An automated method to search for glacier-like forms on Mars?

David L. R. Trethewey

MSc Dissertation

Department of Geography and Earth Sciences

Aberystwyth University

September 2014

Declaration

This work has not previously been accepted in substance for any degree and is not being concurrently submitted in candidature for any degree.

Signature of candidate:

Date:

Statement 1

This work is the result of my own investigations, except where otherwise stated. Where correction services have been used, the extent and nature of the correction is clearly marked in a footnote(s).
Other sources are acknowledged (e.g. by footnotes giving explicit references).
A bibliography is appended.

Signature of candidate:

Date:

Statement 2

I hereby give consent for my work, if accepted, to be available for photocopying and for interlibrary loan, and for the title and summary to be made available to outside organisations.

Signature of candidate:

Date:

Abstract

The Souness *et al.* (2012) catalogue of 1309 Martian glacier-like forms (GLF) is examined and Mars Express High Resolution Stereo Camera stereo coverage identified covering these objects. Of the 1309 objects, 179 tiles of HRSC digital terrain model data are located covering 1030 objects. The HRSC DTMs are used to derive topographic layers including slope, aspect, and curvature layers. These are formed into a layerstacked feature vector, and segmented in Python `RSGISLib`.

Descriptive statistics of the Souness GLFs, in comparison to those of the HRSC DTM tiles as a whole, are used to create a fuzzy classifier, based on the feature vector of the segments. The descriptive statistics show the same trends observed with the lower resolution Mars Orbiter Laser Altimeter data in Souness *et al.* (2012) for elevation, that the GLFs are disproportionately found at middle elevations between -3000m and zero relative to Mars datum, and show a bias to a poleward orientation.

In this work, it is shown that the Souness catalogued objects occur on sloping terrain, with average slope of the extent areas of $\sim 10-15°$ and of the immediate area of 100 m radius around the catalogued head points of $\sim 10-25°$. Both the longitudinal and cross-sectional curvature layers show a bias towards negative values, indicating the GLFs have concave slopes on average, and these objects often are formed in topographic hollows.

The Souness GLF extents show a value for the classifier function that is distinct at a significant level by Z values of at least 2.88 for the HRSC tiles examined, and usually much higher, to the general population of segments. The classifier can act as a search tool to identify potential source areas of viscous flow, but is not specific enough to select glaciers of the type in the Souness catalogue and only those objects.

Contents

x

List of Figures

List of Tables

Chapter 1

Introduction

Recent spacecraft probes exploring Mars have provided a large stream of images and other data concerning the planet. There is a lot of scientific interest in discovering any past or recent existence of liquid water on the surface of Mars, due to its key importance to the question of whether there could have existed any form of life on Mars in the past, or even perhaps in the present day.

One area of interest touching upon this topic is the study of glacial features on Mars. It has been known for a long time that Mars has polar ice caps, (Herschel, 1784), however recent studies have shown the presence of substantial amounts of water ice in the shallow subsurface of large parts of the planet.

Moreover, it has been shown via gravitational simulations, that Mars experiences shifts in its orbital parameters, akin to the Milankovitch cycles on Earth but much more extreme in magnitude. In particular the axial obliquity which currently is $25°$ is thought to have oscillated up to $\sim 60°$ or more, leading to very different patterns of insolation. Subsurface CO_2 ice buried at the poles is expected to have been recycled into the atmosphere at times of high obliquity, leading to a denser atmosphere, warmer climate and a more active water cycle. Studying glacial features on Mars can allow us to examine the climatic history of Mars. As well as its possible relevance for astrobiology, the study of the climatic history of Mars provides a reference comparison to the climatology of our own planet, helping us to understand better the ice ages and climate change on our own planet.

The high resolution topographic data that is becoming available from stereo processing of high resolution imagery opens up a new frontier in landform analysis on Mars. However, the volume of this data is a challenge to traditional manual analysis by domain experts. An automated method of searching for specific features

could narrow down areas of search for features of interest, and provide a method of uniformly searching large areas, that would be impractical to so do manually in an objective way. Subjectivity of classification of landforms from remote sensing imagery and a digital elevation model, even by experts working to a defined set of criteria, is difficult to avoid and was recognised in Reuter, Wendroth & Kersebaum (2006) and references therein.

The aim of this project is to examine whether an automated method analysing medium resolution topographic and image data is successful in classifying terrains associated with glacial features on Mars, of the type examined in the work of Souness *et al.* (2012) from visual assessment of CTX images from Mars Reconnaissance Orbiter. The work of Souness *et al.* (2012) used a visual assessment of ~ 6 metre resolution CTX camera images, together with Mars Orbiter Laser Altimeter topography (at a resolution of ~ 350 m in the mid-latitudes of Mars), to search for objects fitting a set of criteria which had been defined to look for objects which appeared to be analogous to terrestrial valley glaciers.

The first aim of this work, is to use the higher resolution digital terrain model available from the Mars Express *High Resolution Stereo Camera* (HRSC) dataset (50-250m depending on location), to extend the descriptive statistical work characterising these objects done in Souness *et al.* (2012), by examining features including slope and topographic curvature layers, beyond that which was possible using a global low resolution topographic model.

Secondly, the aim is to use the Souness catalogued objects as a training set, to develop an automated classifier to determine locations that are similar to the Souness objects in topography. This will provide a basis for comparison to the manually assembled dataset, and potentially be used to assist in searching for further similar objects on the Martian surface. This is done by segmenting a layer-stack containing feature vector of the imagery, elevation, and derived topographic layers, using the Python RSGISLib software. Similar automated methods using feature vectors have been demonstrated for Mars terrains by Tomasz Stepinski et al. (Stepinski & Collier, 2004; Stepinski & Vilalta, 2005; Bue & Stepinski, 2006; Stepinski, Mendenhall & Bue, 2009; Ghosh, Stepinski & Vilalta, 2010). However, searching the literature did not reveal any previously published research where glacial landforms on Mars have been the subject of a study using automated methods.

Chapter 2

Background and literature review

2.1 General background

2.1.1 Basic parameters of Mars as a planet

Mars has a radius about half that of the Earth, and a mass approximately 0.1 Earth masses. The surface gravity of Mars is 38 % that of the Earth.

The semi-major axis of Mars' orbit is 1.524 astronomical units[1] which results in a lower mean solar irradiance and a longer orbital period of 687 (Earth) days. The Martian orbit is notably more eccentric than the Earth's orbit.

In some respects, Mars is similar to the Earth, having a length of day of 24 hours and 40 minutes,[2] and an axial obliquity to its orbit of 25.2°. These parameters are more similar to the Earth than any other planet in the Solar System.

See table 2.1 comparing these parameters of Mars to those of the Earth, and the NASA Mars Factsheet (NSSDC, 2014) for more information.

---

[1]1AU is defined as the semi-major axis of Earth's orbit

[2]This has led to some challenges in operating Mars rover surface missions, whereby the operations team have needed to keep time with the Martian day, see Mishkin *et al.* (2006) for a review of this.

Parameter	Value	Value in units of similar parameter for Earth
Mass	6.4×10^{23} kg	0.11
Mean radius	3390 km	0.53
Density	3933 kgm^{-3}	0.71
Surface gravity	3.71 ms^{-2}	0.38
Escape velocity	5.0 kms^{-1}	0.45
Semi-major axis of orbit	227.9 $\times 10^6$ km	1.52
Mean solar irradiance	589 Wm^{-2}	0.43
Mean surface temperature	~ 210K (-63°C)	288K (15°C)
Mean atmospheric pressure at surface [a]	6.36 mBar	0.0063
Orbital eccentricity	0.094	5.6
Day length	24.66 h	1.027
Orbital period (sidereal)	687 days	1.88
Spin axis obliquity	25.2°	1.075

Table 2.1: Basic parameters of Mars as a planet

[a]Measured at sea level for Earth, at the mean radius for Mars.

2.1.2 Geological history of Mars

The geological (areological?) history of Mars is generally divided into several time eras, namely the Noachian, Hesperian, and Amazonian.[3]

The Noachian is generally held to have begun with the formation of the Hellas basin by impact 4.1 to 3.8 Gyr ago, and ended around 3.7 Gyr ago. Frey (2003) estimated Hellas formation at 4.1 Gyr ago. The Noachian era was characterized by high rates of cratering and erosion, and valley formation. The Tharsis bulge, an area depending on how it is defined, of 10–30 million km^2 of high ground on Mars, about twice as high above Mars datum as the Tibetan plateau on Earth is above sea level, formed during the Noachian era by uplift caused by volcanic activity.

There are some terrains surviving on Mars from the Noachian era, including the heavily cratered Noachis region for which the era is named. It is likely that all of the visible craters larger than 100km post-date the formation of the Hellas basin. For further detail on Mars' geological history see Carr & Head (2010).

After the Noachian, erosion rates dropped to a fraction of their previous level (Craddock & Howard, 2002), however volcanism continued, resurfacing around 30% of the planet. (Head, Kreslavsky & Pratt, 2002).

The time since ~ 3 Gyr ago is referred to as the Amazonian. Erosion activity slowed further, and volcanic activity also declined to about a tenth of its level in the Hesperian, being confined to the Tharsis and Elysium areas. Volcanic activity is thought to have been highly episodic, suggested by the clustering of crater ages in these areas. (Werner, 2009; Michael & Neukum, 2010).

History of the atmosphere of Mars

The volcanism on early Mars outgassed a significant quantity of water vapour, CO_2 and other gases to the surface. Although the quantity is not precisely known, it is thought to have contributed enough to allow for liquid water to have existed on the surface at early times in areological history. (Craddock & Howard, 2002; Ramirez *et al.*, 2014). It is thought that there could have been several hundred mBar partial pressure of CO_2 in the Noachian era, and a large proportion of it being sequestered in the subsurface crust of Mars, for example in carbonate rocks, rather than having escaped to space. (Jakosky & Phillips, 2001; Lammer *et al.*, 2013) There has been some discussion about exactly what form the Martian atmosphere may have taken

---

[3]These are named after locations on Mars such as Noachis Terra, which form type terrains for the Martian stratigraphy.

at this time, and how dense it could have been. See for example, Kite *et al.* (2011, 2013); Kite, Lucas & Fassett (2013); Kite *et al.* (2014) for details.

Water on Mars in the past

During the Noachian and Hesperian eras, surface conditions were conducive, at least episodically, to liquid water and fluvial erosion. Water is known to have been present on early Mars in the Noachian era, given that ancient terrains showing fluvial erosion have been observed. Hydrous weathering products such as phyllosilicates have also been observed on Mars. Although there appears to have been much less fluvial activity than in the Noachian, there were episodic large floods throughout the Hesperian, which continued to 3 Gyr ago. (Clifford & Parker, 2001; Fairén *et al.*, 2003). Extensive ice deposits are likely to have formed in low-lying areas of Mars, in both the Hellas basin, and the northern plains after the Hesperian flood events. Ice is thought to have flowed from higher areas to the south into the Hellas basin floor. (Kargel & Strom, 1992) The northern plains are also supposed to have been subject to a continental scale glaciation in the past by Kargel *et al.* (1995).

The Dorsa Argentea formation in the southern hemisphere may represent a sink for Martian water. (Head & Pratt, 2001). This is a Hesperian aged terrain of polar plains, that surrounds the present south polar cap and the layered terrain that underlies and surrounds it poleward of $\sim 70° - 80°$S. Plate 1 of Head & Pratt (2001) shows the geographical distribution of Dorsa Argentea. It is thought to have been a sink for water ice and other volatiles, and that in earlier periods of Martian history, an ice sheet covered it that included subglacial water channels, leaving traces in the form of esker landforms. See also the reviews of Tanaka & Kolb (2001) and Kolb & Tanaka (2001).

2.1.3   Global trends in the topography of Mars

There is a global dichotomy in the elevation of the Martian surface, with a bimodal distribution, with a difference of 5.5km between the two hemispheres. (See figure 2.1). The low-lying northern plains are also covered by younger deposits, as shown by the lower density of craters. (Aharonson, Zuber & Rothman, 2001).
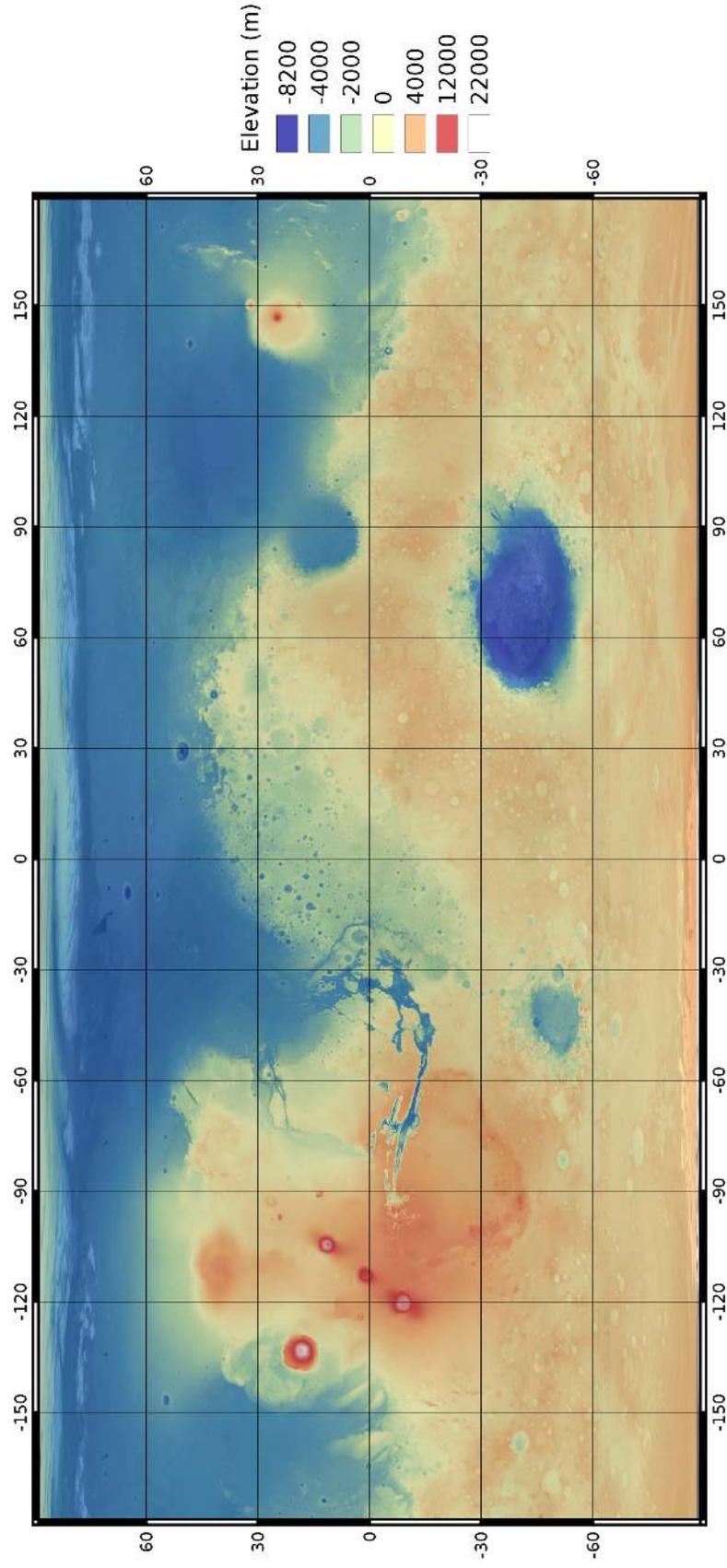
Figure 2.1: The global elevation map of Mars, based on Mars Orbiter Laser Altimeter LiDAR data from Mars Global Surveyor. The Hellas basin in the southern hemisphere is the lowest point, and the general dichotomy between the northern and southern hemisphere, and the elevated Tharsis bulge can be seen. See the maps in Appendix A for more detail.

2.2 Water ice on Mars

Water ice is known to exist in the polar caps of Mars, being detected by Viking orbiter instruments and by telescopic near-infrared spectroscopic observations. (Clark & McCord, 1982).

Contemporary Mars is hyperarid and cold by comparison with Earth. The mean annual temperature is $\sim$ 215K at the equator, and a mean surface pressure of 6.1mBar. (Carr & Head, 2010). The maximum atmospheric pressure on the surface of Mars is at its lowest topographic point in the floor of Hellas basin, at approximately 11.55 mBar. (Zalewska, 2013, 2014) This exceeds the triple point of water, which is 6.12 mBar. The H_2O partial pressure in the Martian atmosphere is only $\sim 1\mu$Bar or 160 ppm, which makes it approximately 1000 times drier than the Earth's atmosphere. Thus even if there are regions such as this and others (Lobitz *et al.*, 2001), where water can be stable against freezing and boiling, the hyperarid atmosphere means it is not stable against evaporation. (Martínez & Renno, 2013) In order for pure liquid water to be stable against evaporation, the partial pressure of H_2O in the atmosphere would have to be greater than the saturation water vapour pressure which at the triple point temperature is 6.1173 mBar.

This means that pure liquid water can only exist temporarily even where temperatures exceed freezing point and pressure triple point. Any liquid water would in any case freeze at night, since night-time temperatures are universally below freezing on Mars, given the poor ability of the thin atmosphere to retain heat. Water ice is not stable against sublimation at the surface, since the hyperaridity of the atmosphere favours sublimation. It will persist at the surface where temperatures remain extremely low, such as in the polar caps where daytime temperatures remain low and sublimation is slowed.

However, strong brines of certain salts can potentially exist under Martian temperature and pressure conditions (Ellery *et al.*, 2002), and brine flows have been hypothesised to be the cause of the 'recurring slope lineae' observed in some areas of Mars. (McEwen *et al.*, 2013).

Even if ice cannot avoid sublimation on the surface, at relatively modest depth water ice can be stable since daily temperature variations are damped, causing permafrost conditions where the ground temperature is always below 0°C. Neutron and gamma-ray spectroscopy indicates ice at depths of tens of centimetres below the surface at latitudes over 60°. (Boynton *et al.*, 2002; Feldman *et al.*, 2004). The Phoenix lander, which landed at a latitude of 68°N in the northern polar region,

also confirmed water ice presence, uncovering ice with its robotic arm at depths of 5-15 cm. There were also some droplets seen, which are believed to be liquid salt water brines. (Mellon *et al.*, 2009; Rennó *et al.*, 2009).

At lower latitudes, the ice fraction detected by orbital spectrometers is lower than at high latitudes, however geological indicators of the presence of ground ice, such as patterned ground (Levy *et al.*, 2009), and sublimation pitting (Mustard, Cooper & Rifkin, 2001; Milliken, Mustard & Goldsby, 2003) are found at latitudes as low as 30°. Significant amounts of subsurface ice may be found either at depths too great to allow it to be detected by the orbiting spectrometers, or in local areas smaller than their spatial resolution.

Dundas & Byrne (2010) considered the sublimation of shallow subsurface ice that had been exposed by recent impacts on the Martian surface, observed by Byrne *et al.* (2009). They concluded that there was a high volumetric fraction of ice in the subsurface material exposed by the impact, in excess of that which could be found within pore-spaces.

Glaciation on Mars is thought to have occurred locally and regionally in several places, including the tropical mountain areas on the Tharsis bulge, and the mid-latitude regions. Previous work observing Martian glacial landforms is reviewed in section 2.5.

2.3   The Martian orbital obliquity cycle

Both Mars and the Earth experience gravitational perturbations from other planets, principally Jupiter, Earth and Venus. Jupiter is more massive than any other planet, but Venus approaches Earth much more closely, therefore due to the inverse-square law of gravity it is a significant perturbation on the Earth. On Earth, these perturbations cause the Milankovitch cycles in the Earth's orbital eccentricity, axial obliquity and longitude of perihelion. These have an effect on glaciation on Earth, particularly in the way in which total summer insolation at high latitudes varies, and hence summer melting. (Hays, Imbrie & Shackleton, 1976).

The axial obliquity of Mars is currently $25°$. The oscillations on Mars are more extreme, including a variation of the obliquity expected from simulations of up to $\sim 60°$. (Laskar, Joutel & Boudin, 1993; Laskar *et al.*, 2004). Unlike the Earth, Mars has no large satellites, its two moons Phobos and Deimos being very much smaller than the planet. The larger of the two, Phobos has a mass of $\sim 10^{16}\text{kg}$,
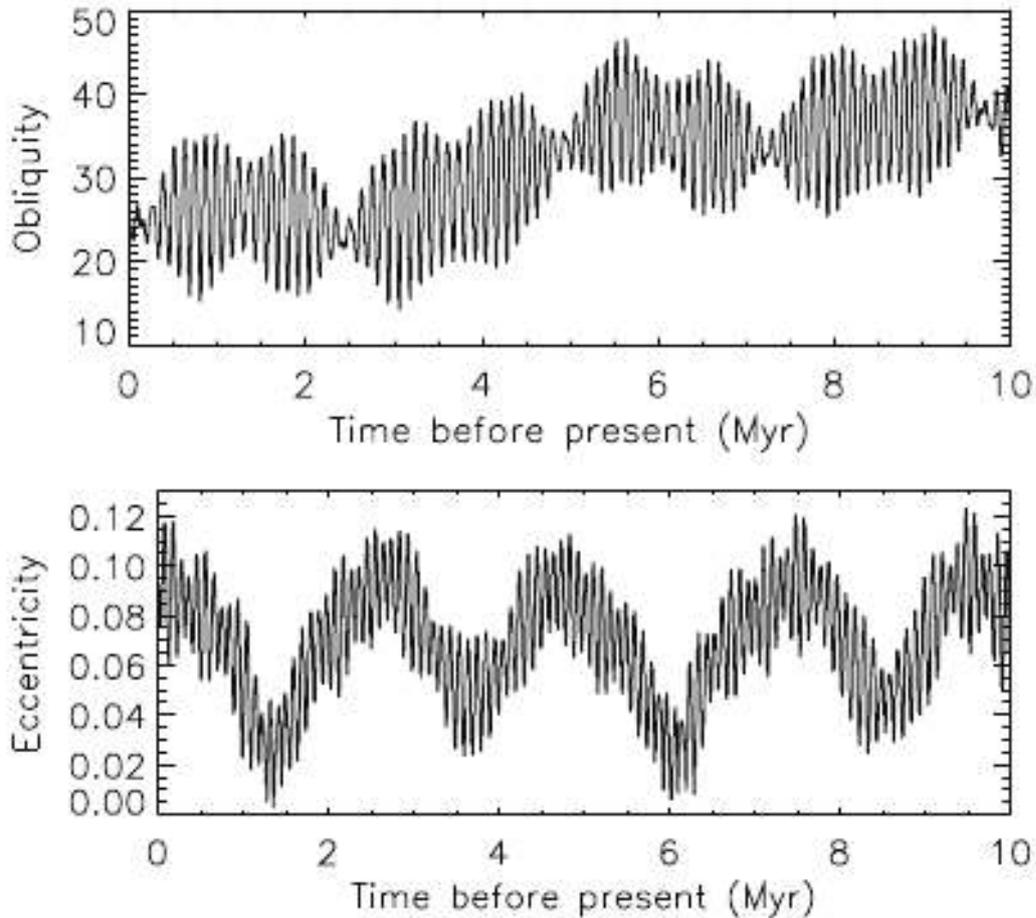
Figure 2.2: The simulated history of Martian orbital eccentricity and obliquity according to Madeleine *et al.* (2009).

compared to a Martian mass of $\sim 6 \times 10^{23} \mathrm{kg}$. Thus they are insignificant when considering gravitational influences on Mars., whereas the Earth's moon exerts a stabilising influence on the Earth's obliquity. Large changes of obliquity over time are calculated for a simulated moonless Earth by Lissauer, Barnes & Chambers (2012). This would have major effects on the climate of such a hypothetical planet, an issue to be considered in speculation about the habitability of extrasolar planets. (Williams & Pollard, 2003).

At high levels of obliquity on Mars, ice tends to be driven from the polar regions (which experience more summer insolation, and for extreme obliquity levels, more insolation in total than the tropics at these times) and deposited at lower latitudes. Forget *et al.* (2006) and Montmessin (2007) reviewed the impact on obliquity changes on the Martian climate, noting that 5 Myr ago, when obliquity is calculated

10

to have been oscillating around a value of $\sim 35°$, total polar insolation would have been about 50% greater than today. Carbon dioxide ice currently sequestered in the polar layered deposits can be returned to the atmosphere, making a warmer, thicker atmosphere. The quantity of CO_2 that can be made available to the atmosphere is unknown, but may have been significant. (Yokohata, Odaka & Kuramoto, 2002; Forget, 2009; Trainer *et al.*, 2010). Whether or not the atmosphere is significantly thicker during high obliquity epochs, changes to climate are expected, with warmer summer maxima, and greater gradients between hemispheres that would have led to large dust storms at the summer solstices with greater dust lifting than today. (Haberle, Murphy & Schaeffer, 2003; Newman, Lewis & Read, 2005). The total water vapour available in the atmosphere may increase markedly from its present low value; the total water column may increase from $\sim 60\mu$m to $\sim 3000\mu$m. (Fouchet *et al.*, 2007; Madeleine *et al.*, 2009).

In the last few Myr, the obliquity is expected to have oscillated between approximately $15°$ and $35°$ about a mean of $24°$ (see figure 2.2), however the longer term mean is calculated at around $40°$, with higher obliquities of $\sim 60°$ or more being possible. The periodic oscillation of obliquity takes ~ 125 kyr, and has an amplitude modulation with a period of ~ 1.3 Myr. The maximum oscillation amplitude of the periodic changes is $\sim 20°$. The longer-term changes of the mean obliquity at timescales of ~ 5 Myr and greater are chaotic.

Changes to the eccentricity of the Martian orbit, and the precession cycle, determining which hemisphere is experiencing summer at closest approach to the Sun, also play roles in the Martian climate.

At current obliquity conditions, ground ice should be present down to $\sim 40°$ however indicators of ice down to latitudes as low as $30°$ are observed. Thus observations are important to determine the extent of current subsurface ice.

2.4   Observations of ground ice on Mars

Mustard, Cooper & Rifkin (2001) used Mars Orbiter Camera images from the Mars Global Surveyor mission, and found features associated with ground ice in Martian mid-latitudes, including a dissected mantle and viscous creep features.

According to Head *et al.* (2003), the Martian surface in the $30 - 55°$ latitude belts is covered with a ~ 10m thick layer of material composed of a mixture of ice and dust, that was deposited in the most recent higher-obliquity era between

2-0.4 Myr ago. (Searls *et al.*, 2008; Schon, Head & Milliken, 2009).

There are several types of viscous flow feature that have been studied in the literature. Lobate Debris Aprons were studied on Mars as long ago as the Viking Orbiter era, when the work of Squyres (1978) found flow features in the 'fretted terrain', and Squyres (1979) mapped their distribution on the Martian surface. These are explained as the relaxation of a broad region of ground dominated by ice, across a lower topography, which is not strongly constrained. They may be hundreds of metres thick, and run parallel to the adjacent escarpment. (Pathare, Paige & Turtle, 2005; Levy, Head & Marchant, 2007; Kadish *et al.*, 2008; Berman, Crown & Bleamaster III, 2009; Morgan, Head & Marchant, 2009; Hartmann & Werner, 2010).

Lineated Valley Fills are areas where a large valley constrained by topography is filled with a viscous flow feature. These are sometimes formed as the convergence of several lobate debris aprons, (Kress & Head, 2008; Baker, Head & Marchant, 2010; Van Gasselt, Hauber & Neukum, 2010) although the terminology is sometimes used to refer to a smaller feature analogous to a valley glacier on Earth. This convergence can produce a diverse range of complex patterns and surfaces. They can exhibit a 'thermokarst' surface where the terrain is dissected by processes of sublimation and disaggregation, thermal weathering of ice deposits. Various types of viscous flow feature, may form part of an integrated system, (Head *et al.*, 2010), or a viscous flow may be superposed on another older one, such as for some features in Nilosyrtis Mensae detailed in the work of Levy, Head & Marchant (2007).

2.5 Mid-latitude glaciers on Mars

The formation of glaciers in Martian mid-latitudes at high obliquity was studied in Head *et al.* (2005) and Forget *et al.* (2006). Souness & Hubbard (2012) review much of the recent work on glacier-like forms on Mars. Other work focusing on individual features and areas includes Morgan, Head & Marchant (2009); Soare & Osinski (2009); Hubbard *et al.* (2011); Souness & Hubbard (2013); Hartmann *et al.* (2014) and Hubbard, Souness & Brough (2014).

There are a range of features on Mars which are believed to be glacial in origin, or be ice-related, including some which bear resemblance to terrestrial valley glaciers. (Marchant & Head, 2003; Head *et al.*, 2005; Forget *et al.*, 2006). Pierce & Crown (2003) studied debris aprons east of the Hellas basin, and suggested

debris-covered ice flow as a possible model. Further features studied on Mars are pedestal craters in Kadish *et al.* (2008), polygonated and patterned ground (Burr *et al.*, 2005; Mangold, 2005; Soare, Osinski & Roehm, 2008; Levy, Head & Marchant, 2009; Levy *et al.*, 2009; Levy, Marchant & Head, 2010), and periglacial features such as pingos. (Soare, Burr & Wan Bun Tseung, 2005; Burr, Tanaka & Yoshikawa, 2009; Dundas & McEwen, 2010; Soare *et al.*, 2014). For a terrestrial comparison, see Marchant *et al.* (2002) for observations of polygonated terrain in Beacon Valley in the Antarctic Dry Valleys.

'Glacier-like forms' has been the name used in Souness *et al.* (2012) for objects appearing analogous to some valley glaciers on Earth. Some of the glaciers in the Antarctic Dry Valleys (Rignot, Hallet & Fountain, 2002; Marchant & Head, 2007) are a particularly useful analogue. Ablation of Antarctic Dry Valley glaciers is primarily by sublimation, as would be the case on Mars. Fountain *et al.* (1998) found 70-90% of total ablation was by sublimation. Debris cover becomes more concentrated as sublimation removes ice. See figure 2.3 for an image of a debris-covered glacier in Beacon Valley, Antarctica.

The flow rate of some Antarctic Dry Valley glaciers can be as low as < 40 mm yr^{-1} for the Mullins and Friedmann glaciers in Beacon Valley. Under current Martian conditions, where the average temperature is at an average of around -50°C or less, glacier ice is expected to remain very cold year-round due to debris cover, and a lower surface gravity to provide stress, similar or even slower flows can be expected. For water ice, the exponent n in the strain-stress equation (Glen's Law) $\dot{\epsilon} = A\sigma^n$ is ~ 3. The value of A, is dependent on temperature (see Chapter 4 of Benn & Evans (2010), and Chapter 11 of Melosh (2011)), and at low temperatures $\ll 0$°C this reduces to an exponential dependence on temperature of the form $A \propto e^{-\frac{Q}{RT}}$ where Q is the creep activation energy, and R is the ideal gas constant.

During the last glacial maximum, conditions in the Antarctic Dry Valleys were even colder and drier than today, and mean annual temperature may have been as low as -68°C, comparable to present-day mid-latitudes of Mars. (Marchant & Head, 2007). Insolation may be of similar order of magnitude, since the high-latitude areas of Antarctica at ~ 80°S experience a low sun angle always $< 33°$, whereas a $40°$ latitude glacier on Mars at high obliquity would have experienced direct overhead insolation during summer.

It is thought that some areas of the Antarctic Dry Valleys, have preserved

Figure 2.3: Debris-covered glacier in Beacon Valley, Antarctica.
Image credit: Boston University Antarctic Research Group

glacier ice dating back ~ 8 Myr (Sugden *et al.*, 1995), beneath ~ 60 cm of debris cover, which may indicate it is possible to preserve ice for millions of years in the Martian subsurface at mid-latitudes. Kowalewski *et al.* (2006) modelled rates of sublimation of a detached remnant of the debris covered Taylor Glacier in Beacon Valley, suggesting that ice survival since the Miocene could have been possible with an average climate slightly colder than present. See also Bryson *et al.* (2008).

The Martian glacier-like forms often appear on the slopes of high relief landscapes and show morphologies indicative of viscous flow. The very low hypothesised flow rates support the view that these features are relics from a higher obliquity era when warmer climates existed at mid-latitudes more conducive to accumulation and viscous flow of ice. The lateral margins and lower extents of these features have been observed to have 'moraine-like ridges' which have multiple ridges aligned in parallel to each other. This apparent nesting has been observed both on flat surfaces and valley walls. There may have been successive flow events causing multiple moraines to be observed. Most GLFs have a broad upper basin that merges gradually with surrounding topography, and an elongate tongue that is typically confined by raised bounding ridges.

Crater density studies, e.g. Hartmann (2005) indicate a geologically recent origin and an age < 10 Myr for these glacier-like forms. According to Hartmann & Werner (2010), craters $< \sim 90$m survive only about ten percent as long on viscous flow features than on plains.

GLFs are sometimes observed to flow out of cirque-like alcoves and merge into the upper reaches of LDAs. This is particularly common on the Protonilus and Deuteronilus Mensae areas of the topographic dichotomy boundary. In some cases it appears that LDAs include mass solely derived from several GLFs, in others that the GLF flow is superposed on an older LDA, and flows out on top of it.

There has been some argument concerning to what extent viscous flow features on Mars are filled by ice, or an ice-debris mixture, analogous to Earth 'rock glaciers'. At least some of the GLFs are predominantly ice rather than rock according to SHARAD radar observations. (Holt *et al.*, 2008; Plaut *et al.*, 2009). This favours an atmospheric precipitation model of accumulation rather than the model of pore-filling condensation.

'Glacier-like flows' has also been used as an alternative name for glacier-like forms, however it may be more appropriate to use the latter since current flow has not been observed for these features. There has been a general consensus that Martian viscous low features are 'cold-based', i.e. frozen to their underlying surface, based on the absence of substantive evidence for wet-based glaciation, such as pro-glacial or lateral meltwater streams, and the prevailing very low temperatures on Mars.

2.5.1 A case study: Glacier-like forms in crater Greg

Hubbard *et al.* (2011) described the surface terrain associated with a viscous flow feature, on the southern (poleward) facing rim of a 66 km diameter crater, named 'Greg', in eastern Hellas Planitia, east of the Hellas basin at 38.15°S, 113.16°E. This area has also been studied in Hartmann, Thorsteinsson & Sigurdsson (2003); Marchant & Head (2003); Milliken, Mustard & Goldsby (2003) and Hartmann *et al.* (2014). See figure 2.4.

Detailed imagery, and detailed 1m resolution topographic information via a digital terrain model derived is available from HiRISE stereo imagery. Crater Greg is thought to be of age $\sim 1 - 3$ Gyr. There are a series of different terrains, with characteristic patterning textures, and differing slopes of the topography. (see figure 2.5).
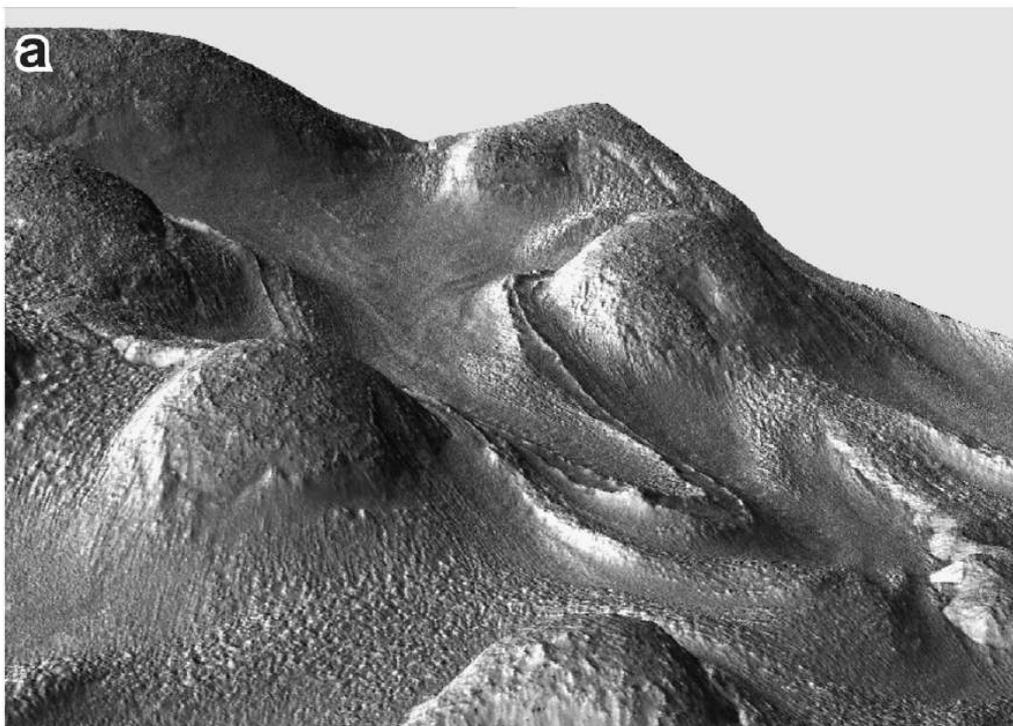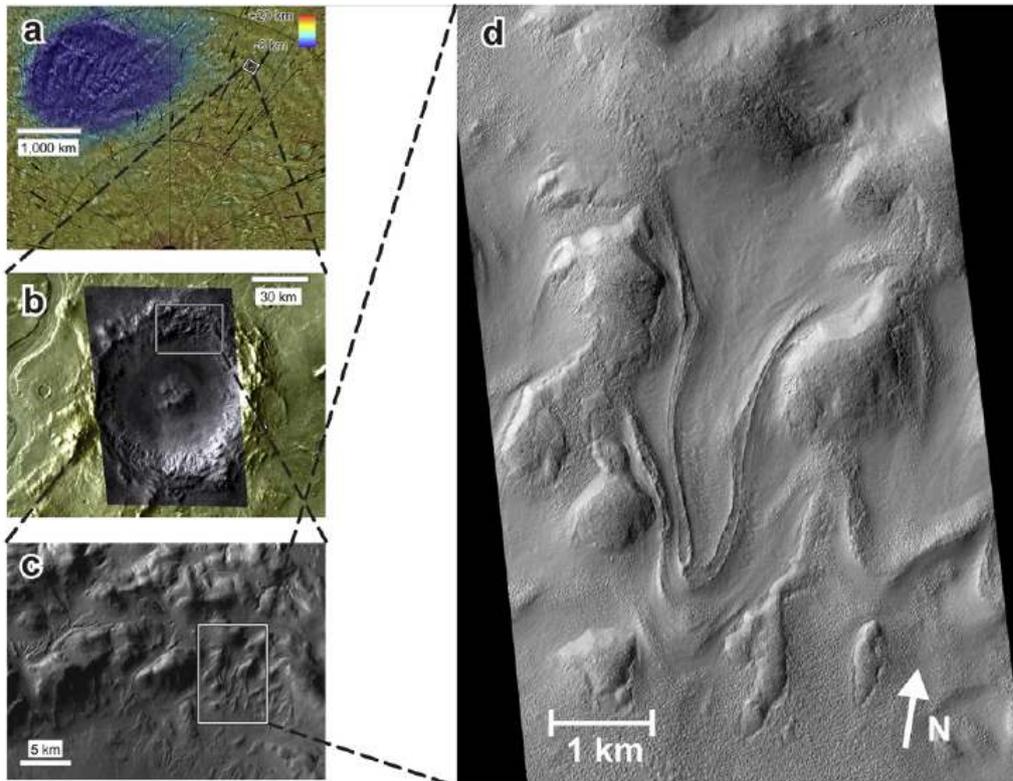
Figure 2.4: A figure from Hubbard *et al.* (2011) showing the location of a GLF complex on the north wall of the southern hemisphere crater Greg, and a 3D perspective rendering of one of the GLFs.
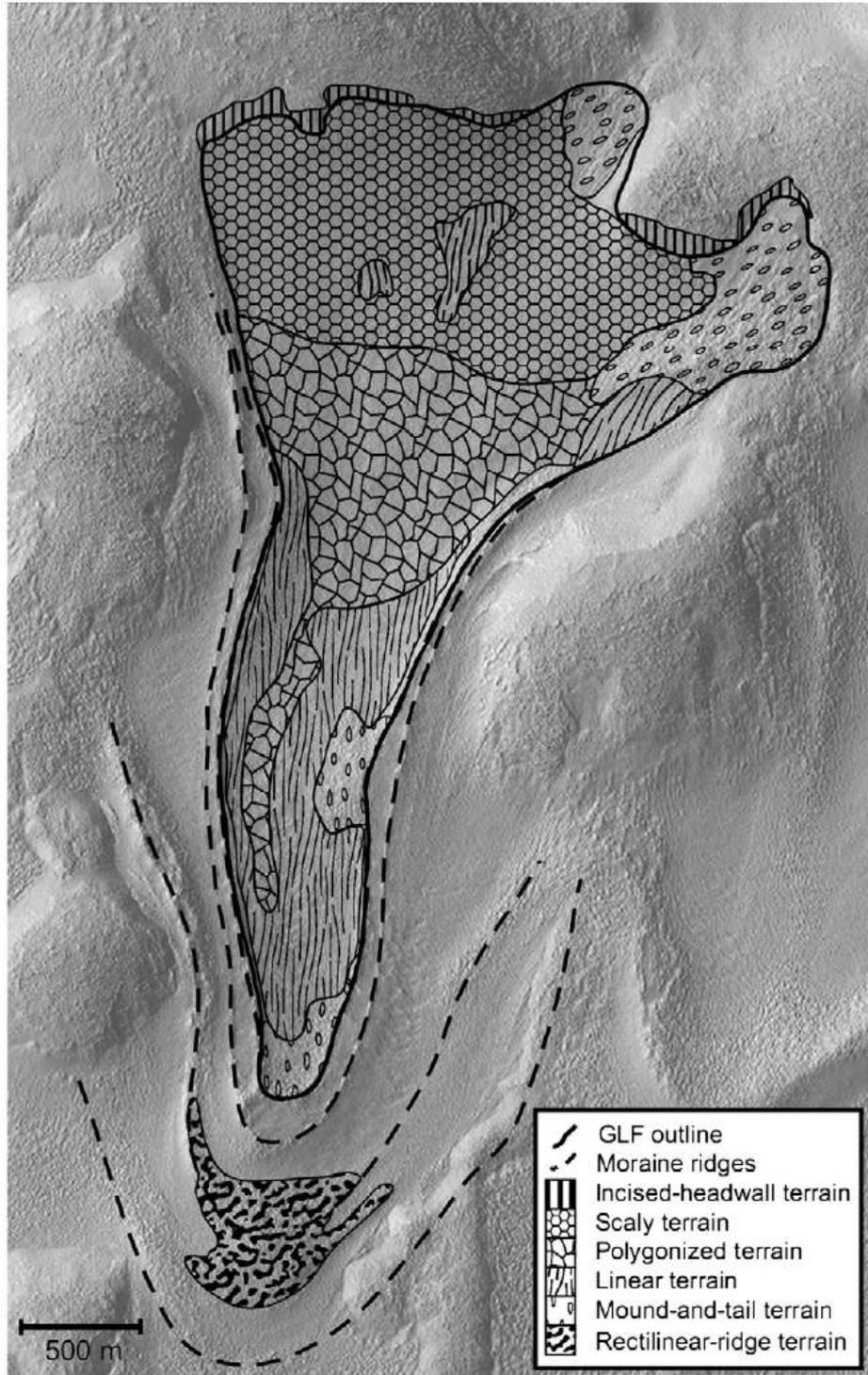
Figure 2.5: A figure from Hubbard *et al.* (2011) showing a geomorphological map of the terrains in one of the GLFs on the north wall of crater Greg.

17

The upper margin of the feature is bounded by steep ($\sim 30°$) headwalls, typically some tens of metres high. These are incised by a series of slope-parallel lineations. Below the incised headwalls, the feature flows at a general angle of $\sim 10°$ from a broad upper basin to a lower tongue that is bounded by a series of nested elongate raised ridges.

It was suggested in Hubbard *et al.* (2011) that the glacier may have been partially wet-based at the time of its maximum extent, and has experienced a period of recession, punctuated by stand-still or advance since that time.

Polythermal ice masses generally have a warm-based (wet) interior where thick overlying ice provides insulation to allow the $0°$C isotherm to rise above the bed surface, and cold-based margins. There are outlet glaciers in East Antarctica that exhibit this form, including as postulated in Hubbard *et al.* (2004), those where the basal temperature is expected to be well below freezing, and basal melting is only possible by the subglacial water being hypersaline.

By crater counts, i.e. the density distribution of small (11-16m) diameter craters, the feature is concluded to be no older than ~ 10 Myr old, consistent with timescales from flow deformation studies. (Turtle *et al.*, 2001; Milliken, Mustard & Goldsby, 2003). Within the innermost bounding moraine, there is a generally smooth surface, there is little evidence of wind deflation or degradation, and no large impact craters, indicating a young surface age within the last ~ 0.4 Myr.

The lowering of the feature within its bounding lateral and terminal moraines, indicates that the feature has been lowered by mass loss within the last $10^5 - 10^6$ years, and the nesting of at least four latero-terminal moraines shows evidence for cyclical or punctuated variations in processes controlling mass loss.

The feature is number 947 in the Souness *et al.* (2012) catalogue. It has an area quoted as 3.09 km^2.

The terrain may be contrasted with areas outside the feature, the feature contains areas of 'scaly terrain', 'polygonized terrain', 'linear terrain', and 'mound-and-tail terrain', with areas of 'rectilinear-ridge terrain' outside the GLF proper but within the outermost bounding terminal moraine ridge. Areas outside of the GLF in the same general area exhibit terrains such as 'dust-mantled rocky uplands' and 'subdued hilly lowlands'. These terrain types are examined in detail in Hubbard *et al.* (2011) from HiRISE imagery. See figure 2.5.

The upper portions of the feature, featuring 'scaly terrain' and 'polygonized terrain' exhibit slopes of $\gtrsim 10°$. They may be formed by thermal cracking in

periglacial processes, and the 'scaly terrain' may represent a layer of unconsolidated material due to the boulder tracks observed in this feature.

Noting the absence of a large supply hollow above the basin, Hubbard *et al.* (2011) favour air fall precipitation for supply of the glacier, or supply from surrounding ground.

The 'linear terrain' and 'mound-and-tail' terrain in the mid to lower part of the feature are interpreted as subglacial features in the wet-based portion of a polythermal glacier. Since they extend to the base of the GLFs lateral moraines, they are hypothesised to have formed at the GLF's maximum recent extent. If these are indeed exposed bedforms, it would indicate the glacier has now completely receded from its lower extent.

Fassett *et al.* (2010) note a series of valleys in the floor of crater Greg, which the observed young viscous flow features do not reach to, however hypothesise an earlier epoch of glaciation that may have done so, and that these valleys may have formed part of the drainage system.

Hartmann *et al.* (2014) also study this area, giving a detailed overview of the geomorphology of the south and north walls of crater Greg. The southern wall is steep at around $12°$ and has its base at lower elevation. It shows valley networks arranged in a branching pattern, indicating fluvial activity at a time when free surface liquid water flowed for at least several kilometres.

They also study the slopes on a range of glacial tongues in the northern part of crater Greg, finding a range of slopes of $6.5°$ to $16.4°$, with a mean value of $10.2 \pm 2.3°$. They also examine what they interpret as a separate class of object, more similar to protalus lobes, or rock glaciers (their fig 17), which have a less tongue-like, more arcuate morphology.[4] They also note the depression of central parts of the tongues relative to the bounding ridges, due to sublimation losses.

They argue that the fluvial valleys at the foot of the north wall toe are related to older episodes of glaciation and runoff, rather than subglacial melting of the currently observed glacial tongues, based on an older supposed age of the northern crater floor of $\sim$ 300-800 Myr.

They also conclude based on the profile slope that the calculated basal shear stress $\tau = \rho g h \frac{dh}{dx}$ for the glacial tongues, more closely corresponds to pure ice, or dusty-ice glaciers, than terrestrial rock glaciers, agreeing with radar observations

---

[4]This may depend on the context in which 'rock glacier' is used, which can vary in the literature between protalus permafrost features, to glacier ice with a high proportion of mixed rock.

of the region from Holt *et al.* (2008). A 'rock glacier' would require a greater shear stress for the same level of flow, thus would be expected to have a steeper slope.

Souness & Hubbard (2013) studied another region in the northern hemisphere of Mars. This is a cirque-like alcove in eastern Protonilus Mensae, at lat/long $54.55°E, 40.80°N$. They conclude that this represents a glacier flow out of the alcove, rather than a relic from a past epoch where a glacier flowed into the alcove after which downwasting of the main glacier by sublimation occurred, and reversal of the flow gradient, as was hypothesised by Dickson, Head & Marchant (2008).

Souness & Hubbard (2013) constructed a geomorphological map of the feature, showing surface texture assemblages. This feature, where HiRISE image coverage is available, shows a similar kind of 'mound-and-tail' terrain as was found in the GLF in the northern wall of crater Greg in Hubbard *et al.* (2011). These are interpreted, unlike terrestrial drumlins which are subglacial bedforms associated with wet-based or polythermal glaciers, as supra-glacial features, caused by longitudinal foliation by ice flow and deformation.

2.6   Current and recent Mars spacecraft probes

Mars Global Surveyor spacecraft entered Mars orbit in September 1997, and operated until November 2006. (Albee, Palluconi & Arvidson, 1998). It carried instruments including the Mars Orbiter Camera (MOC), Mars Orbiter Laser Altimeter (MOLA), the Thermal Emission Spectrometer (TES), a magnetometer and a radio experiment to measure the gravity field.

The LiDAR instrument, the Mars Orbital Laser Altimeter (MOLA) on Mars Global Surveyor, was originally flown on the failed Mars Observer probe in 1992. (Zuber *et al.*, 1992). An almost identical instrument was instead flown on Mars Global Surveyor.

An explanation of the MOLA dataset can be found in Som, Greenberg & Montgomery (2008). The MOLA gridded datasets are released at resolutions up to 128 pixels/degree, which at the Martian equator is $\sim$ 450m. The vertical accuracy of MOLA is of the order of about 10m near the equator. Examples of the use of MOLA for global elevation statistics on Mars are given in Smith *et al.* (1999); Kreslavsky & Head (2000); Aharonson, Zuber & Rothman (2001). Direct use of early MOLA tracks to provide elevation profiles of a number of features, and show the initial result of the flatness of the northern plains are detailed in Smith

et al. (1998).

The Mars Express spacecraft, launched by the European Space Agency, reached Martian orbit in December 2003 and the orbiter part of the mission is currently still operating, though unfortunately the lander part of the mission, *Beagle 2*, failed. [5]

The High-Resolution Stereo Camera (HRSC) on Mars Express (Neukum & Jaumann, 2004; Scholten *et al.*, 2005; Jaumann *et al.*, 2007), provides images at resolution of 12.5m/pixel[6], and DTMs gridded at between 50-250m. Stereo coverage, is achieved through an along-track stereo method using nadir directed, forward and aft looking ($\pm 18.9°$), and 2 inner ($\pm 12.8°$) push-broom line sensors. This reduces the problems that can exist with stereo images where differing illumination conditions cause problems in photogrammetric analysis. (Gwinner *et al.*, 2009). As of 2014, approximately 40 % of the Martian surface has HRSC DTM coverage. (Jaumann *et al.*, 2014). The imaging spectroscopy OMEGA visual/near-infrared instrument is also carried on Mars Express and has been used to search for hydrated minerals. (Bibring *et al.*, 2005, 2006).

The Mars Odyssey probe, launched by NASA in 2001, carried instruments including the infrared THEMIS (Thermal Emission Imaging System), a multispectral visible and infrared camera (9 bands between 6.78 and 14.88 μm), for determining the distribution of minerals; the GRS (Gamma Ray Spectrometer), for determining the presence of 20 chemical elements on the surface of Mars, including hydrogen in the shallow subsurface. It also acts as a communication relay to surface missions such as the Mars Exploration Rovers, and Mars Science Laboratory *'Curiosity'* rover.

The Mars Reconnaissance Orbiter, launched by NASA, arrived at Mars in 2006 and carried several instruments including the imaging instruments of the HiRISE and CTX cameras. A description of the HiRISE instrument can be found in McEwen *et al.* (2007) and Delamere *et al.* (2010). The HiRISE data product specifications can be found in Eliason *et al.* (2007) and Eliason *et al.* (2009) and for the context camera Malin *et al.* (2007) and Malin, Lavoie & Grayzeck (2007). HiRISE images, where there is stereo coverage, can be used to produce digital terrain models. (Kim & Muller, 2009). DTMs can be produced at 1m gridding, however only relatively small areas[7] have been covered in stereo. The 'context'

---

[5]See Bonnefoy *et al.* (2004) for a study of possible reasons for the failure.

[6]HRSC also has a high resolution channel, covering a smaller area at a resolution of up to 2 metres.

[7]Approximately 0.1 % of the surface of Mars has coverage with stereo HiRISE images, and not all of this has a DTM derived, given that it is computationally intensive and not fully automatic

CTX camera, has a resolution of ~ 6m, and near-global coverage by the present time.

MRO also carries MARCI, a wide-angle multispectral (2 UV and 5 visible bands) camera aimed at providing daily global images of Mars for weather monitoring purposes, CRISM (Compact Reconnaissance Imaging Spectrometer for Mars) an imaging spectrometer covering a wavelength range 0.362 to 3.92 μm, MCS (Mars Climate Sounder) uses spectroscopy from visible to thermal infrared (0.3 - 50 μm) to examine the Martian atmosphere for temperature, humidity and dust content, and SHARAD (Shallow Radar) which probes the subsurface using radar waves within a 15 to 25MHz range to search for liquid or frozen water by its strong radar return.

The SHARAD data analysed in Holt *et al.* (2008) shows at least some GLFs, in the region east of Hellas observed in that work, are predominantly ice with only a thin debris cover. Further work in the northern hemisphere by Plaut *et al.* (2009) showed a number of lobate debris aprons in Deuteronilus Mensae also are primarily water-ice with only a minor debris component.

The recent surface missions by the Mars Exploration Rovers, *Spirit* and *Opportunity*, and the Mars Science Laboratory *'Curiosity'* rover, all landed within the equatorial regions. The 1997 *Pathfinder* mission landed at 19°N 33.5°W in Ares Vallis. (Golombek *et al.*, 1999). The Viking 2 lander however, landed at $47°$N, $48°$E in Utopia Planatia, and *Phoenix* in the north polar region at $68°$N, $126°$W. (Lemmon *et al.*, 2008). The Viking 2 lander found pitted rocks at its landing site, which could be evidence of past freeze-thaw weathering during high obliquity times. There have been similar rocks observed in Antarctica described in Marchant & Head (2007). The Soviet Mars 3 lander made the first soft-landing on Mars in 1971 at 45°S, 158°W, but only transmitted data to Earth for 14.5 seconds before contact was lost with the lander. (Perminov, 1999).

2.7   The Souness *et al.* (2012) inventory of glacier-like forms on Mars

The study of Souness *et al.* (2012) used visual analysis of Mars Reconnaissance Orbiter 'context' images from the CTX camera, according to a set of criteria, listing a set of 1309 'glacier-like forms' on the Martian surface within the mid-

---

as noted in section 2.8.

latitude regions, a search area between 25° and 65° in both northern and southern hemispheres. The criteria used were that:

i) they are surrounded by topography, showing evidence of flow around or over obstacles.

ii) they be distinct in texture or colour from surrounding areas.

iii) they display surface foliation indicative of down-slope flow such as compressional or extensional ridges, surface lineations, arcuate surface morphologies or surface crevassing.

iv) they have a length to width ratio > 1, thus being distinct from the apron-like lobate debris apron features.

v) they have either a discernible 'head' or 'terminus'.

vi) they appear to contain a volume of ice or other viscous substance, having a relatively flat valley fill surface.

Souness *et al.* (2012) used a 5km circular radius buffer around the heads of GLFs, extracting topographic information from Mars Orbital Laser Altimeter data, to determine statistics of the elevation above Mars datum. Statistics were also collected for the orientations of the forms. In both the northern and southern hemispheres, there was a bias towards a pole facing aspect, with the bias being stronger in the southern hemisphere.

In this inventory, the GLFs are most common in middle elevations, they seem to be depleted at elevation < -3000 m relative to Mars datum, and also at the highest elevations. GLFs occur predominantly in the range -3000 m to -500 m, by measure of the ratio of the normalised GLF count to the normalised surface area against elevation. There is a clustering of GLFs in particular areas, such as the NW rim of the Argyre basin, regions east and west of the Hellas basin, in the southern hemisphere, and in the northern hemisphere the global elevation dichotomy boundary, the most densely packed regions being in the 'fretted terrains' (Sharp, 1973) of Deuteronilus Mensae, Protonilus Mensae, and Nili Fossae. The northern lowland plains contain virtually none, except isolated examples within the rims of large craters.

The populations cluster around latitudes of $\sim 40°$ north and south. The southern hemisphere objects have a higher mean elevation of 884.7 m compared to

-1366.3 m in the north. The southern hemisphere distribution follows more closely the general hypsometry of the terrain than the north.

2.8   Topographic data available for Mars

The topography of Mars has come from two main sources. One is a LiDAR instrument, MOLA carried by Mars Global Surveyor, which provides near global (to $88°$ latitude) coverage gridded at a resolution of 128 pixels/degree, which at the equator is ≈ 460m. See also section 2.6. The second source has been generating stereo DTMs from images through photogrammetric techniques. Mars Express and Mars Reconnaissance Orbiter images have both been used for this purpose. See section 2.6 for further information. The data source used for the quantitative analysis of this study is the *High Resolution Stereo Camera* of the Mars Express spacecraft.

For the data in this study, of the 1309 objects in the Souness catalogue, 1030 have an HRSC DTM, 60 objects have 50 metre topography resolution and a further 481 have 75 metre resolution data. See figure 2.6 and table B.1 where the HRSC tiles used in this work are shown.

An evaluation of several different methods of processing the HRSC stereo images to generate DTMs can be found in Heipke *et al.* (2007).

The HiRISE camera on Mars Reconnaissance Orbiter, can create imagery at a resolution of 0.25m, which is in fact a finer resolution than any currently commercially available satellite imagery of the Earth, and available freely. Approximately 4% of the surface of Mars has been covered by HiRISE to date in 2014, however only a relatively small proportion has stereo coverage.

To generate a DTM from a stereo image pair, it is first necessary to find corresponding points in two or more images, then to transform the image coordinates into ground coordinates, by a geometric model of the satellite camera system.

The process of generating a terrain model is computationally intensive and the image matching step is not fully automatic, so not all areas that have stereo coverage actually have a DTM. Kim & Muller (2008, 2009) explain the process of extracting a terrain model from HiRISE data.

The HiRISE Operations Center (HiRISE Operations Centre, Lunar and Planetary Laboratory, University of Arizona, 2014) has a publicly available archive of DTMs, and some further areas have stereo DTMs generated by various researchers
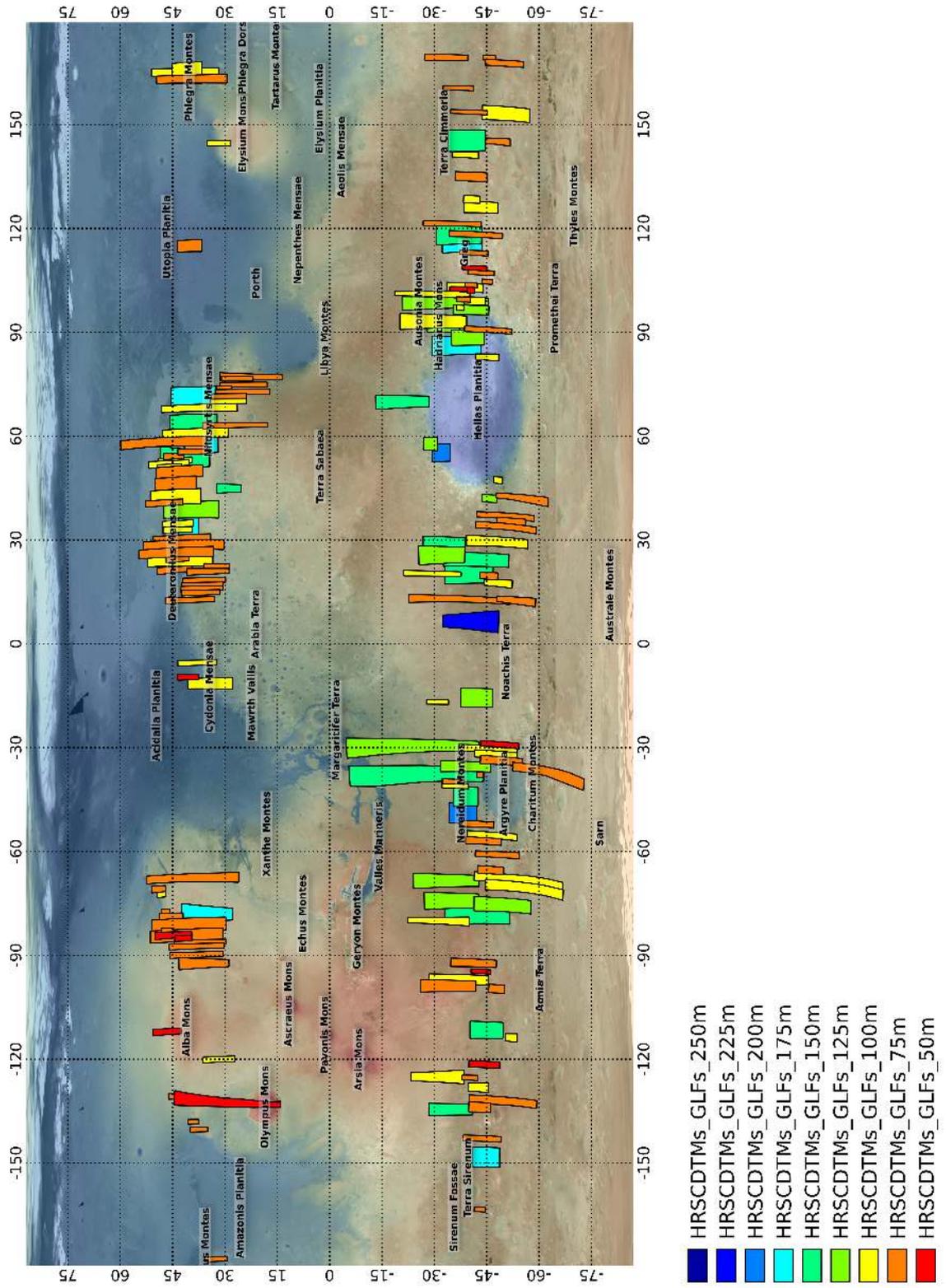
Figure 2.6: The HRSC DTM tiles underlying Souness GLFs colour-coded by resolution. See also table B.1.

25

which have not been publicly released.

2.9 Selected review of Earth-based automated DTM analyses

A common way of analysing topography, is by creating derived topographic layers from the DTM. This often uses differential geometry, and can include deriving the slope, most commonly the maximum slope, usually expressed as an angle relative to the horizontal. The aspect can also be derived, namely the direction in which a slope is facing. This can simply be an angle of azimuth relative to north, or can be a categorised layer often binned in 45° segments.

These calculations are implemented in a variety of GIS software, including the open-source GDAL (GDAL Development Team, 2014) software tools which includes the gdaldem package, which can derive slope from a DTM, as well as aspect, roughness, 'Terrain Ruggedness Index' and the 'Topographic Position Index'. In gdaldem, roughness is defined as the largest inter-cell difference of a central pixel and its surrounding cell, the TRI is the mean difference between a central pixel and its immediate surrounding cells, and the TPI is the difference between central pixel and the mean of its surrounding cells (i.e. similar to the TRI but also expressing the sign of the difference).

Iwahashi & Pike (2007) use an unsupervised nested-means algorithm, to segment the 1km resolution SRTM30 data for the entire Earth land surface, to 16 classes. Minár & Evans (2008) reviewed the theoretical basis of terrain segmentation, discussing what form segmentation of a continuous land surface should take, with a goal to distinguish segments that are genetically homogeneous, and the distinction between elementary and composite forms, which are composed of more than one elementary form. Approaches in land surface segmentation, may divided into 'graph-based' approaches, whereby the goal is explicitly delineating boundaries between segments, and a classification approach, which begins with the internal properties of landform elements. Analyses of digital terrain models of the Earth are useful for a variety of applications, including soil moisture modelling and geological studies. Some theory and applications are reviewed in, for example, Florinsky (2012).

2.9.1 Automated methods studying glaciers on Earth

Brown, Lusch & Duda (1998) used a supervised classification of a DEM and derived topographic variables, to examine glacial landform morphologies in Michigan related to Pleistocene glaciation defining six types of glacial landform and using a training set to train a classifier both with a maximum entropy or artificial neural network method. This kind of work has often been used to model soil moisture properties, for example for ecological modelling or agricultural purposes such as by MacMillan *et al.* (2000). In this case, a method was used with a fuzzy ruleset, to convert terrain attributes, such as slope, curvature etc. and measures of local relief, to landform classes. A similar method is used for an area in Austria by Van Asselen & Seijmonsbergen (2006).

Brenning & Trombotto (2006) studied glaciers and rock glaciers in the Andes, using a logistic regression method of terrain attributes including elevation, slope, and curvature layers, and derived quantities of contributing areas, making a prediction the general pattern of areas containing intact rock glaciers, exposed bedrock and debris surfaces. Brenning (2009) compares a number of different classification methods for debris-covered glaciers, and rock glaciers for a test site in the San Juan Mountains in Colorado, using both remote sensing images (Landsat ETM+) and terrain attributes, finding better results using both than either alone.

Romstad & Etzelmüller (2009) segment a DEM of an area of Adventdalen on Svalbard, containing both fluvial and glacial valleys, using a watershed segmentation of the mean curvature, and the inverse mean curvature, calculated by multiplying the curvature by -1. These two different segmentations are used to identify convex and concave segments, which are interpreted in context of landforms.

2.9.2 The machine-vision based 'geomorphons' method.

The 'geomorphons' method, developed by Jasiewicz & Stepinski (2013), uses a machine-vision based approach to analysing topography, by taking a point, and examining whether the line of sight, is above or below the horizontal, or within a tolerance to be considered flat in the eight directions at 45°. This draws on the definition of topographic openness described in Yokoyama, Shirasawa & Pike (2002), and which was applied in a supervised landform classification in Japan by Prima *et al.* (2006). The geomorphons method generates one of a number of

discrete geomorphons for each cell, which can be generalised to a smaller number expressing peaks, ridges, hollows, valleys, pits, passes, etc. The geomorphons method is available as an extension to the open-source GRASS GIS (version 7), or for small datasets, a web-based utility. (Jasiewicz & Stepinski, 2014).

2.10   Previous automated analyses of Mars data

There has been some work applying automated image and terrain analysis and classification methods to the Martian surface.

Impact craters have often been a focus, since they have a characteristic circular depression profile, and they are important as indicators of the age of a planetary surface, heavily cratered surfaces indicating an older age. A number of studies focusing on Martian data are Barata *et al.* (2004); Bandeira, Saraiva & Pina (2007); Bue & Stepinski (2007); Stepinski, Mendenhall & Bue (2009) and Plesko (2010).

Bue & Stepinski (2007) used thresholded maps of profile curvature, and a circular Hough transform, to detect impact crater candidates. The procedure takes the profile curvature of the DTM and create a binary image for a threshold value, then applying a morphological closing and thinning operation, followed by a Hough transform to identify circular features. Stepinski, Mendenhall & Bue (2009) use a two-step (topographic depression finding, followed by machine-learning crater-selecting) algorithm for identifying impact craters from circular depressions in MOLA 128 pixels/degree topography, using a training set. This work also measured crater depths. This work found a sudden decrease in the depth-diameter ratio of craters at latitudes $\gtrsim 38°$ S regardless of crater size, remarking that this could be due to the presence of subsurface ice.

Other features on Mars have been studied with automated methods, although not specifically glacier-related features:

Stepinski & Collier (2004) apply an automated analysis of topography to study valley networks on Mars, studying a set of old Noachian terrains, using an algorithm that first identifies pits in the DTM, and then fills them (a 'flooding' step), in order to restore flow continuity disrupted by craters, then determining the drainage direction, i.e. the pixel in the direction of the steepest slope, then calculating the area drained for each pixel, in order to determine the outlet. Stepinski & Vilalta (2005) used a pixel-based classification of a feature vector derived from a DTM of

the Tisia Valles region of Mars, calculating 'flooding', slope, 'flooded' slope, and total hypothetical drainage contributing areas for the raw and 'flooded' DTM, to construct a thematic map of the area.

Bue & Stepinski (2006) used a 'Digital Topography Model'[8] which organises a site's topographic data into a three-dimensional array consisting of several two-dimensional layers with each layer holding a different topographic attribute organized in a spatial grid common to all layers, to classify the Terra Cimmeria area of the Martian surface, using a pixel-based automatic minimum variance grouping method.

Stepinski, Ghosh & Vilalta (2006) use an object-based analysis of a feature vector, to classify a test site in Tisia Valles on Mars, segmenting by a homogeneity measure, combined with a watershed transform, and classifying objects into 6 landform classes with physical meaning using Support Vector Machines. Stepinski & Bagaria (2009) use what they describe as a 'stacked classification' which consists of a pixel-based classification, using the Iwahashi & Pike (2007) method, followed by capturing secondary features of the neighbouring area of a pixel, and combined into a feature vector, then a segmentation, based on the recursive hierarchical segmentation algorithm, applied to the Tharsis region of Mars. Ghosh, Stepinski & Vilalta (2010) presents a method using machine-learning techniques, to classify Martian surfaces, detailing choice of several different segmentation methods including K-means, and watershed-based methods, and several supervised learning based classification methods. In a similar way to Stepinski, Ghosh & Vilalta (2006), this work uses a feature vector incorporating slope, curvature, and a binary 'flood' variable, extending the study to several different sites and testing different classifiers. A manually labelled training set was used to classify the terrain into 6 landform classes.

The work of Bandeira *et al.* (2013) makes an automated search for a specific feature on the Martian surface, in this case aeolian sand dunes, based on the image gradient vector, both in searching high-resolution images for dunes, and classifying different types of them by morphology.

---

[8]This is abbreviated by the authors as DTM, however this can also be used for 'Digital Terrain Model' which at least for Mars may be used interchangeably with DEM (Digital Elevation Model) given the lack of vegetation or buildings.

Chapter 3

Methodology

3.1   Methods of topographic analysis

In this work, the the `LandSerf` (Wood, 2009) software[1] is used to calculate the derived topographic layers, which include slope, aspect and curvature rasters, which are related to the second derivatives of the DTM in both along slope and cross-slope directions. The aspect layer is processed using `gdalcalc`, to convert it to the absolute angle from north-facing, to deal with the issue that an aspect in degrees from $0°$ to $360°$ has a discontinuity.[2] A *Landscript* file can be used to automate the `LandSerf` software in calculating the derived layers for each tile.

The `LandSerf` software fits bivariate quadratic functions, to each grid cell, in order to evaluate a derived layer, such as slope, or a curvature layer. (Wood, 1998)

This work uses `LandSerf` to create the 'cross-sectional curvature', 'longitudinal curvature', 'profile curvature', 'plan curvature', and 'mean curvature' as derived layers. In addition, it has the facility to create a 'feature' map, which will delineate peaks, ridges, passes, pits, channels and planar terrain at a given windowing size.[3] In this work, a windowing size of 3 cells is used throughout to create derived topographic layers.[4] The 'cross-sectional' and 'longitudinal' curvature layers are used for further segmentation work in `RSGISLib` since to include more curvature layers would essentially duplicate information already present, and increase com-

---

[1]Another researcher, Igor V. Florinsky, had previously created a software called 'Landlord' for topographic analysis. (Florinsky, 2014)

[2]This has the limitation of removing any east-west information.

[3]Note that this feature map may change according to the windowing scale, see Fisher, Wood & Cheng (2004).

[4]See sections 5.10.2 and 5.11.2 for discussion of the issue of scale in topographic analysis, and approaches that may be taken in responding to these issues.
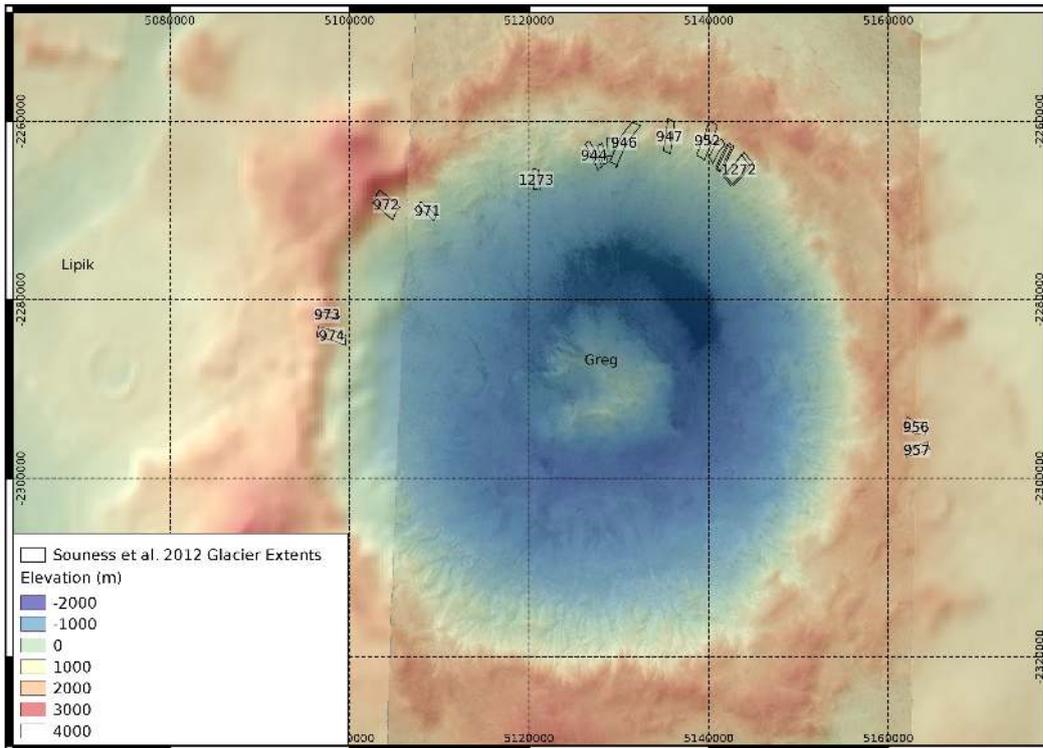
(a) Elevation
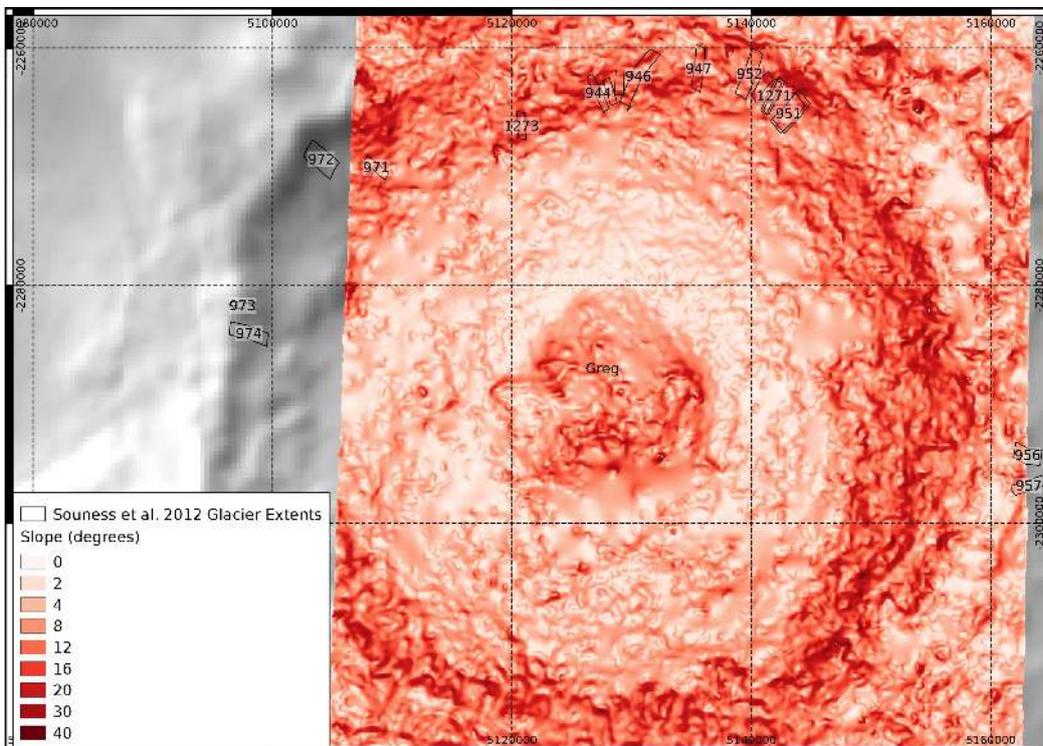
(b) Slope

Figure 3.1: Crater Greg, showing the elevation and slope with Souness GLF extents overplotted. The elevation is overplotted via transparency on the nadir image.

putational time. The longitudinal and cross-sectional curvatures are defined as the curvature parallel and orthogonal to the 3-dimensional steepest slope vector respectively. (Wood, 1996). An example of the slope layer in crater Greg on Mars can be seen in figure 3.1. Examples of the curvature layers, showing the longitudinal and cross-sectional curvature layers in the north wall of crater Greg are shown in figure 3.2.

3.2   Software tools used

One way of visualising locations on Mars is to use Google Earth. It is possible to use a Mars globe, and overlay options of Mars Express imagery in optical or infrared, colourised MOLA elevation, or Mars Reconnaissance Orbiter CTX camera mosaics. See figures 3.3 and 3.9.

Using the table of 'glacier-like forms' identified by Souness *et al.* (2012) and available as a table in the supplementary information to the paper, it is possible to create a 'Google Fusion Table' with the locations in Mars latitude and longitude, and export this to a KML file suitable to visualise in Google Earth.

A further technique applied to the Souness data, is to use the Python Shapefile Library (`pyshp`) to create shapefiles of the glacier extents, using the specified centre, head, terminus and left and right mid-channel locations, assuming a constant channel width. In addition, 'context' shapefiles are also created by expanding the object by a factor of three from its centre in each dimension, thus creating an area 9 times the extent. The head and termini locations were buffered by 100m, to create small areas around these for further analysis, and the heads also buffered by 5km to allow a direct comparison to the analysis of Souness *et al.* (2012). These shapefiles can also be exported to KML format to view in Google Earth. See figure 3.3.

`RSGISLib` is used to extract zonal statistics of the derived topographic layers for these shapefiles. The minimum, maximum, mean and standard deviation are calculated for the each of the of the layers for each object.

The 'Filtergraph' website was used to visualise the locations of GLFs, and quality of DTM coverage, plus the metadata provided by Souness e.g. length, width, elevation etc. Filtergraph provides a convenient graphical front-end to the Python `matplotlib` plotting library. (Burger *et al.*, 2012).
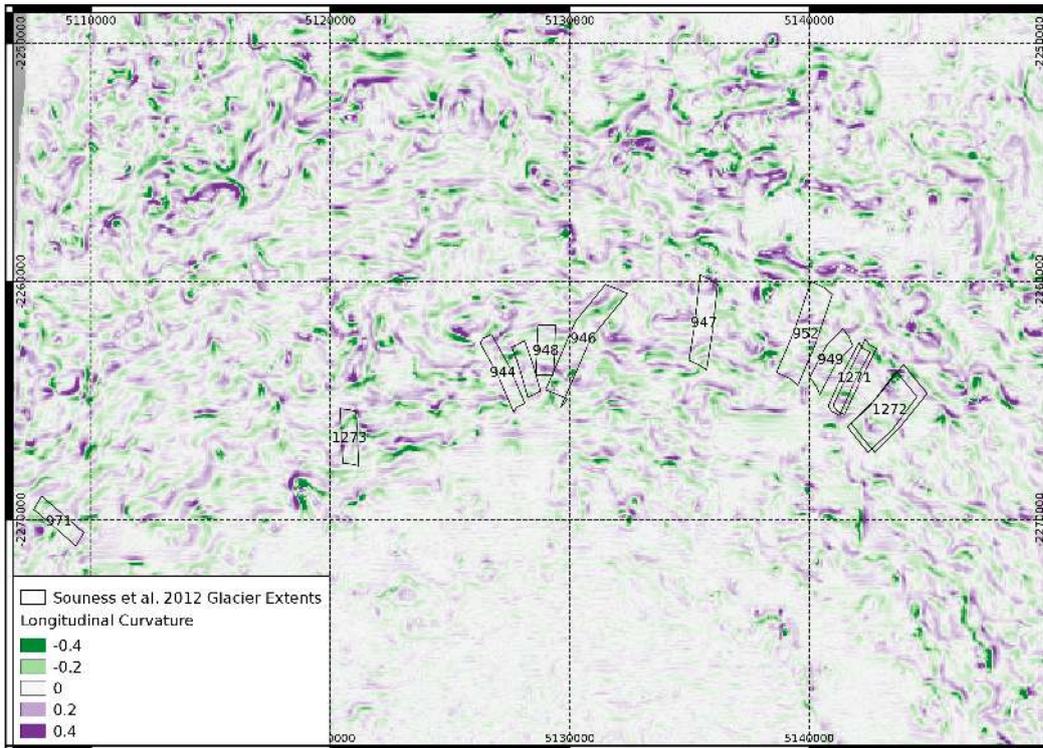
(a) Longitudinal Curvature
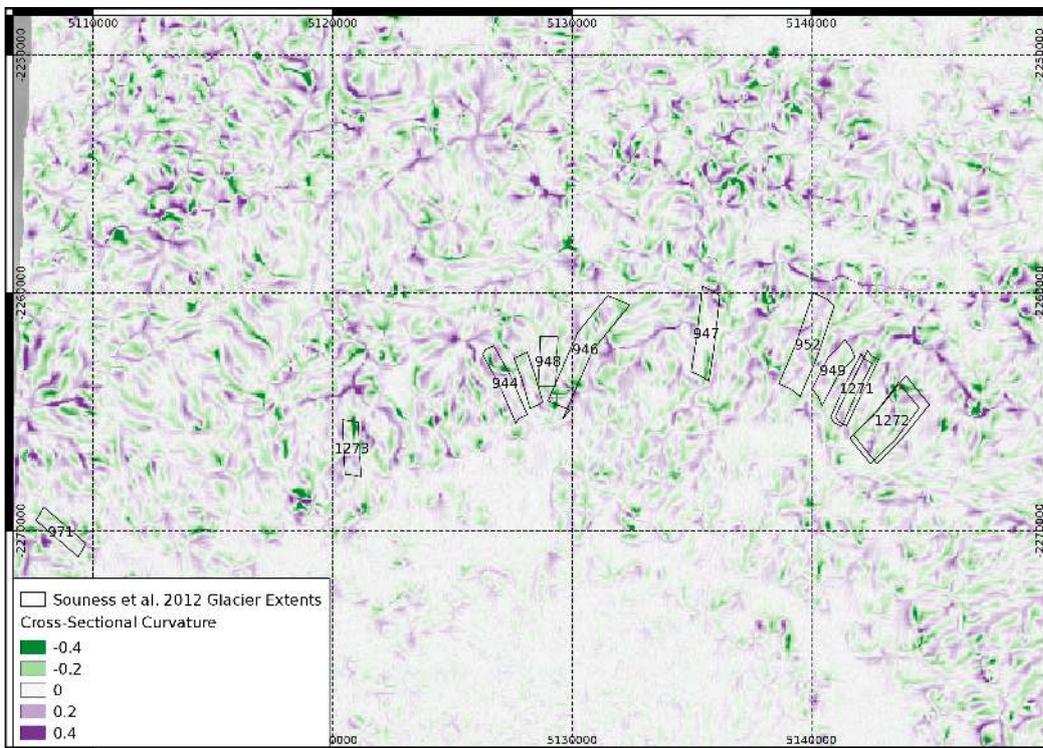
(b) Cross-sectional Curvature

Figure 3.2: The curvature layers, calculated in `LandSerf`, the longitudinal curvature expressing the convexity or concavity of a slope, and the cross-sectional curvature defined perpendicular to the slope.
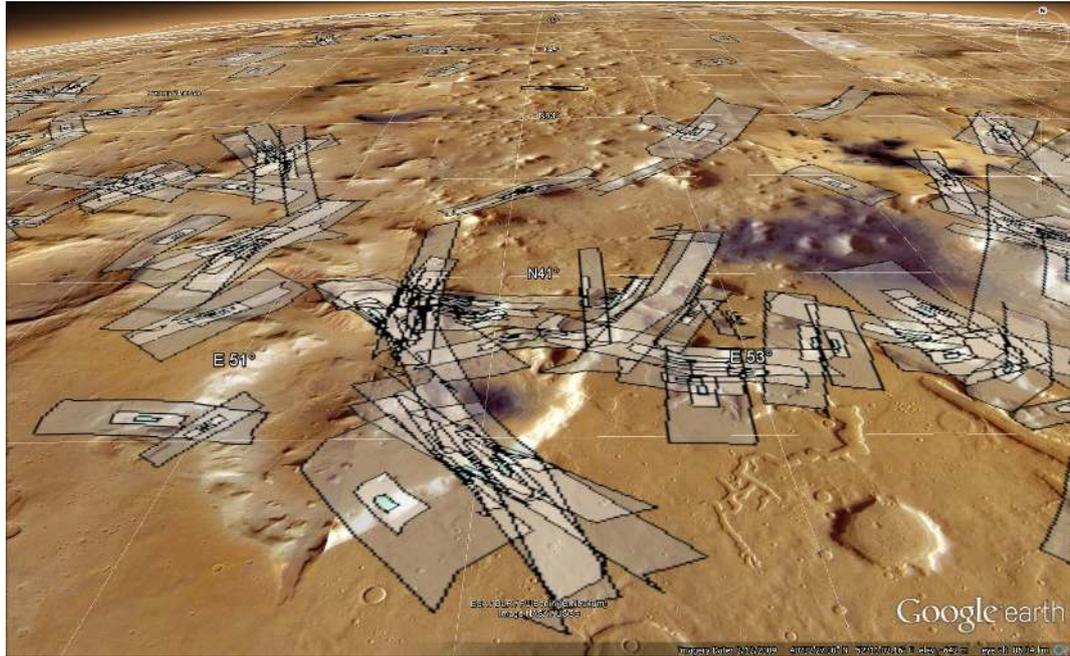
Figure 3.3: A Google Earth screen shot, showing the Souness GLFs, 'context' and 'context9' shapefile extents in the Protonilus Mensae region of Mars.

3.3 Collecting topographic data

Beginning with the Souness *et al.* (2012) inventory of glacier-like forms (GLFs), which lists 1309 candidate glaciers identified by visual inspection of CTX images, the first step was to identify coverage by HRSC stereo DTMs and HiRISE images, anaglyph, and DTM data.

This was done using the Mars Orbital Data Explorer (Planetary Data System Geosciences Node, 2014), checking whether the coordinates of the GLF centre have HRSC DTM coverage, and identifying the best resolution tile where more than one DTM tile underlies it, also flagging HiRISE images and anaglyphs either of the object or in close proximity.

See Appendix A for maps covering the mid-latitudes of Mars in both hemispheres, indicating the locations of the HRSC tiles and their context in overall topography.

3.4 Data pre-processing and processing

A set of flowcharts expressing the steps involved in pre-processing, processing, constructing the classifier, and evaluation of results are shown in figures 3.4, 3.5,

3.6, 3.7 and 3.8.

3.4.1   Pre-processing

The pre-processing steps are detailed in the flowchart in figure 3.4. The HRSC DTM tiles covering each Souness GLF are identified as described earlier, and the nadir image, and the areoid DTM downloaded for each. Using a Mars equicylindrical projection, set at a standard parallel of 40°, to match the modal latitude of the GLFs, the HRSC DTMs are reprojected into a common coordinate system, which allows comparison across the full dataset available.

    Landscript scripts are generated to use `LandSerf` to create derived topographic layers from each of the 179 HRSC DTM tiles.

    A layerstack is created using `GDAL` of the nadir image from HRSC, resampled to the DTM resolution, the elevation and the derived topographic layers. This creates both the 10 band layerstack, which additionally includes profile, plan, and mean curvature, and a 'feature' layer, as well as the 6 band layerstack including the image resampled to DTM resolution, elevation, slope, absolute aspect angle from north, cross-sectional, and longitudinal curvature.

3.4.2   Processing

The 6 band layerstacks, are segmented using Python `RSGISLib`, (Bunting & Clewley, 2014), using the `runShepherdSegmentation` function in the `rsgislib.segmentation` module. This function uses the segmentation algorithm of Shepherd, Bunting & Dymond (2014). The minimum object size is set to 0.2 square kilometres, which is calculated for each HRSC tile in terms of the number of pixels that falls closest to this value, due to the variable pixel scale.

    The attribute table is populated with local statistics for the segments, and converted to vector polygons using `GDAL`, and the raster attribute table output to a text CSV file. It is then possible to use GIS software to join the vector shapefile to the raster attribute table, and explore the data by selecting segments by attribute. See figure 3.5 for a flowchart describing this.

    Using `pyshp`, shapefiles corresponding to the extent, context, context9 (expanding the dimensions by a factor of 3 and 9 respectively keeping the same centre) areas, as well as 100m radius buffers around the listed head, centre and terminus locations are created. These are used to calculate zonal statistics of the
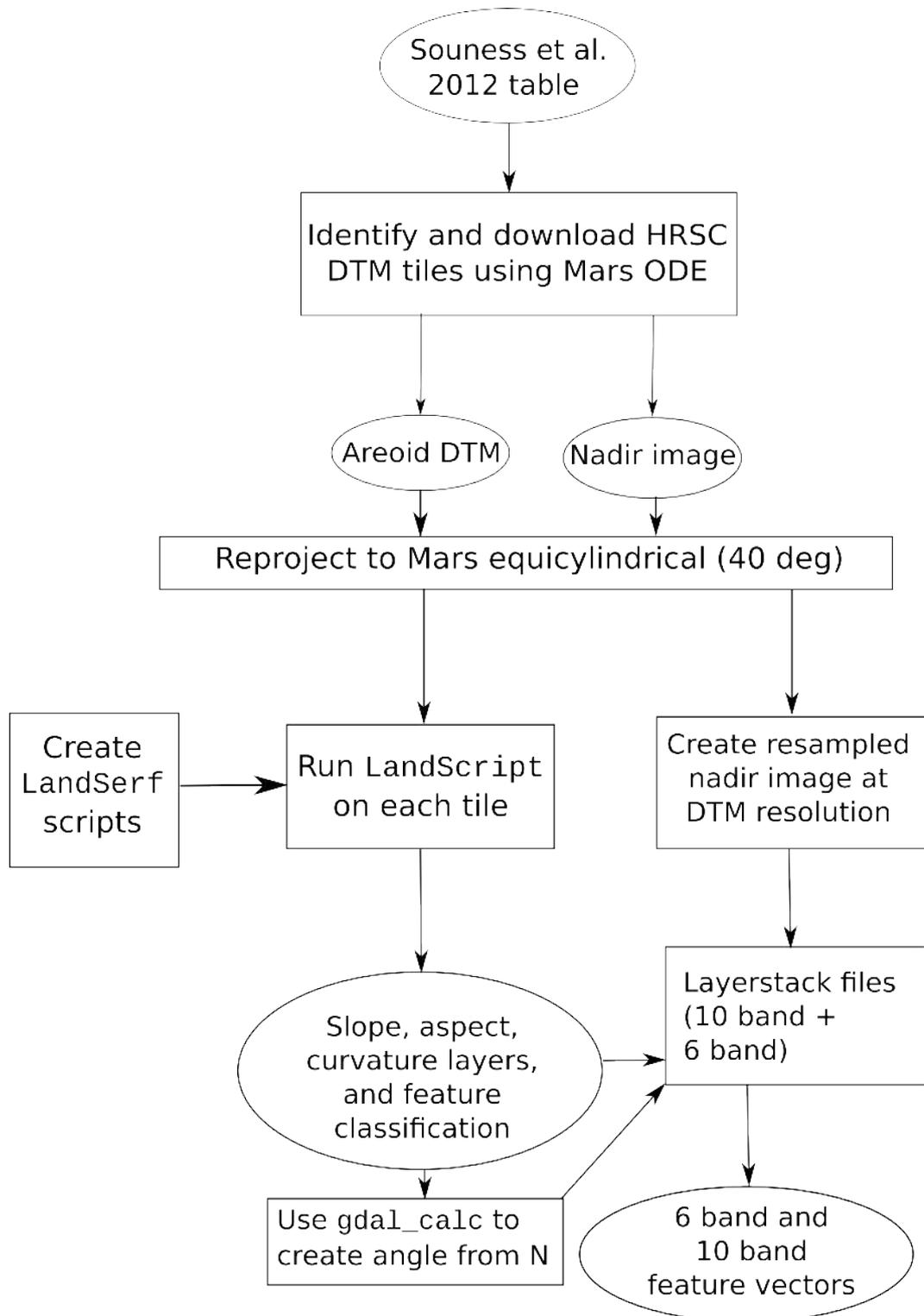
Figure 3.4: A flowchart showing the pre-processing steps in creating the layer-stacked feature vectors.
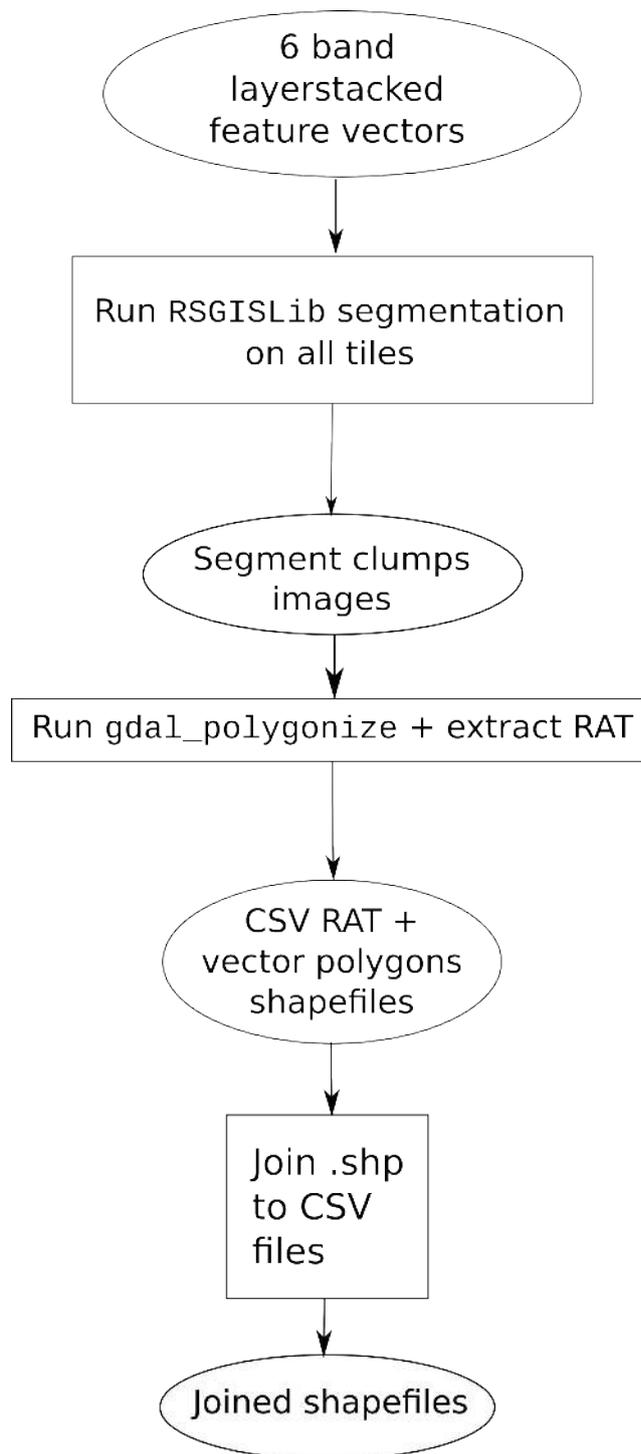
Figure 3.5: A flowchart showing the processing steps involved in running `RSGISLib` on the tiles and creating vector shapefiles of the output.
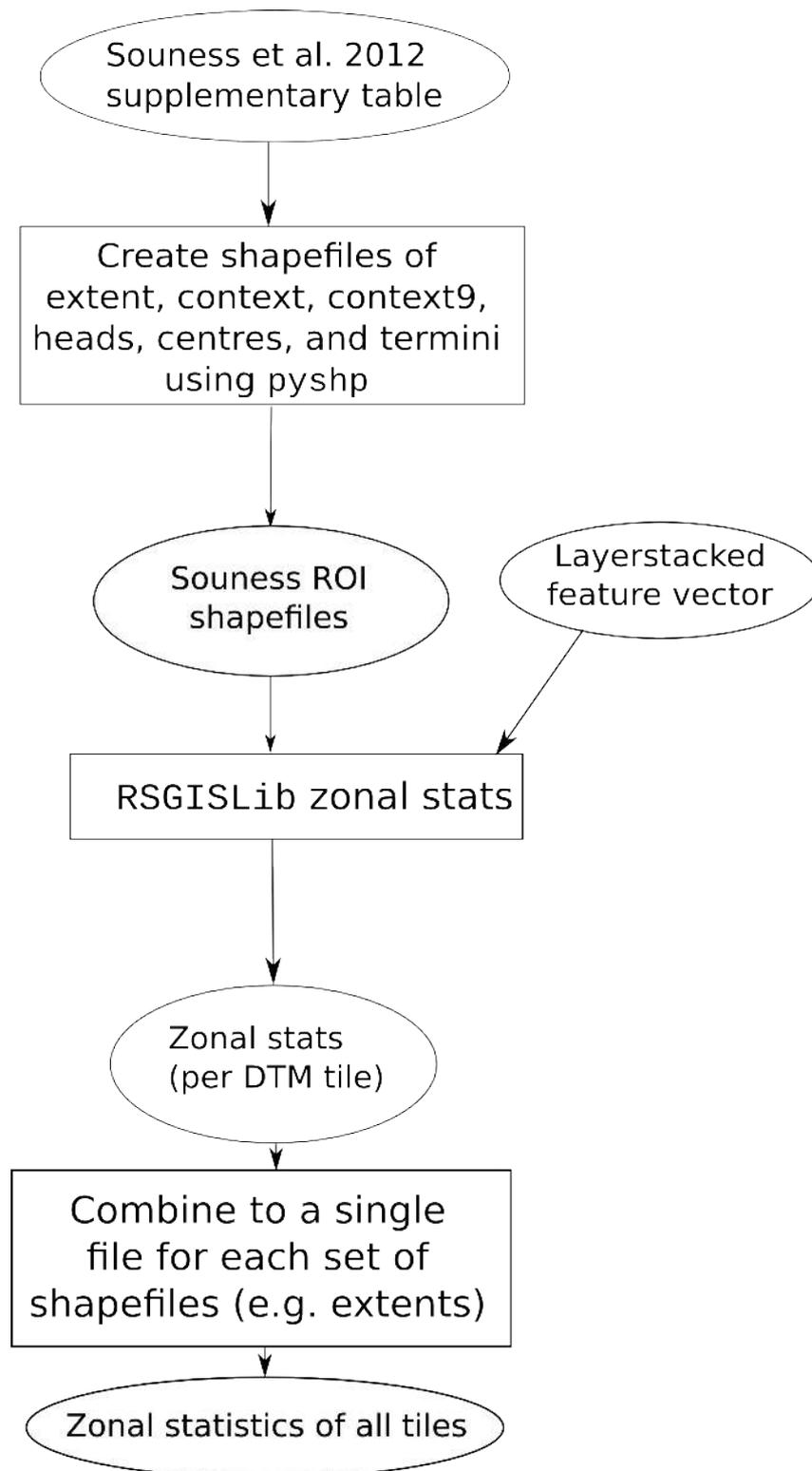
Figure 3.6: A flowchart showing the processing steps involved in creating zonal statistics.
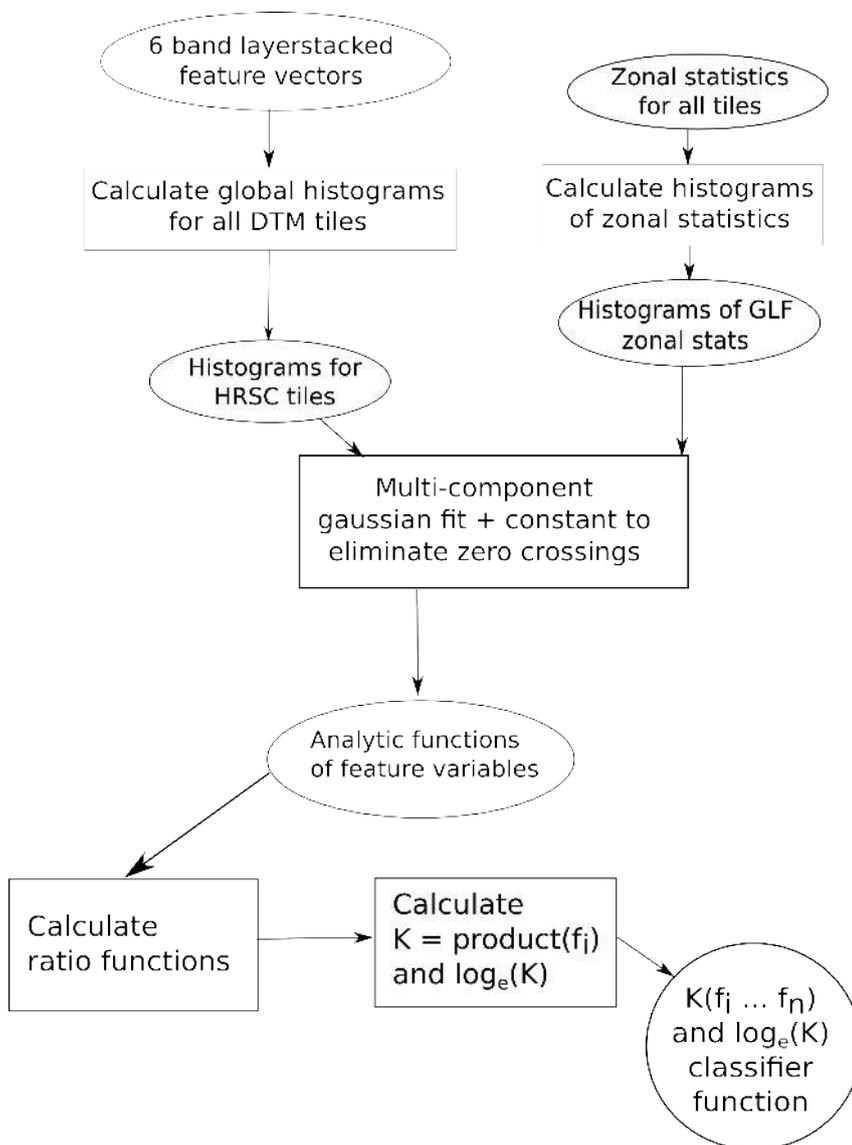
Figure 3.7: A flowchart showing the processing steps involved in creating the classifier function.
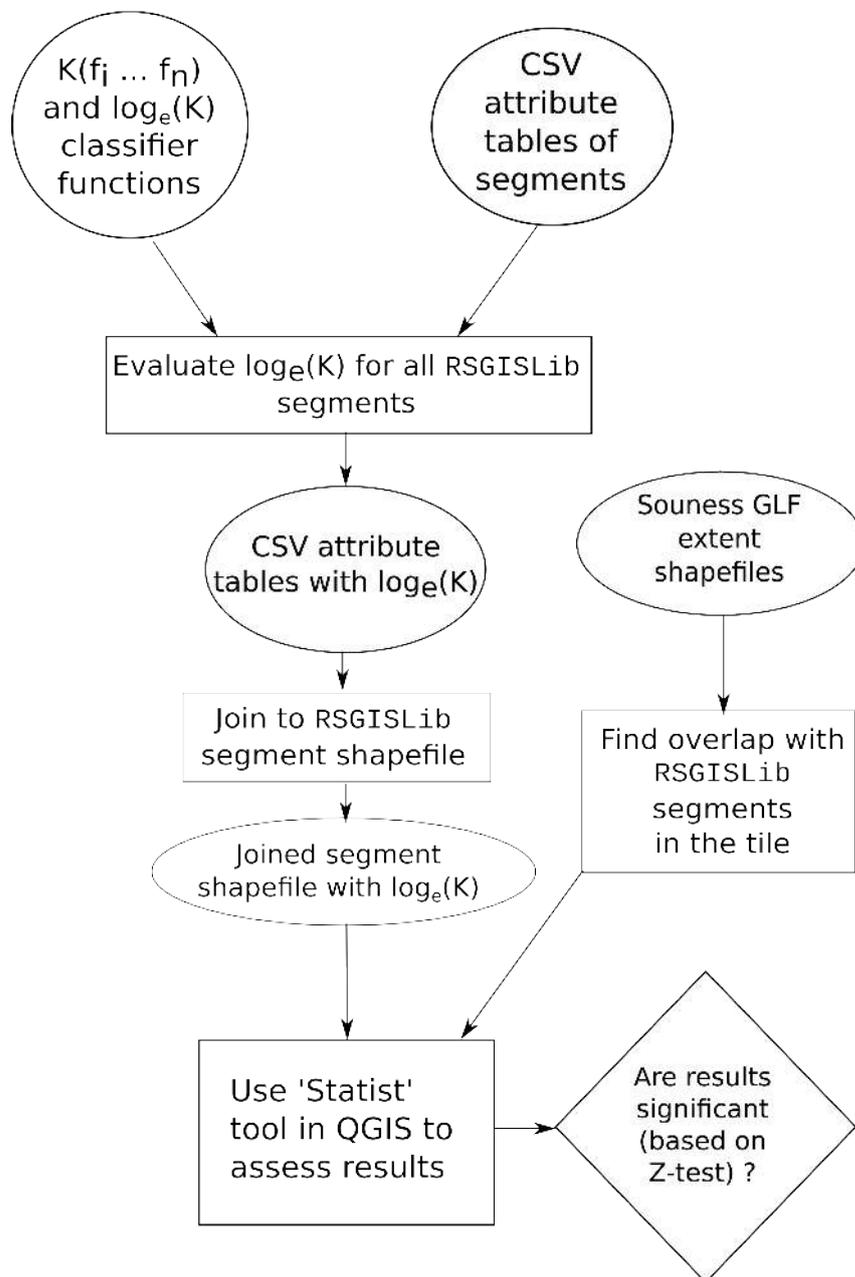
Figure 3.8: A flowchart showing the processing steps involved in evaluating the results from the classification function.
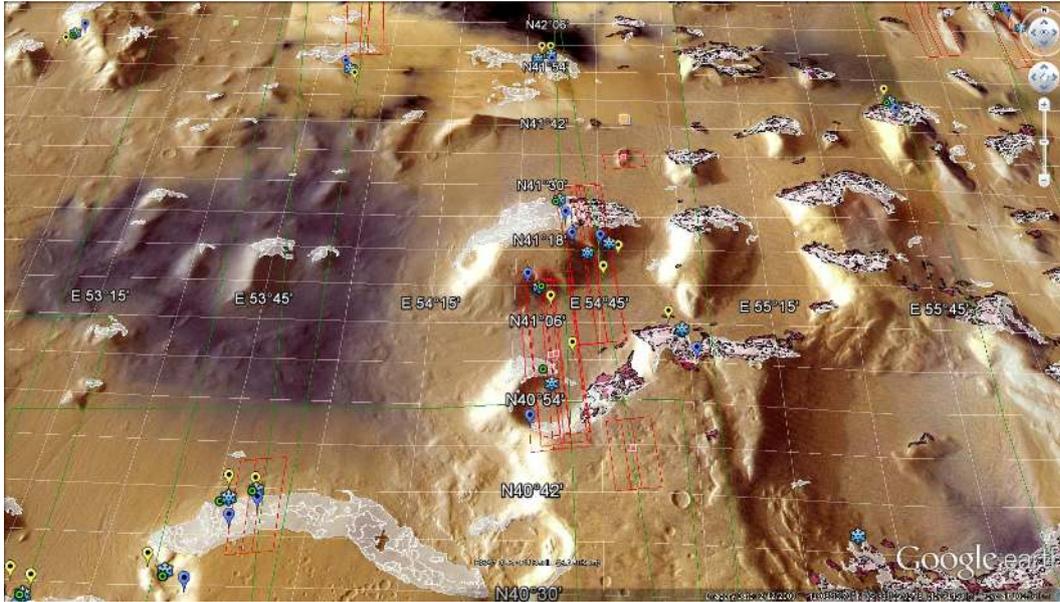
Figure 3.9: An area of Protonilus Mensae, showing areas where segments are selected for having a northerly aspect and a relatively steep slope of more than 10 degrees. In this figure the head and termini locations are marked with blue and yellow markers respectively, and the centre with a snowflake.

layerstacked feature vector. These statistics are first created per DTM tile, and are combined using a Python script to a combined list indexed by the Souness catalogue number. See figure 3.6.

A simple rule based selection could be made, for example see figure 3.9 where segments are selected based on their zonal statistics, e.g. having a north-facing slope (in northern hemisphere areas). However, hard windowing by elevation, slope, aspect etc. in a rule based classification would both reject many genuine objects, and classify other areas spuriously as glaciers, since the distributions of the variables are not separable. Therefore, the approach taken below is a 'fuzzy' classifier.

3.5   Constructing a fuzzy classifier

A 'fuzzy' classifier is constructed based on comparing the histograms of the topographic variables for the Souness GLFs, considering either the extents, contexts, or the 100m or 5km head area buffers and comparing the histograms of the variables for the zones to those for the HRSC tiles as a whole. The histograms and abundance ratio plots are reproduced here for the extent and 100m head shapefiles in

figures 4.1 and 4.2.

The histograms of counts of Souness GLFs as functions of each variable of nadir image brightness, elevation, slope, absolute deviation of aspect from north, cross-sectional curvature, and longitudinal curvature are calculated, as well as the histograms of all pixels in the layerstacks of the HRSC DTM tiles that are used in the analysis (see table B.1 for a list), summing by area. See figures 4.1, and 4.2.

It is then possible to fit a curve to these histograms so that the counts (or areas per unit variable) are calculated as functions of the variables. This is accomplished using Python `scipy`, using a multi-component Gaussian plus a hard-coded fixed constant. The fixed constant avoids zero-crossings. It is necessary to fine-tune the range in which the fit is calculated, to prevent large spurious values at the edges of the range of the variable. Following this, ratios of GLF counts divided by the total area in the HRSC tiles are calculated as functions of the variables. See figure 4.3.

A classifier function $K = \prod^{i} f_i$ can be constructed by taking the product of each of the ratio functions. A larger value of K indicates the segment better approximates the characteristics of the Souness GLFs in some way or other. The further analysis uses $\log_e(K)$ due to its construction as a product. See figure 3.7 for a flowchart detailing the classifier construction.

The values of the ratio functions, and of K and $\log_e(K)$ are calculated and added to the CSV attribute tables for each tile, so they can be joined using GIS software to the vector polygons and values of the classifier examined spatially. See figure 3.8 for a flowchart describing this process.

Chapter 4

Results

4.1 Summary of descriptive statistics

See figures 4.1 to 4.4 showing the histograms of the image brightness and topographic variables comparing for the averages over the GLF extents, and the overall distributions across all of the HRSC tiles used.

4.1.1 Nadir image brightness

The nadir image brightness, in shown in figure 4.1a tends to be brighter for the Souness glacier extents than the overall distribution across all of the HRSC tiles. The ratio of the nadir brightness areas of interest to HRSC coverage is stronger for the 100m head buffers, than the extent buffers.

4.1.2 Elevation

The overall elevation histogram (figure 4.1f) for the HRSC DTM tiles shows a bimodal distribution with peaks at ~ -2500m and $\sim +1000$m, of which the peak at $+1000$m is the larger.

The Souness extents again show a bimodal distribution, except that the peaks are at ~ -1500m and $\sim +500$m, and the -1500m peak is the larger. See figure 4.1d. The minimum between the two peaks occurs just below 0m, instead of $\sim$ -1000m as it does for the HRSC DTM tiles. A distribution made for the context areas shows a similar form to that for the extents.

Relatively speaking, there are fewer Souness glaciers at the very lowest and the very highest elevations. Souness *et al.* (2012) remarked upon an observed depletion

(a) Image (Extents) (b) Image (Heads) (c) Image (overall)

(d) Elevation (Extents) (e) Elevation (Heads) (f) Elevation (overall)

(g) Slope (Extents) (h) Slope (Heads) (i) Slope (overall)
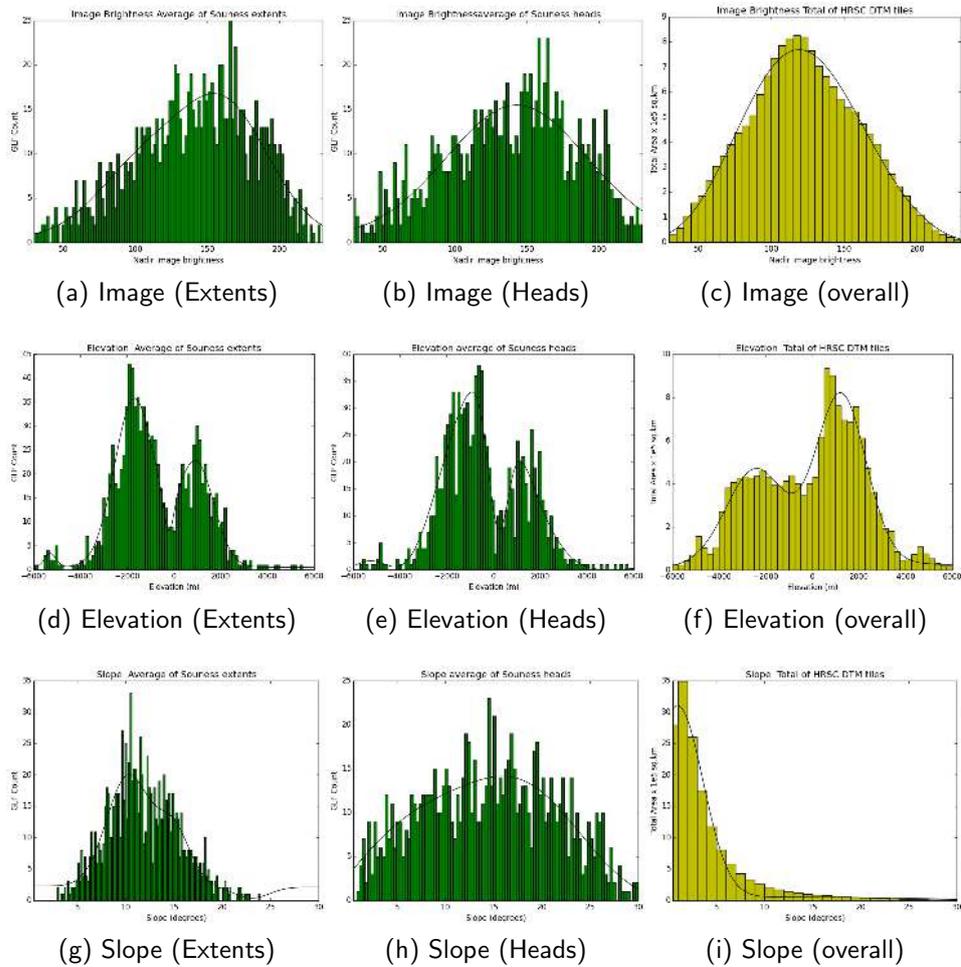
Figure 4.1: Histograms showing average brightness of nadir image, elevation, and slope over Souness GLF extents, over 100m radius buffers around Souness head locations, and over all pixels summed by area in the HRSC DTM tiles.

46

(a) Aspect N hemisphere (Extents)   (b) Aspect N hemisphere (Heads)

(c) Aspect S hemisphere (Extents)   (d) Aspect S hemisphere (Heads)

(e) Extents crs. curvature (f) Heads crs. curvature (g) Overall crs. curvature

(h) Extents lgt. curvature (i) Heads lgt. curvature (j) Overall lgt. curvature
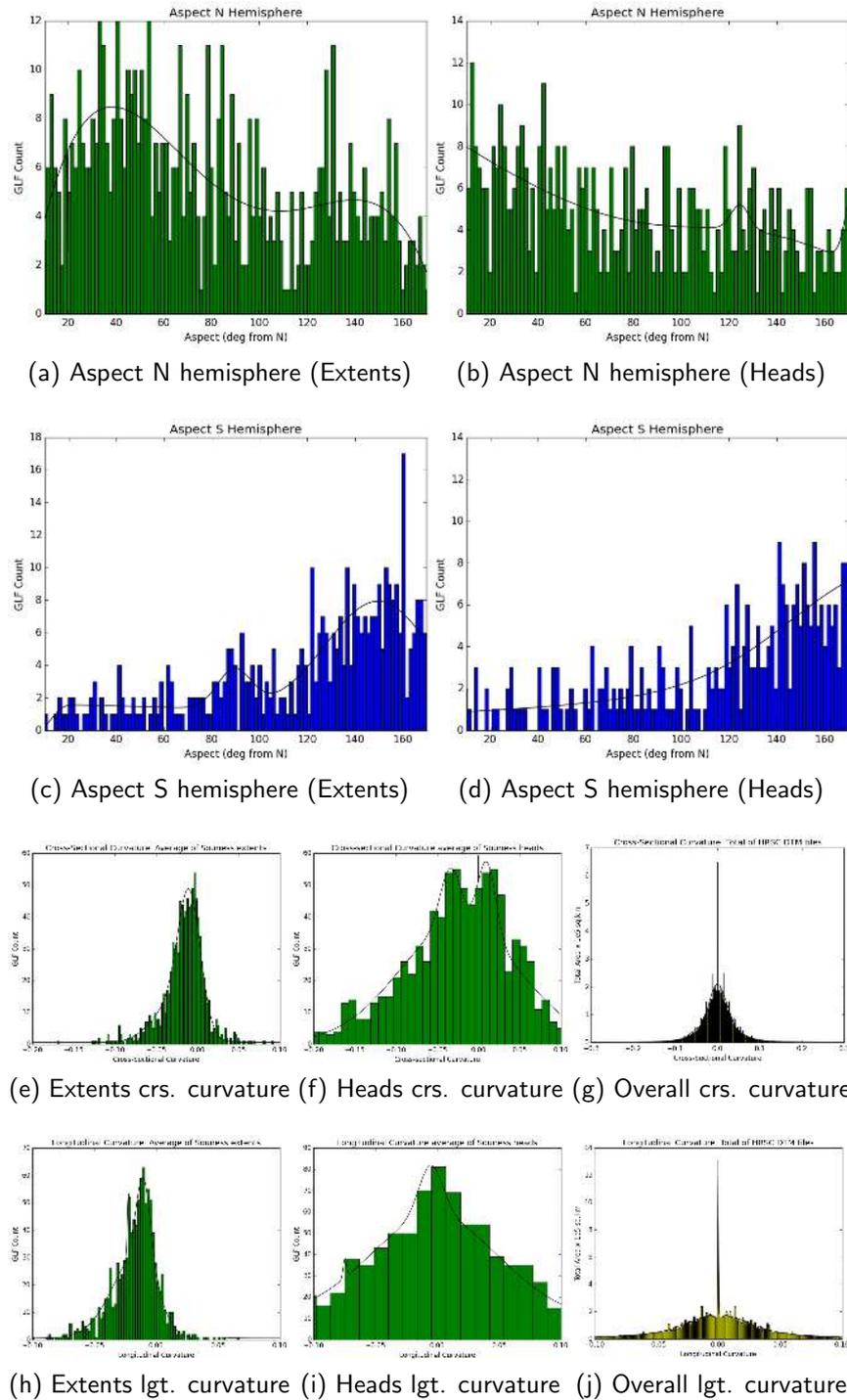
Figure 4.2: Histograms showing average aspect angle from N over Souness GLF extents and heads, in both northern and southern hemispheres, and of the curvature layers for Souness GLF extents and heads and for the HRSC tiles overall. Note that the Souness GLFs have a bias towards negative curvature, whereas the overall data has a symmetric distribution about zero.

(a) Nadir Image   (b) Elevation   (c) Slope

(d) Aspect (N hemisphere)   (e) Aspect (S hemisphere)

(f) Longitudinal Curvature   (g) Cross-sectional Curvature
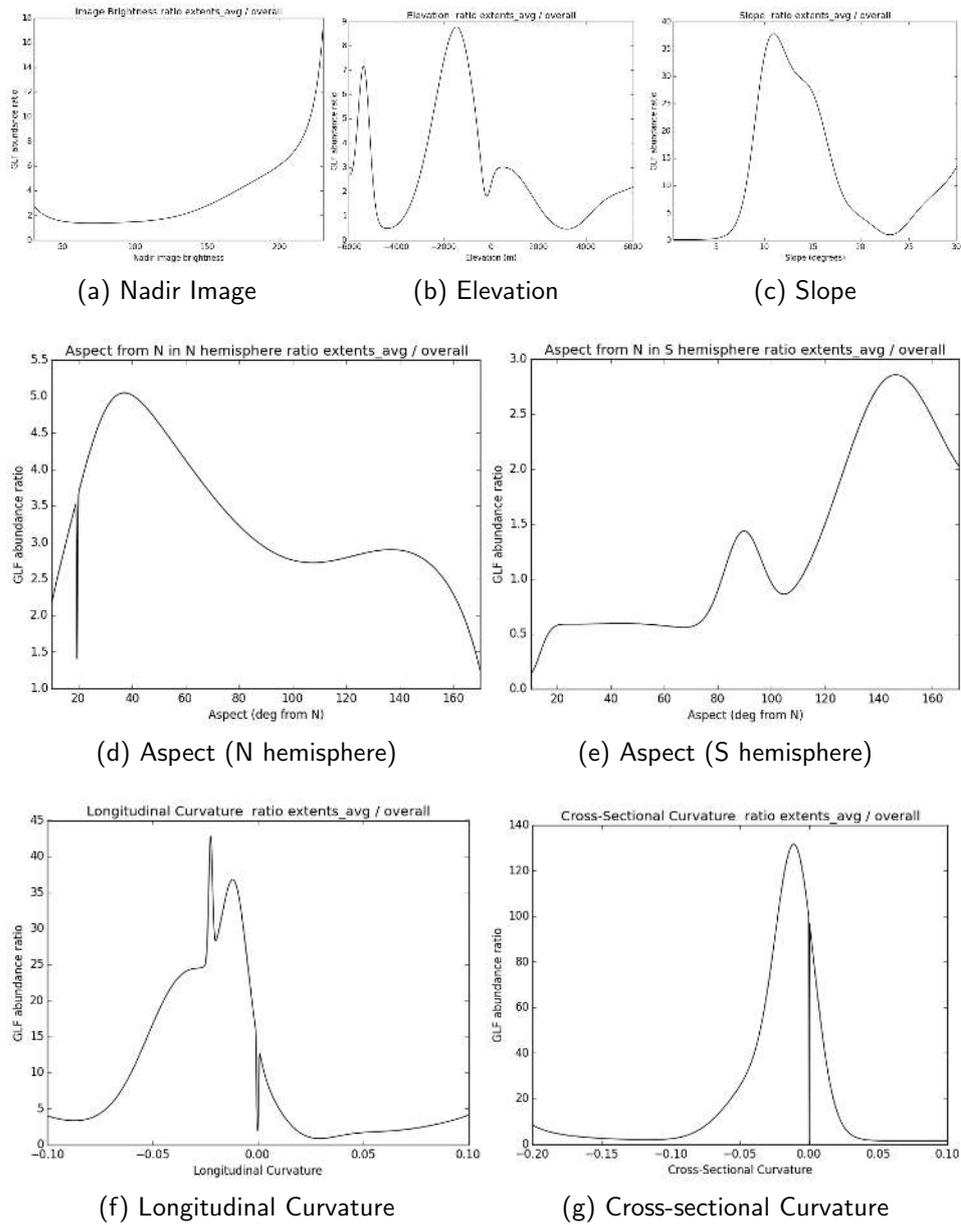
Figure 4.3: Ratio of Souness GLF counts to overall HRSC histograms as functions of feature vector variables - extents.

(a) Nadir Image

(b) Elevation

(c) Slope

(d) Aspect (N hemisphere)

(e) Aspect (S hemisphere)

(f) Longitudinal Curvature

(g) Cross-sectional Curvature
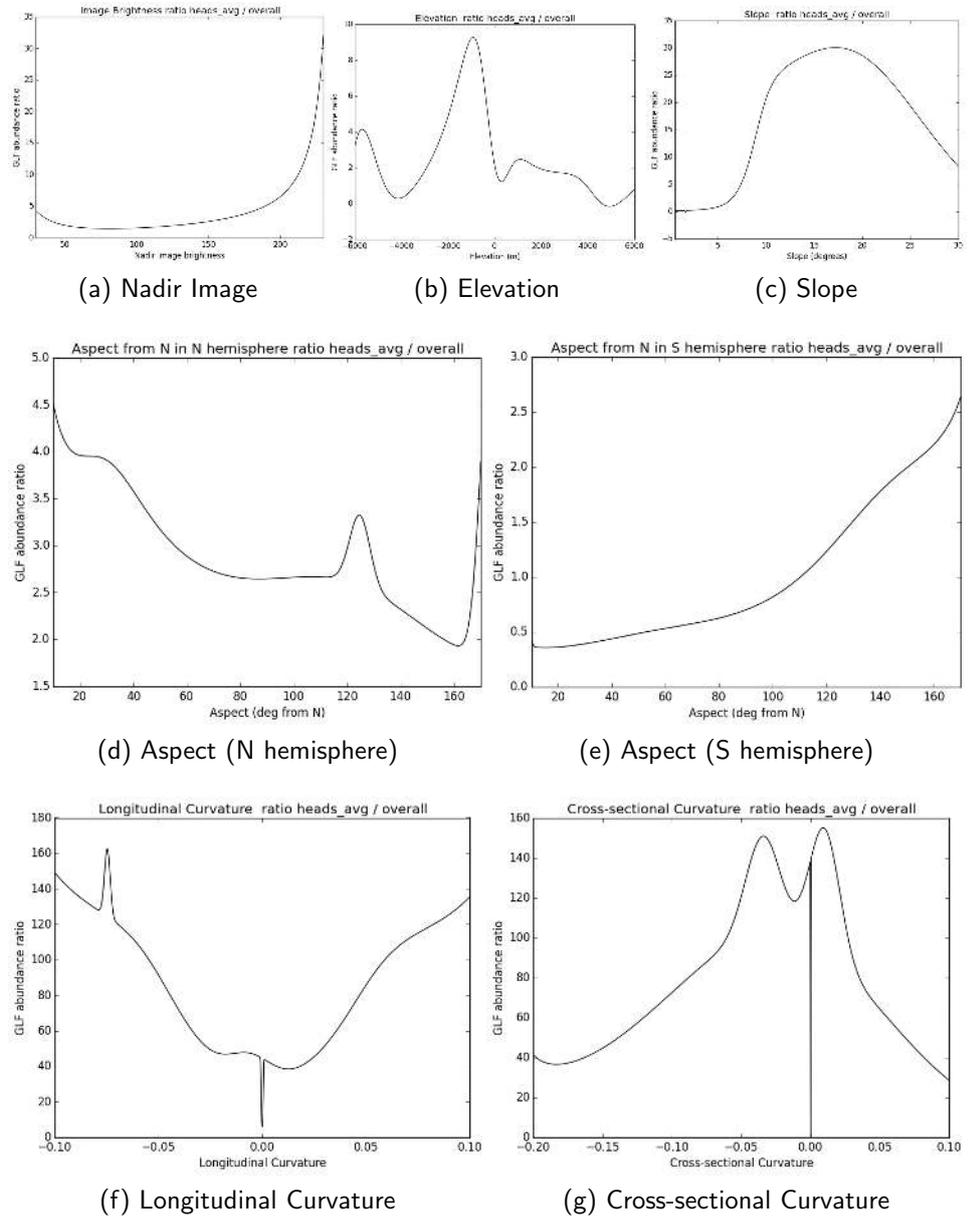
Figure 4.4: Ratio of Souness GLF counts to overall HRSC histograms as functions of feature vector variables - 100m radius head buffers.

of glacier-like forms below an elevation of -3000m, which could be attributed either to lack of formation or poor preservation.

The head areas show wider peaks; an effect of the much smaller area[1] over which the elevation is measured such that local variation plays more of a role in determining the statistics; and a general shift of the peaks to higher elevations.

The 5km head buffers, created to allow a direct comparison with Souness *et al.* (2012) results that used MOLA elevation, show a similar elevation distribution to that was found in that work.

The 'context' buffers, which have an area 9 times that of the GLF extents, have a similar elevation histogram to that of the 5km head buffers, except that the 5km head buffers are shifted to higher elevations, as we should expect given these are down slope flow features.

4.1.3 Slope

The overall slope histogram (figure 4.1i) of the HRSC DTM tiles shows a peak at $1-2°$ and decay at larger slope values. The Souness GLFs, averaged over extents, show a peak at 10-15°. (figure 4.1g). There are very few with average slopes of 5° or less. This should be expected given that these objects are defined as objects where Souness *et al.* (2012) saw evidence for down slope flow.

These objects tend to occur in areas with a high abundance of steep slopes, since the context histograms also show a peak around 10°. The context9 areas, show a peak shifted to lower slopes, as expected if the expanded areas include flatter areas, but nevertheless, there are still few with an average slope of $\lesssim 5°$, showing that the objects have a tendency to occur in areas where there is more high relief in surrounding areas, rather than in isolated mesas.

The heads slope histogram (figure 4.1h) shows a much broader distribution, centred around 15° with a larger variance than the extents. As a ratio, the peak is around 17°.

4.1.4 Aspect

The DTM tiles., on average show a relatively flat curve for aspect, as may be expected.

---

[1]The head areas have a buffer of 100m around the Souness *et al.* (2012) location, whereas the median extent area of the GLFs is 1.1 km^2

In the northern hemisphere, there is a tendency towards GLFs being found on north-facing slopes and in the southern hemisphere towards south-facing slopes. However, in neither case are the GLFs exclusively found on poleward-facing slopes. The southern hemisphere appears to show a stronger suppression of glaciers on equatorward facing slopes. See figures 4.2a, 4.2b, 4.2c, and 4.2d. These trends broadly match those for orientation in Souness *et al.* (2012). The correlation between Souness' orientation, processed to the absolute angle away from north, and the aspect averaged over extents can be seen in figure 4.5.
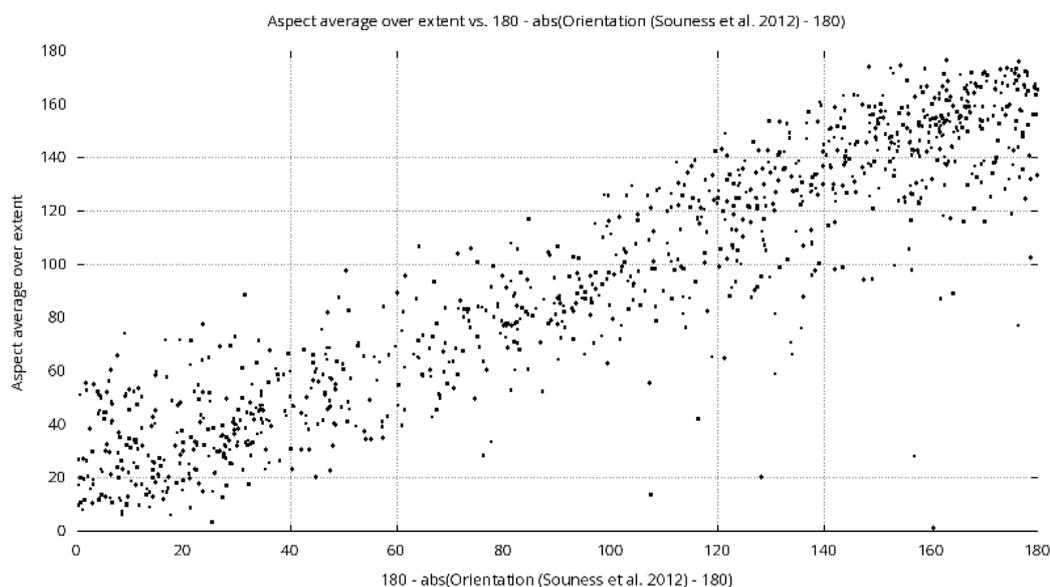
Figure 4.5: The Souness *et al.* (2012) orientation, converted to absolute angle from north, plotted against the average aspect angle from north over the GLF extents.

4.1.5 Cross-sectional curvature

The general trend for the HRSC tiles as a whole, is for the distribution to be centred around zero. In contrast, the extents show a bias towards negative numbers, which is consistent with these features being found in topographic hollows, or features like cirques. See figures 4.2e, 4.2f and 4.2g.

4.1.6 Longitudinal curvature

The general trend for the HRSC tiles as a whole, is for the distribution to be centred around zero. In contrast, the extents show a bias towards negative numbers, i.e.

concave slopes, which fits the model of these objects as having steep slopes which become shallower as the flow progresses as was described in Hubbard *et al.* (2011). See figures 4.2h, 4.2i, and 4.2j.

4.2 RSGISLib segmentation and statistics of individual HRSC tiles

Due to the large number of HRSC tiles, it is not possible within this work to discuss the results from all tiles. This work will focus on particular tiles, choosing first areas in both hemispheres with 50m resolution topography with a large number of Souness GLFs. Following this, some tiles with 75m topography are discussed that also are well-populated with GLFs and have had some previous study in the literature for comparison. The locations of tiles are displayed on the global maps in Appendix A and listed in table B.1. Note that not all tiles are labelled on the maps since QGIS automatically avoids label overcrowding.

4.2.1 East of Hellas: Tiles with 50m resolution DTM data

This work selects tiles h2279 and h0248 located to the east of Hellas Planitia, in the southern hemisphere. See figure 4.6 for an overview of these tiles, and figure A.11 for location map in broader context.

Tile h0248

This tile is located at 35-40°S, and 102°E. There are 8 Souness catalogued GLFs within the tile. A portion of the tile segmented using RSGISLib is shown in figure 4.7. The values of $\log_e(K)$ for the segments, calculated both based on features of extents, and of the 100m radius buffer around the head, are shown in the histograms in figures 4.8 and 4.9.

Since for any of the tiles used, the number of segments in the whole tile vastly exceeds the number of segments intersecting Souness GLF extents, to estimate the statistical significance of the larger value of $\log_e(K)$ in the intersected segments, a one-sided $Z-$test is used, which calculates $Z = \frac{(\bar{x}-\mu_0)\sqrt{n}}{\sigma_0}$ where $\bar{x}$ is the mean of the $\log_e(K)$ for the intersecting segments, μ_0 and σ_0 are the mean and standard deviation of $\log_e(K)$ of the whole set of segments in the tile and n is the number of intersecting segments. The value of the Z statistic is 5.58 in this case, which
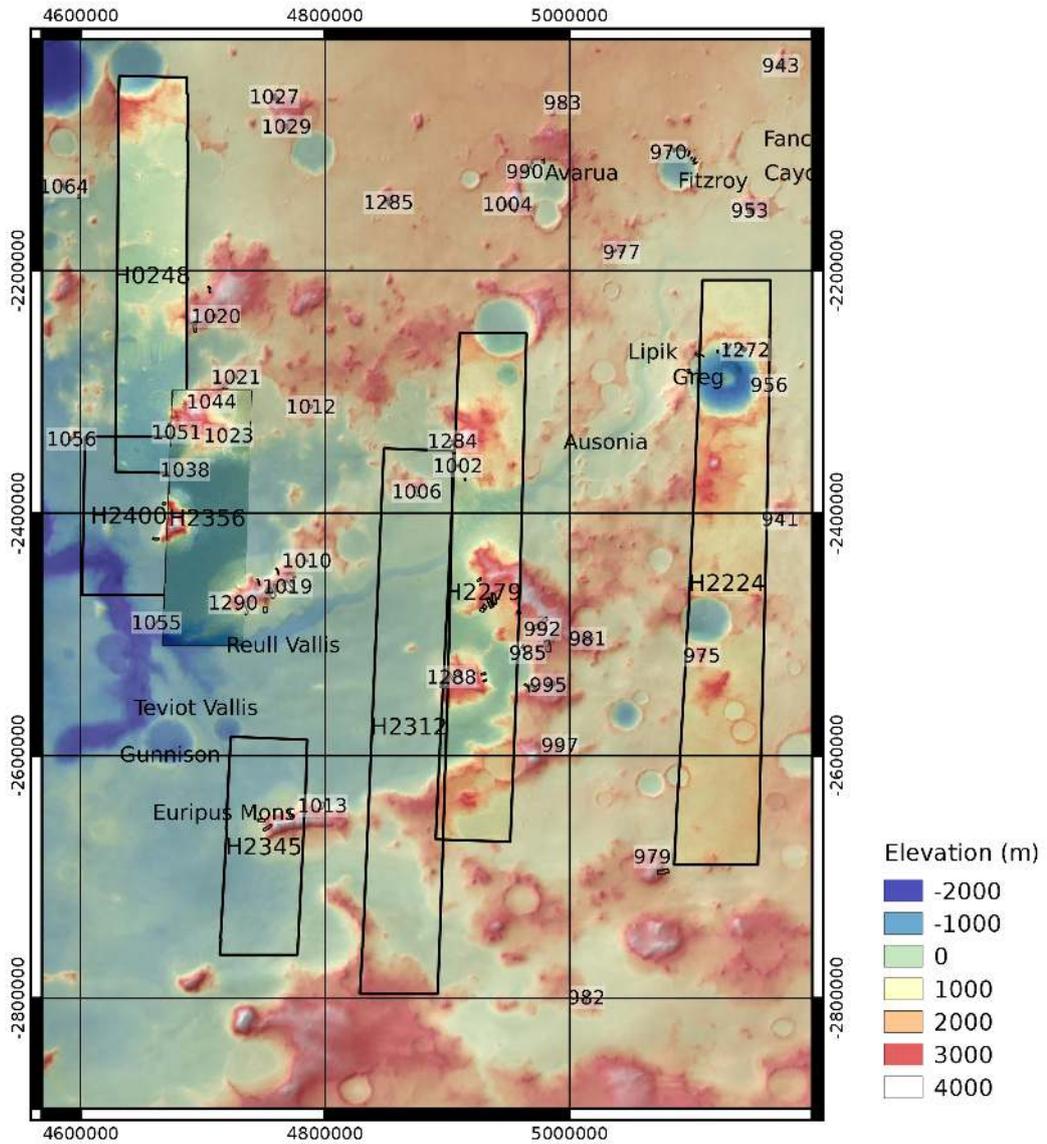
Figure 4.6: HRSC DTM tiles at 50 and 75m resolution in the area east of Hellas Planitia, of which tiles h0248, h2279, h2224 and h2356 are displayed. The background is filled by MOLA elevation. The grid numbers are in units of metres, in an equicylindrical projected coordinate system with standard parallel at 40° latitude.
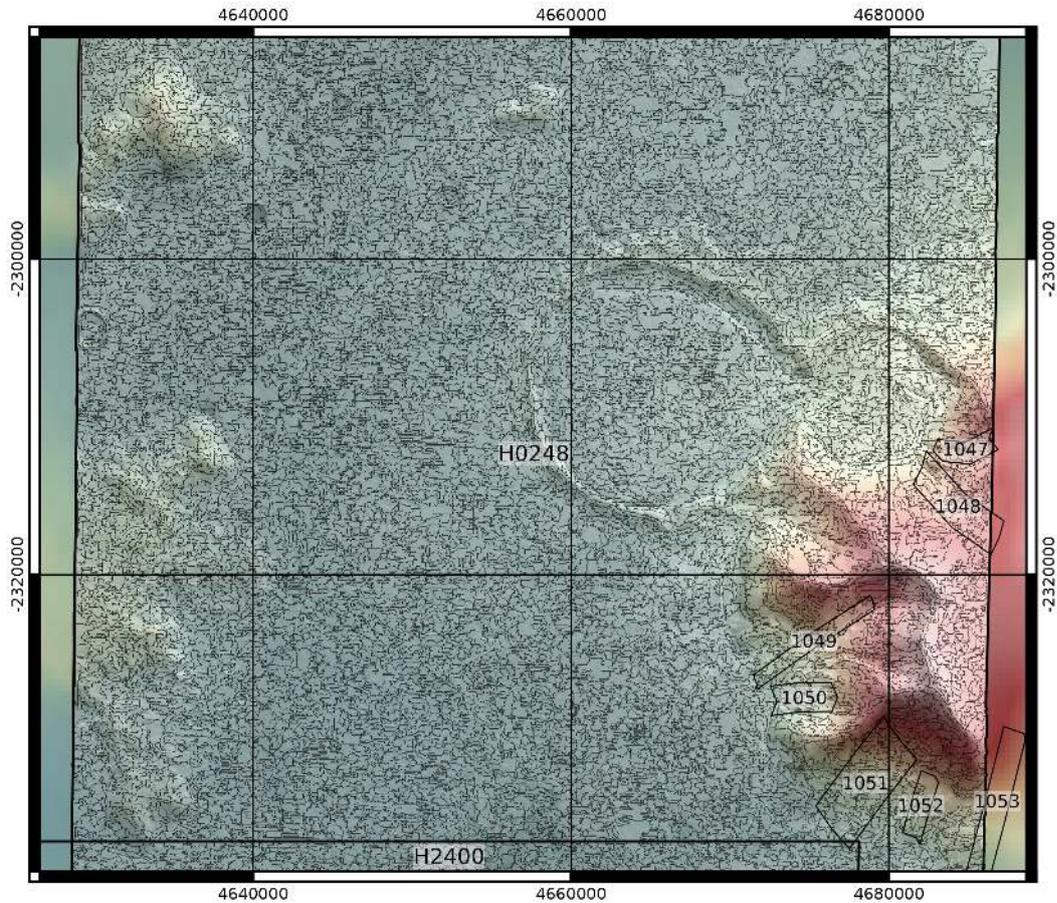
Figure 4.7: The RSGISLib segmentation of HRSC tile h0248, showing the southern portion of the tile. The total number of segments across the whole tile is 43909. Grid units are in metres as for figure 4.6

(a)   (b)
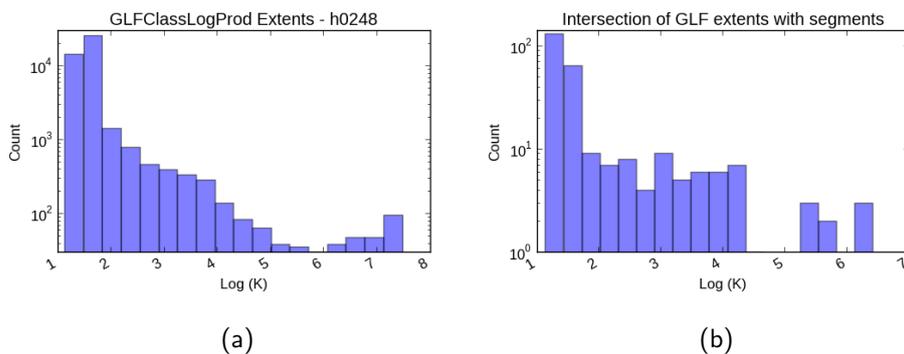
Figure 4.8: Histogram of $\log_e(K_e)$ for tile h0248 calculated based on GLF extents. The mean and standard deviation of $\log_e(K_e)$ are 1.65 and 0.61 respectively. The number of segments intersecting is 263 and the mean and standard deviation of these are 1.86 and 1.08. The Z statistic has a value of 5.58.

54

indicates a highly significant rejection of the null hypothesis that the classifier function has the same distribution for the GLF areas as the tile as a whole.

This can also be calculated for the classifier function based on the average feature variables of the 100m radius head buffers, as in figure 4.9. In this case, $Z = 16.6$, substantially higher than when calculating the classifier using the extent averages. For this reason, the 'head' version of the classifier function is used in the rest of this work.

(a)	(b)
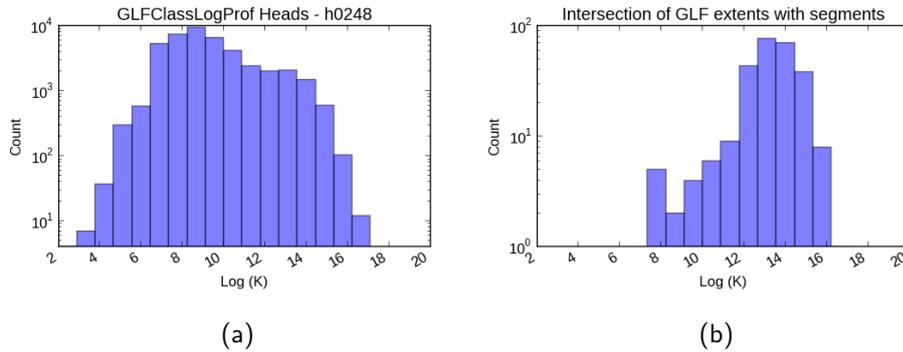
Figure 4.9: Histogram of $\log_e(K_h)$ for h0248 calculated based on the 100m buffer around the heads. The mean and standard deviation are 8.62 and 4.52 respectively. The number of segments intersecting is 263 and the mean and standard deviation of these are 13.24 and 1.46. The Z statistic has a value of 16.6.

Tile h2279

This tile is located at 38-45°S, and 108°E. There are 12 Souness catalogued GLFs within the tile. See figures 4.12 and 4.13 for the results in this tile.

4.2.2 Mareotis Fossae: Tiles h5304 and h5286

In the northern hemisphere, the tiles h5304 and h5286 near Mareotis Fossae region at $\sim 80°$W have 50m HRSC topographic data, and are discussed below. These tiles are located at 40-50°N and 83-86°W. There are 8 Souness GLFs within h5304, and 11 within h5286.[2] A location map to show the general location of these tiles is shown in figure A.2. See figures 4.14 and 4.15 for results of these tiles.

---

[2]One object, Souness catalogue number 50, is covered in both tiles.
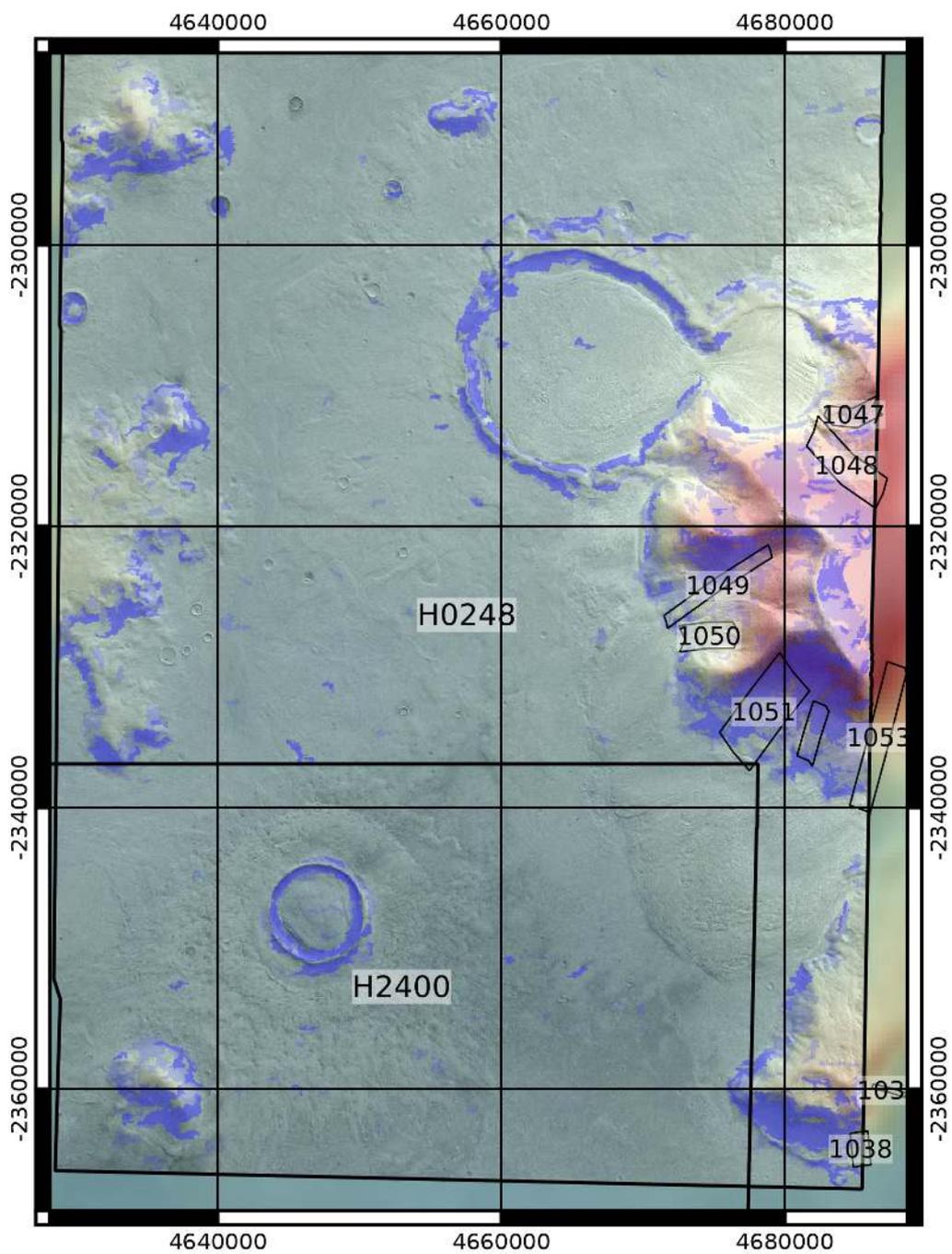
Figure 4.10: Part of HRSC tile h0248, showing segments where $\log_e(K_h) > 13$, and $\log_e(K_h) > 14$ in progressively darker shades of blue to classify potential glacier source areas.
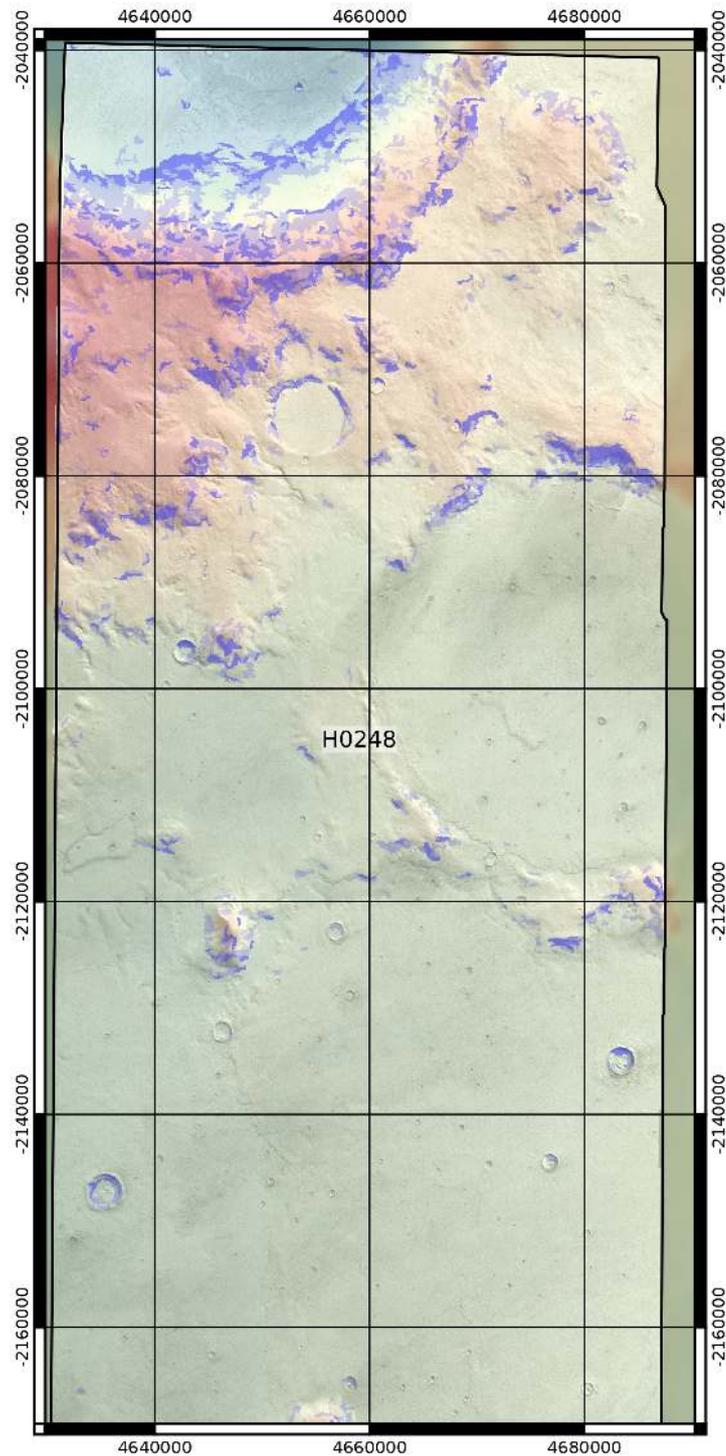
Figure 4.11: Part of HRSC tile h0248, showing segments where $\log_e(K_h) > 13$, and $\log_e(K_h) > 14$ in progressively darker shades of blue, searching for glacier source areas. In this case, there have been areas picked up by the classifier function that do not have Souness GLFs.

GLFClassLogProd Heads - h2279

Intersection of GLF extents with segments

(a)   (b)
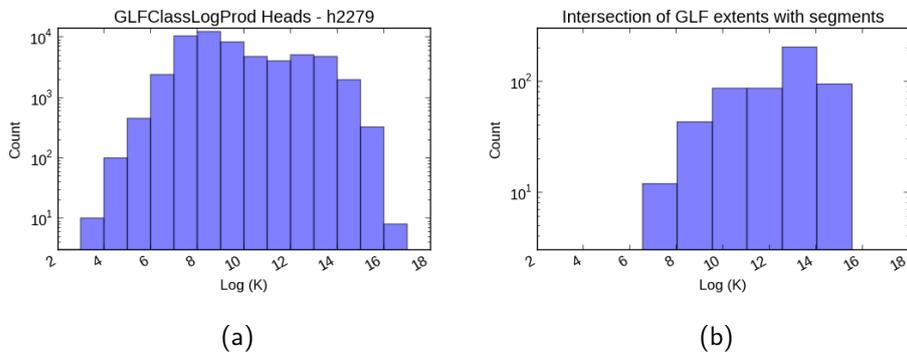
Figure 4.12: Histogram of $\log_e(K_h)$ for tile h2279 calculated based on the 100m buffer around the heads. The mean and standard deviation of $\log_e(K_h)$ are 9.37 and 3.78 respectively. The number of segments intersecting is 531 and the mean and standard deviation of $\log_e(K_h)$ for these are 12.08 and 2.94.

The null hypothesis of the intersected segments being the same distribution as the overall tile is rejected at $Z = 16.5$.
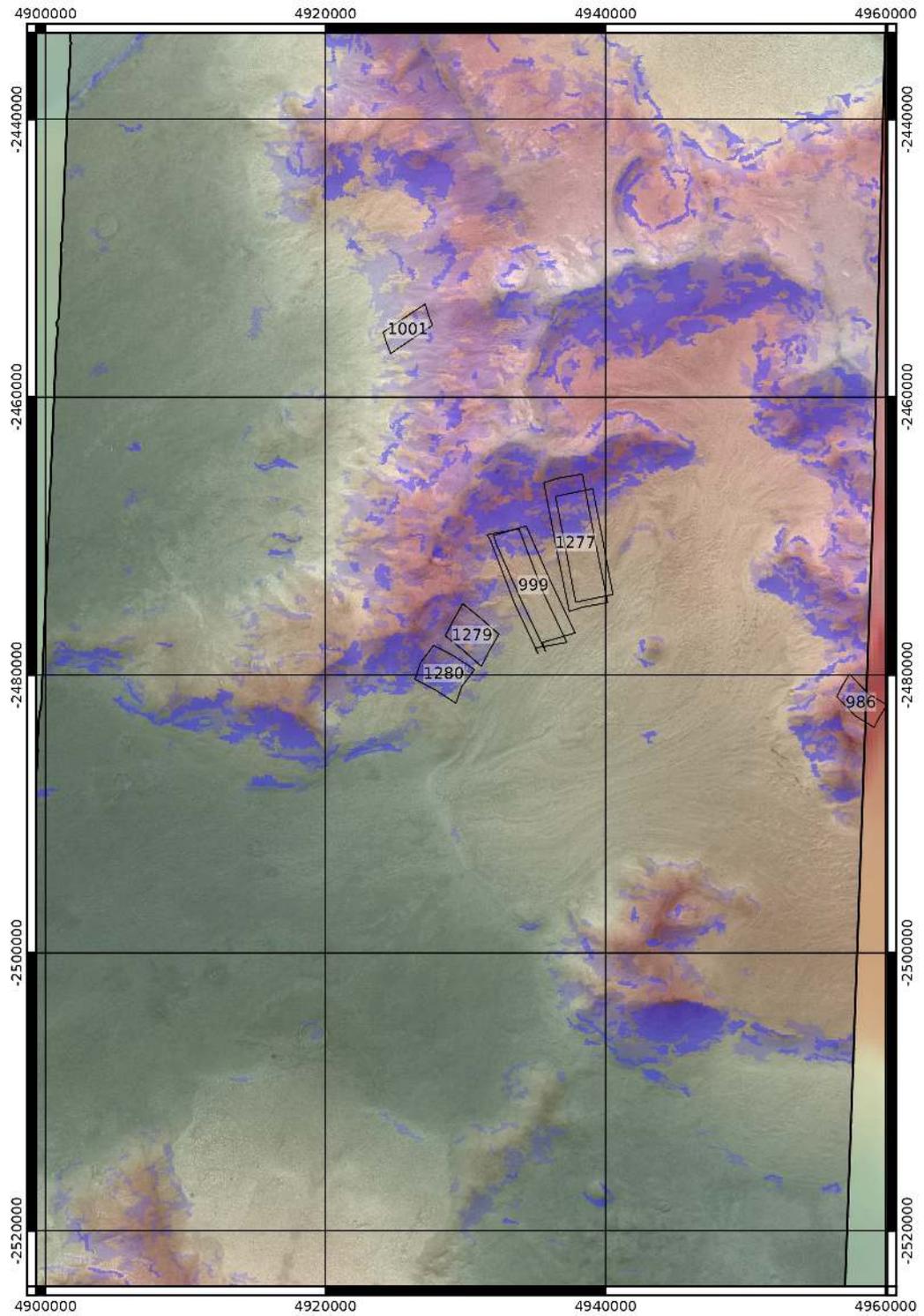
Figure 4.13: Part of HRSC tile h2279, showing segments where $\log_e(K_h) > 13$, and $\log_e(K_h) > 14$ in progressively darker shades of blue to classify potential glacier source areas.

(a)

(b)

(c)

(d)
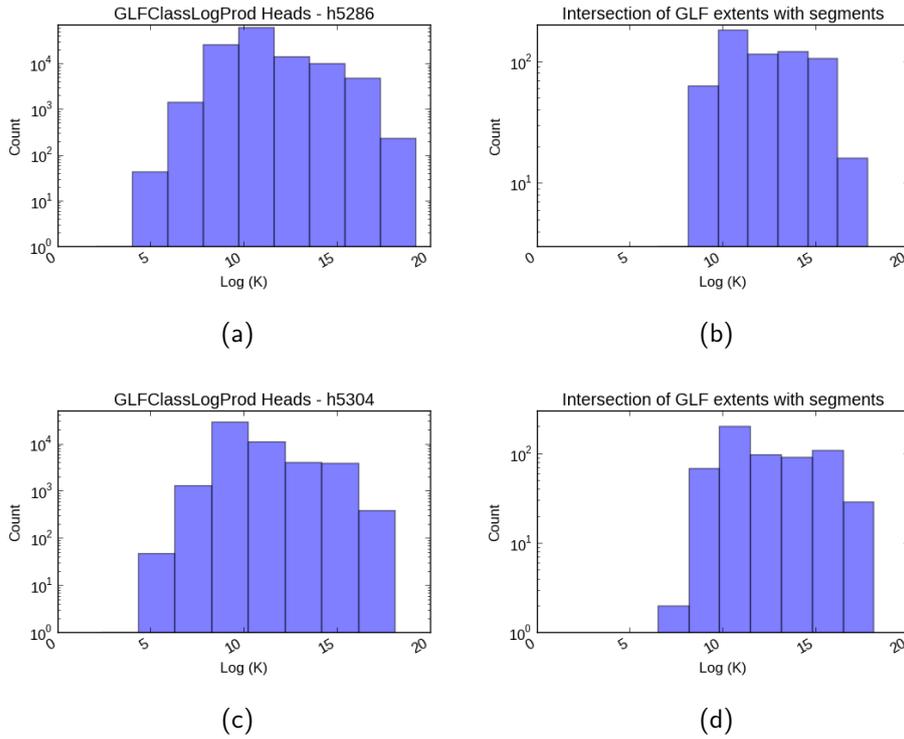
Figure 4.14: Histograms of $\log_e(K_h)$ for tiles h5286 and h5304 calculated based on the 100m buffer around the heads.

For h5286, the mean and standard deviation of $\log_e(K_h)$ are 10.35 and 4.12 respectively. The number of segments intersecting is 616 and the mean and standard deviation of $\log_e(K_h)$ for these are 12.00 and 3.43. The null hypothesis of the intersected segments being the same distribution as the overall tile is rejected at $Z = 9.94$.

For h5304, the mean and standard deviation of $\log_e(K_h)$ are 10.08 and 3.88 respectively. The number of segments intersecting is 608 and the mean and standard deviation of $\log_e(K_h)$ for these are 12.05 and 3.79. The null hypothesis of the intersected segments being the same distribution as the overall tile is rejected at $Z = 12.5$.
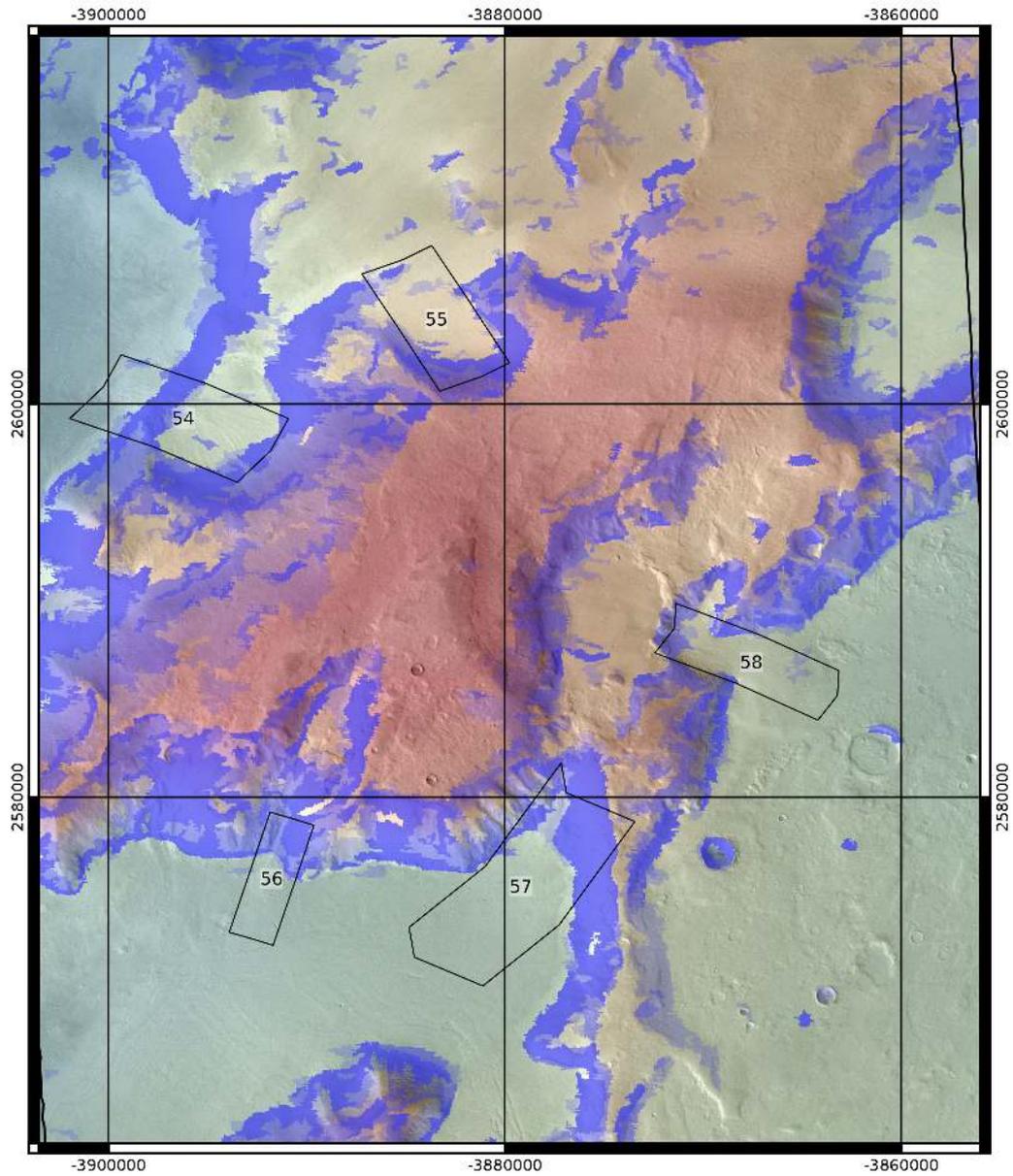
Figure 4.15: Part of HRSC tile h5304, showing segments where $\log_e(K_h) >$ 13, 14, and 15 in progressively darker shades of blue to classify potential glacier source areas.

4.2.3 Olympus Mons: Tile h0037

The HRSC tile h0037 is one of the largest in the data used in this work, with pixel dimensions of 4391 × 36200. This tile at 14-44°N, ∼ 132°W includes 7 Souness GLFs in the Acheron Fossae region, and also the summit of Olympus Mons, and also includes part of the lobate debris apron north of the Olympus Mons escarpment. See figure A.1 for a general location map, and figures 4.16, 4.17 and 4.18 for results of this tile.

(a)   (b)
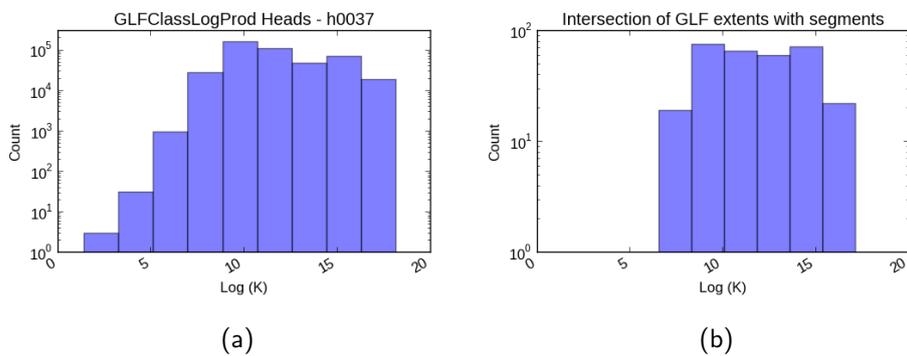
Figure 4.16: Histogram of $\log_e(K_h)$ for tile h0037 calculated based on the 100m buffer around the heads. The mean and standard deviation of $\log_e(K_h)$ are 10.65 and 5.44 respectively. The number of segments intersecting is 608 and the mean and standard deviation of $\log_e(K_h)$ for these are 11.53 and 3.55.
The null hypothesis of the intersected segments being the same distribution as the overall tile is rejected at $Z = 2.88$. Note that part of the lobate debris apron north of Olympus Mons is in this tile, much of which has a high $\log_e(K_h)$.
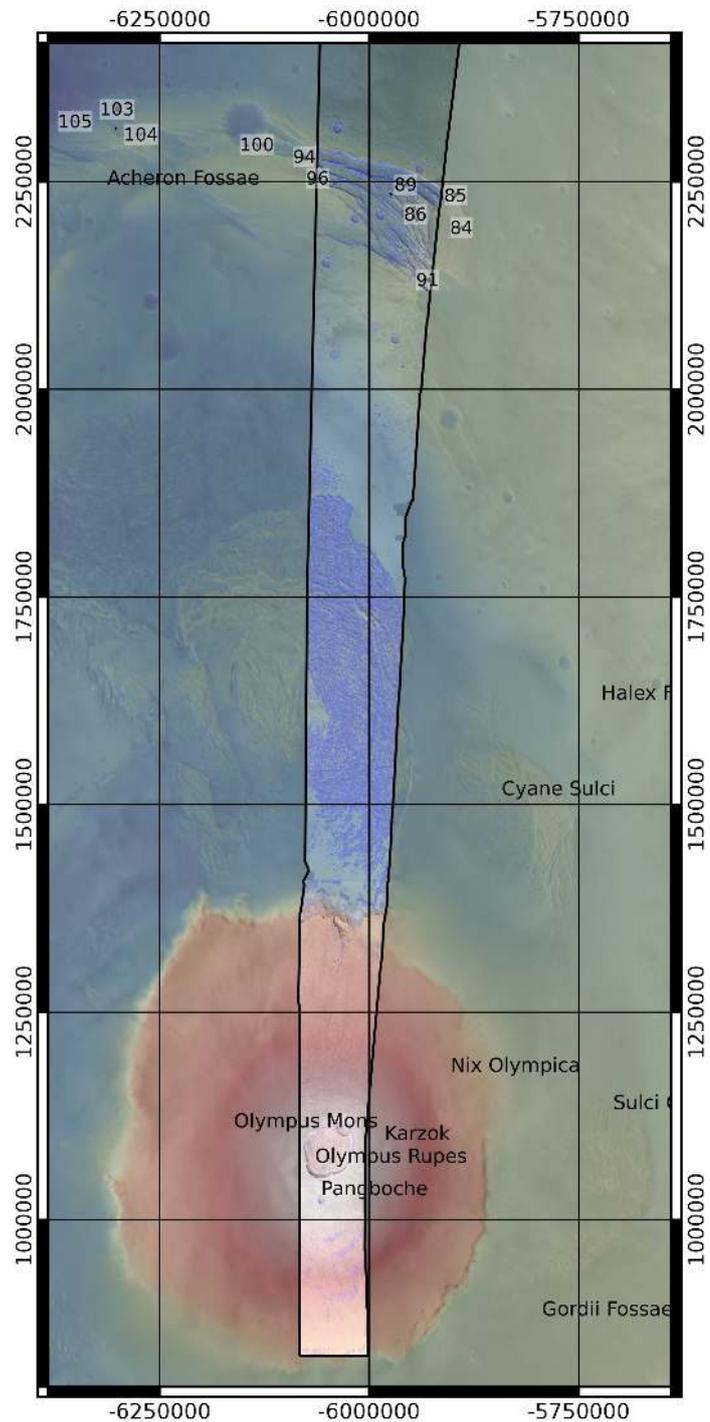
Figure 4.17: HRSC tile h0037, showing segments where $\log_e(K_h) >$ 13, 14, 15, 16 and 17 in progressively darker shades of blue to classify potential glacier source areas. The Olympus Mons lobate debris apron can be noted, and is visible highlighted in blue here.
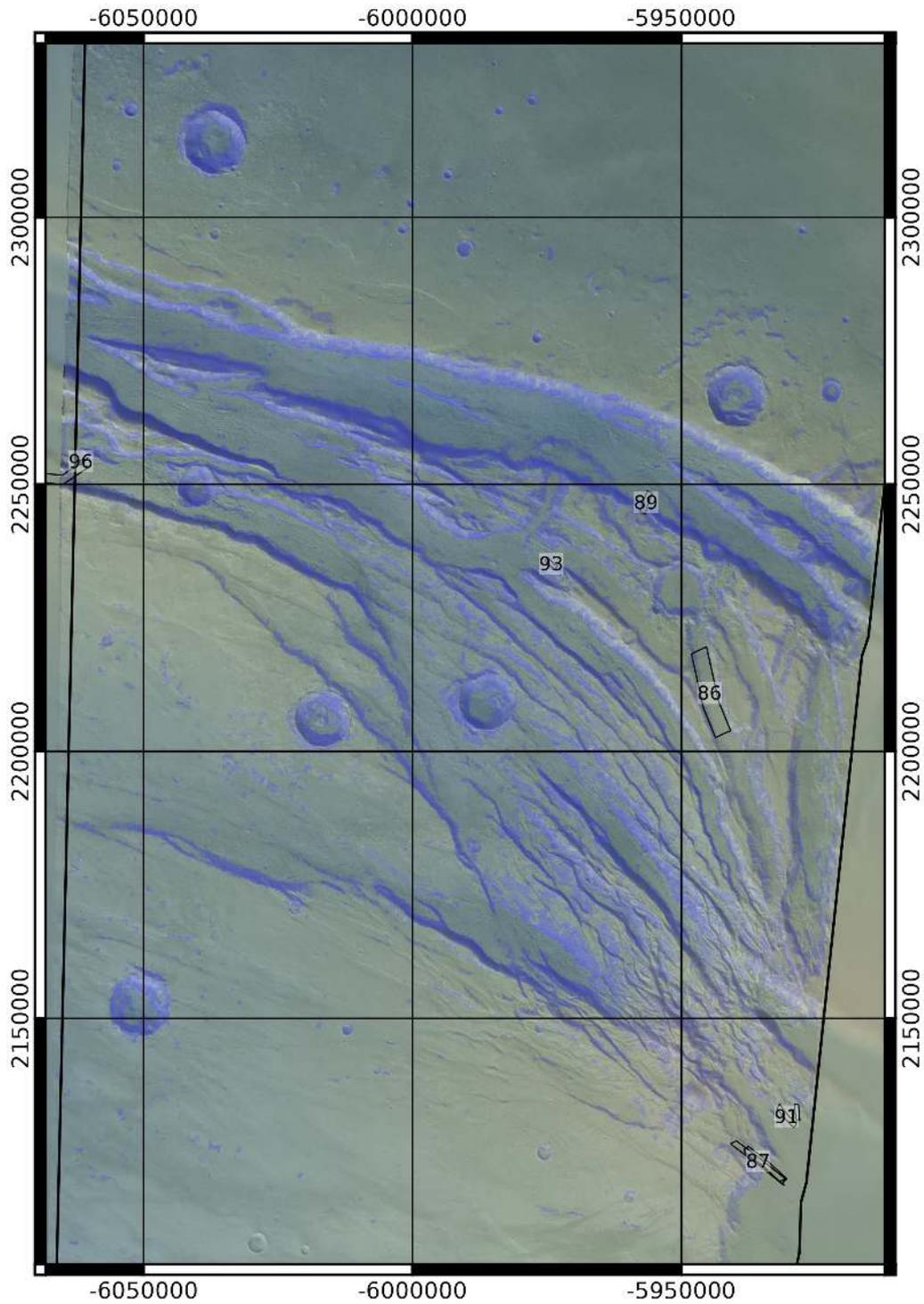
Figure 4.18: Part of HRSC tile h0037, showing the Acheron Fossae area. Segments where $\log_e(K_h) > 13, 14, 15, 16$ and 17 are shaded in progressively darker shades of blue to classify potential glacier source areas.

4.2.4   East of Hellas: Tiles with 75m resolution DTM data

The tile h2224 which covers the area around the well-studied crater Greg with its GLFs, of which there are 14 catalogued objects[3], and h2356 are presented below. Tile h2356 has 19 Souness GLFs within its footprint, and several others partially within it. Tile h2224 is at 113°E, 38-45°S and h2356 is at 104°E, 39-42°S. See figures 4.6 and A.11 for location, and figures 4.19, 4.20, and 4.21 for results.
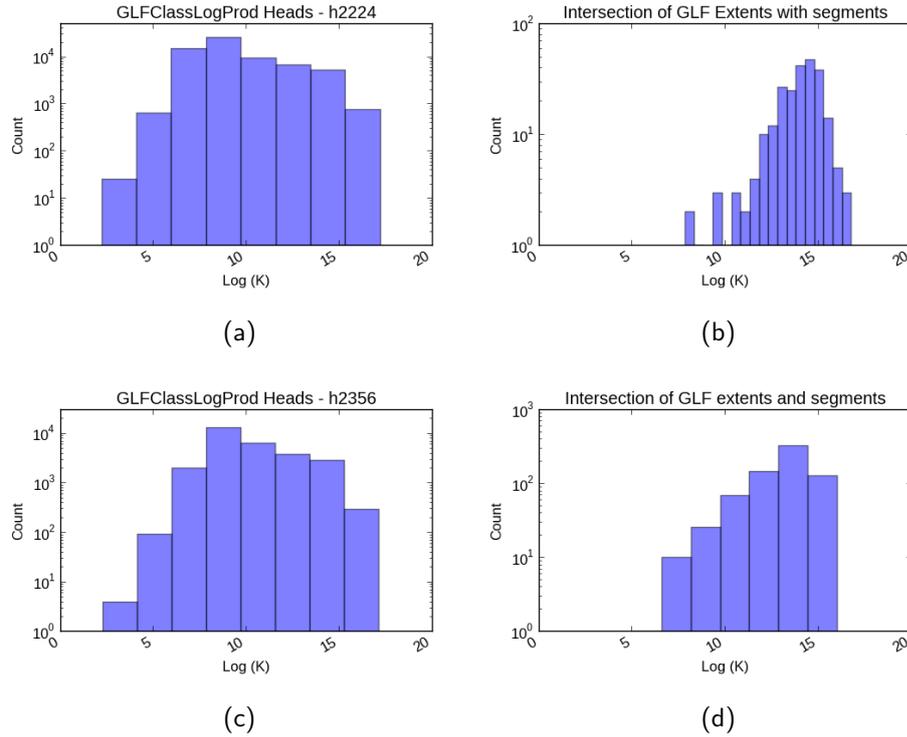
Figure 4.19: Histograms of $\log_e(K_h)$ for tiles h2224 and h2356 calculated based on the 100m buffer around the heads.

For h2224, the mean and standard deviation of $\log_e(K_h)$ are 9.21 and 3.61 respectively. The number of segments intersecting is 239 and the mean and standard deviation of $\log_e(K_h)$ for these are 13.89 and 1.39. The null hypothesis of the intersected segments being the same distribution as the overall tile is rejected at $Z = 20.0$.

For h2356, the mean and standard deviation of $\log_e(K_h)$ are 9.50 and 4.29 respectively. The number of segments intersecting is 716 and the mean and standard deviation of $\log_e(K_h)$ for these are 12.84 and 2.68. The null hypothesis of the intersected segments being the same distribution as the overall tile is rejected at $Z = 20.8$.

---

[3]Two of these, 950/1271, and 951/1272 appear to be duplicates of each other, and there are a further two GLFs partially within the tile.
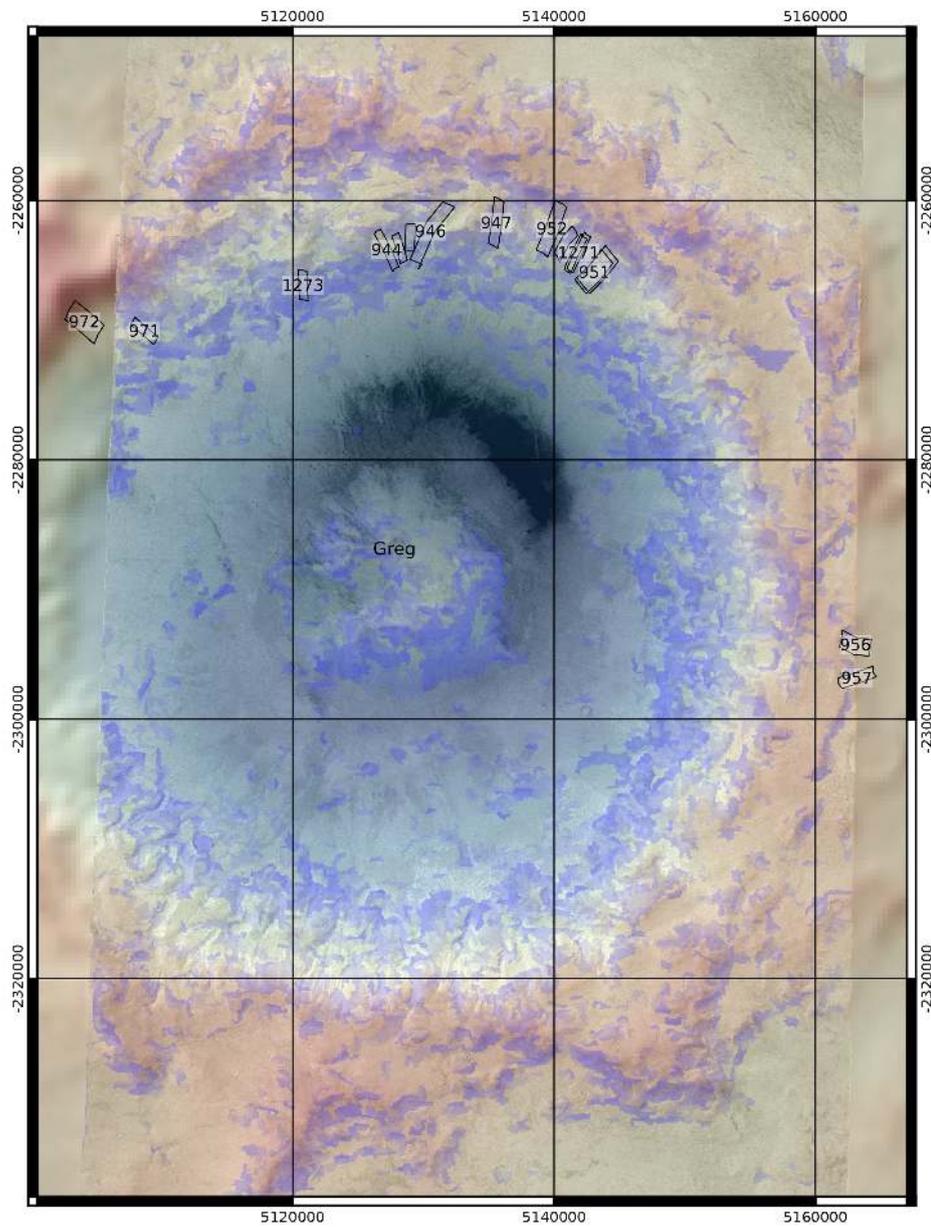
Figure 4.20: Part of HRSC tile h2224, showing crater Greg. Segments where $\log_e(K_h) > 13,\ 14,\ 15$ and 16 are shaded in progressively darker shades of blue to classify potential glacier source areas.
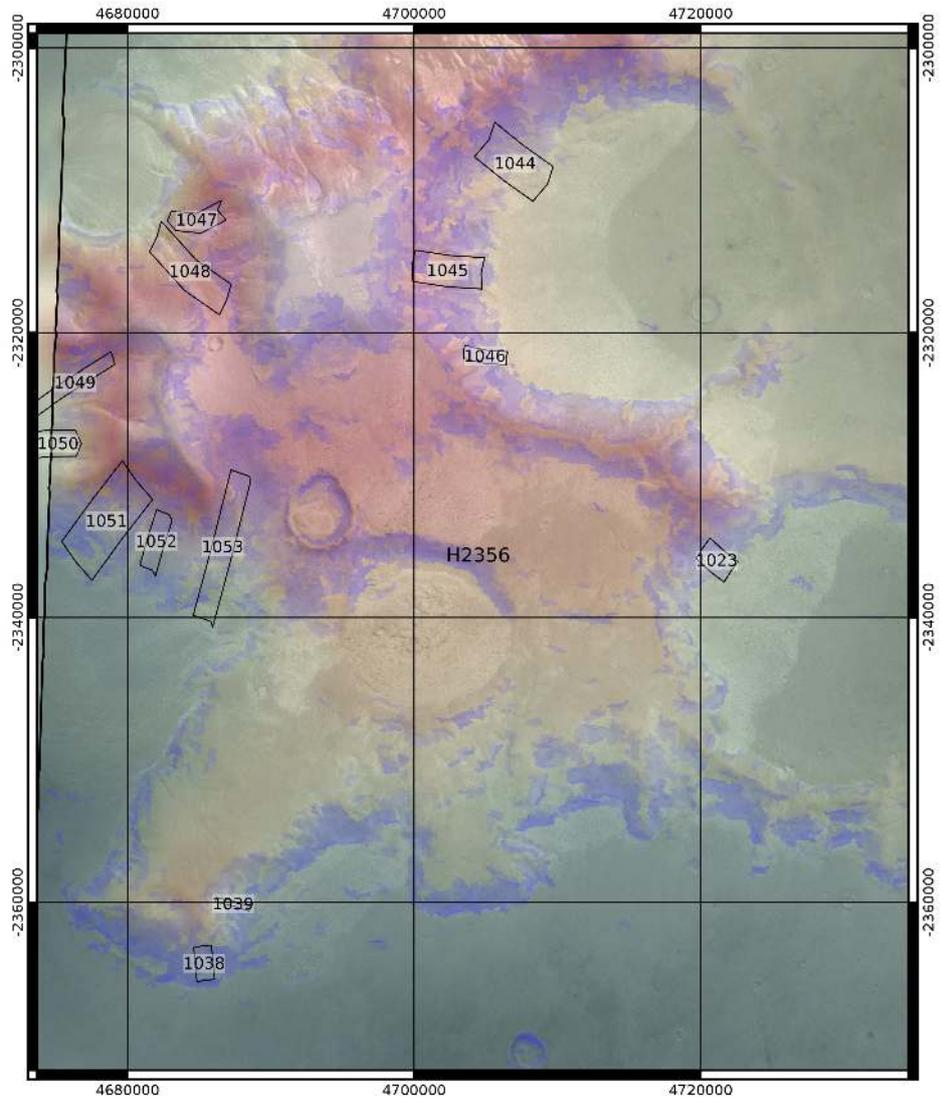
Figure 4.21: Part of HRSC tile h2356. Segments where $\log_e(K_h) > 13, 14, 15$ and 16 are shaded in progressively darker shades of blue to classify potential glacier source areas.

4.2.5   Protonilus Mensae: Tiles h1545 and h1523

The tiles h1545 and h1523 in the region of the northern hemisphere dichotomy at $\sim 45 - 50°$E around Protonilus Mensae have 75m topographic data and contain a large number of catalogued GLFs. Tile h1545 has 38 Souness GLFs and tile h1523 has 54. These tiles cover an area around 37-50°N and 45-51°E. See figure A.4 for overall location and figures 4.22, 4.23, 4.24 and 4.25 for results of these tiles.

(a)

(b)

(c)

(d)
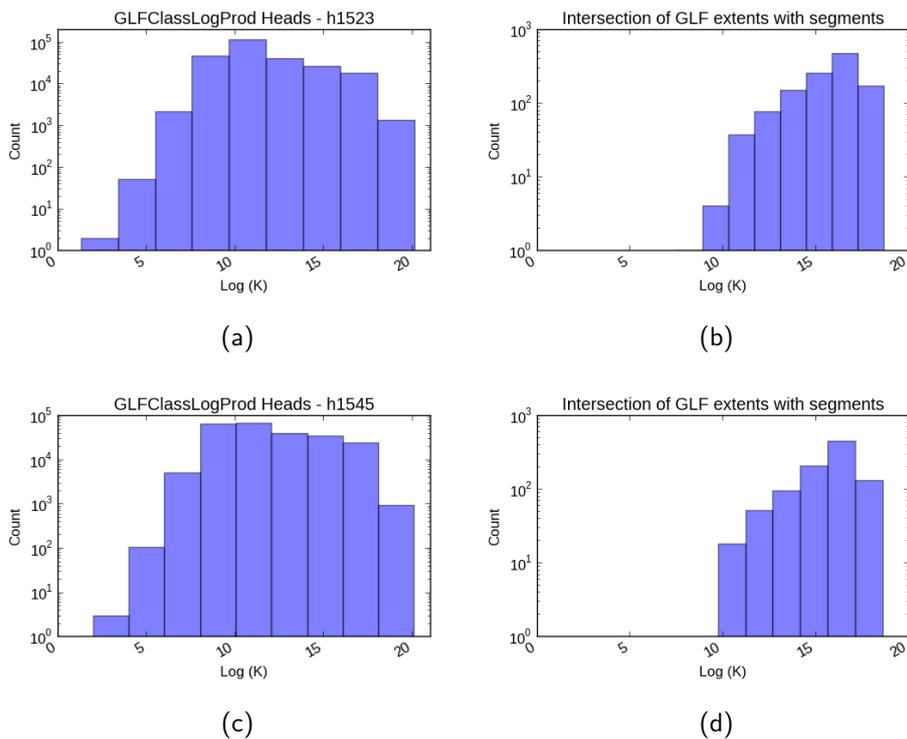
Figure 4.22: Histogram of $\log_e(K_h)$ for tiles h1523 and h1545 calculated based on the 100m buffer around the heads.

For 1523, the mean and standard deviation of $\log_e(K_h)$ are 11.06 and 4.14 respectively, and the number of segments intersecting is 1184 and the mean and standard deviation of $\log_e(K_h)$ for these are 15.52 and 2.36. The null hypothesis of the intersected segments being the same distribution as the overall tile is rejected at $Z = 37.1$.

For 1545, the mean and standard deviation of $\log_e(K_h)$ are 11.33 and 4.68 respectively, and the number of segments intersecting is 954 and the mean and standard deviation of $\log_e(K_h)$ for these are 15.48 and 2.33. The null hypothesis of the intersected segments being the same distribution as the overall tile is rejected at $Z = 27.4$.
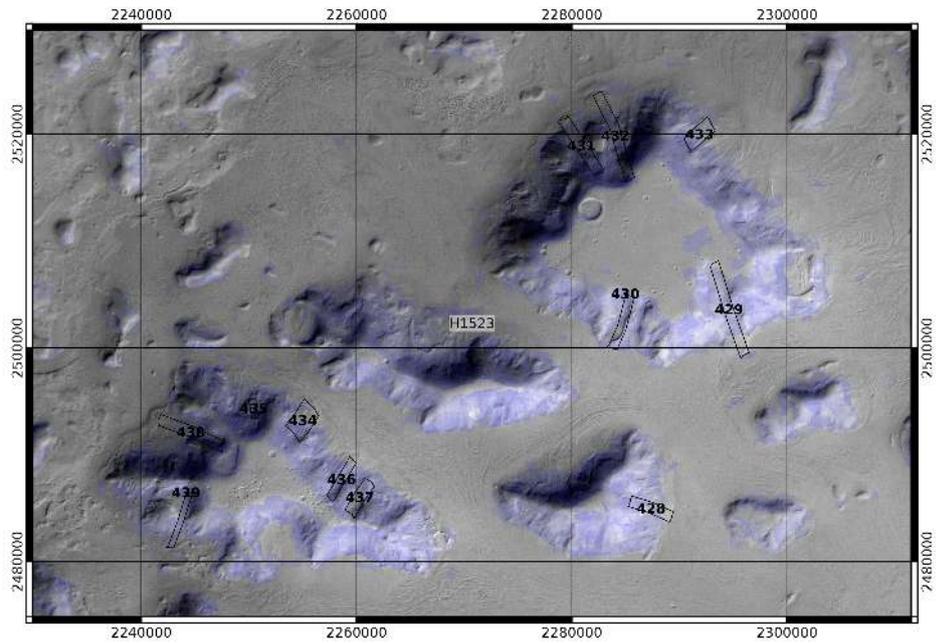
Figure 4.23: Part of HRSC tile h1523. Segments where $\log_e(K_h) > 15, 16, 17, 18$ and 19 are shaded in progressively darker shades of blue to classify potential glacier source areas.
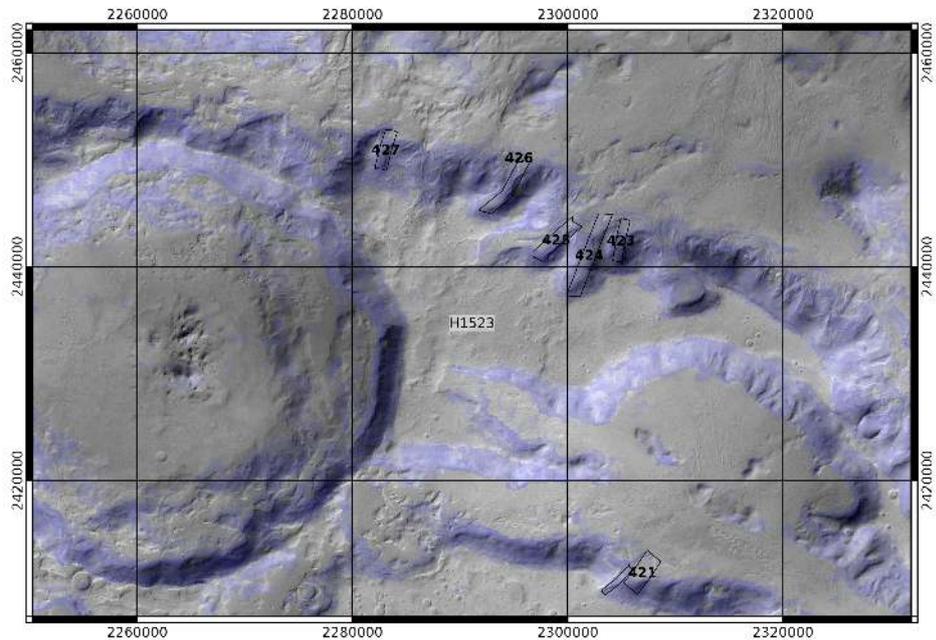
Figure 4.24: Part of HRSC tile h1523. Segments where $\log_e(K_h) > 15, 16, 17, 18$ and 19 are shaded in progressively darker shades of blue to classify potential glacier source areas.
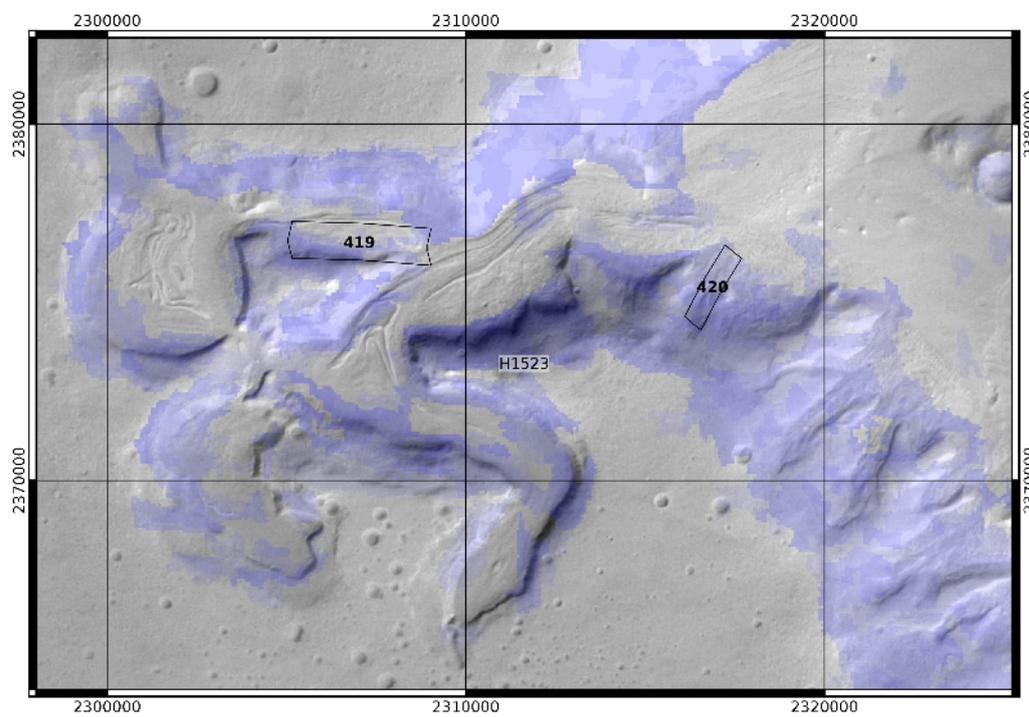
Figure 4.25: Part of HRSC tile h1523. Segments where $\log_e(K_h) >$ 15, 16, 17, 18 and 19 are shaded in progressively darker shades of blue to classify potential glacier source areas.

Chapter 5

Discussion

5.1 Implications of the descriptive statistics

5.1.1 Nadir image brightness

The nadir image brightness being brighter for the GLF extents than the average for the HRSC tiles may be due to the objects having a debris cover from the typical wind-blown dust on Mars, rather than the darker, volcanic rocks found in some locations. Alternatively, it may be that areas with darker dust cover are less likely to form persistent glaciers, due to a thin covering of low albedo dust accelerating sublimation, therefore regions where the dust covering is light in colour are more likely to preserve glaciers. The ratio of the nadir brightness areas of interest to HRSC coverage is stronger for the 100m head buffers, than the extent buffers, indicating that as one concentrates on the source areas, the effect becomes stronger, or that since the head areas are by their definition as the head of a gravitationally driven flow feature, locally elevated in topography, they are less likely to be in shadow.

5.1.2 Elevation

The depletion of the numbers of GLFs at z < -3000m may be due to one of two reasons: either they were not formed below this elevation, or they were perhaps formed, but have not been preserved to the present day. Differential sublimation, due to variation in debris cover may have occured, perhaps due to wind stripping off dust-sized particles of debris cover, allowing sublimation to take place. At very low elevations, it is possible that the thicker atmosphere is more likely to

promote sublimation, perhaps due to higher temperatures. Nevertheless there are a number of GLFs in the Souness catalogue at very low elevations, of $z < -5000$m (see figures 4.1d and 4.3b). Most of these are concentrated in Hellas Planitia, in tiles such as h0365 in the Harmakhis Vallis area. It is possible that these objects are a population that formed at a later time than the main body of the Souness catalogued GLFs. In this model, at the earlier time, the relatively high obliquity made the elevation range -3000m to 0m most optimal for glacier growth and preservation, with conditions below -3000m favouring ablation by sublimation or melting. Later, the obliquity declined, preserving this population where sufficient debris cover existed to prevent sublimation. However at some later epoch, a climate existed within the Hellas Planitia area where the optimal accumulation zones were the low elevations below -5000m. This would require that the climate has not been warm enough for melting to take place in the low elevation zone since the second epoch, therefore these objects should be younger than the main population, a prediction testable via small crater counts where HiRISE images exist. A portion of HiRISE image PSP_006224_1385 is shown in figure 5.1 covering two Souness catalogued objects at 41.0°S, 90.15°E. It appears that these objects have experienced either some downwasting by ablation, or downslope flow after accumulation ceased, since they appear to have retreated from the heads of their potential accumulation areas.

It would be an interesting study to estimate an age for the surfaces of low-elevation glaciers, to test whether they are younger than the ~ 0.4Myr postulated youngest age for the glaciers in Greg Crater. Another possibility is that the widespread light-coloured dust in Hellas allowed glaciers to form at low elevations since their ablation was reduced by the high albedo of their debris cover. Souness *et al.* (2012) did not catalogue any GLFs within Lyot crater, the lowest point of elevation in the northern hemisphere at ~ 50°N, 30°E and an elevation of the crater floor of $z \sim -7000$m. Mars experiences a shifting of the perihelion summer between the southern and northern hemispheres due to the change in longitude of perihelion, so it is possible that the timing of the last epoch of suitable climate for glacier accumulation was different in the southern hemisphere to the north. There are a small number of GLFs catalogued in craters in the northern plains at elevations $z \sim -5000$m, so it would appear the northern hemisphere formed low-elevation glaciers as well. The absence of catalogued GLFs in Lyot may have been an effect of the higher latitude of the low elevation area of Lyot crater com-
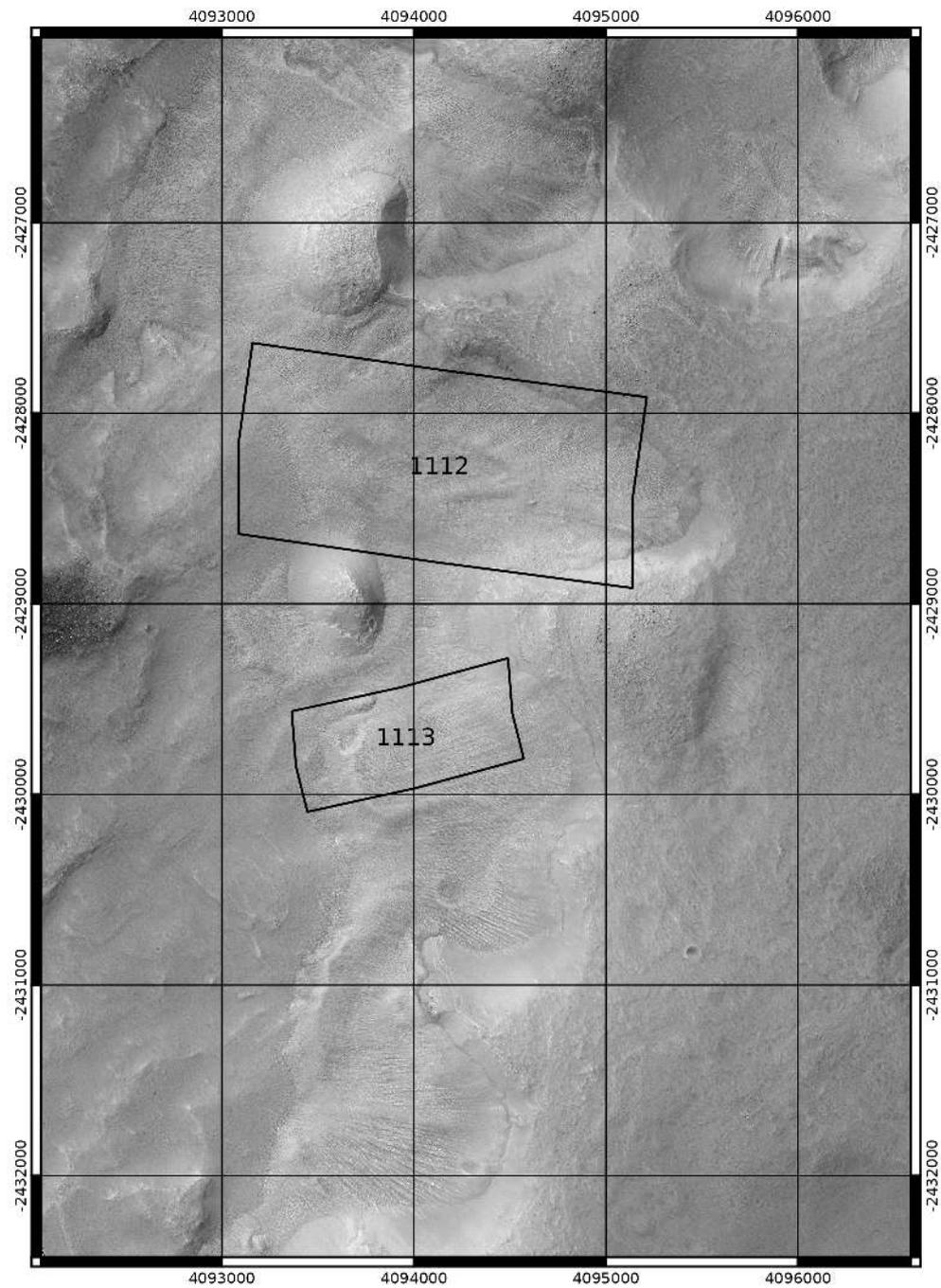
Figure 5.1: A portion of the HiRISE image PSP_006224_1385 showing the Souness catalogued objects 1112 and 1113 at 41.0°S, 90.15°E. These are at average elevations of -5051m and -5108m. North is up.

pared to Hellas, which may have meant the climate was not suitable for sufficient accumulation of glacier ice by precipitation.

5.1.3 Slope

Souness *et al.* (2012) noted that areas with the most precipitous relief, measured in that work by the standard deviation of MOLA elevation within the 5km buffer of the head, have fewer GLFs than areas of moderate relief, indicating some 'optimum' level. Areas of low slope can be understood not to support viscous flow due to insufficient shear stress, and it is suggested that for high levels of relief, sublimation may be enhanced due to exposure of ice by debris landslides.

In this work, the ratio function for extents in figure 4.3c shows a peak between $10 - 15°$. The slope for the 100m buffers around the heads shows a broad distribution with greatest enhancement of GLF counts relative to overall topography between $15 - 20°$ and a drop-off above $20°$ indicating there is some factor that is suppressing them. A possible explanation is that more exposed head areas are more liable to experience wind promoted sublimation, or alternatively that the glaciers have flowed downslope from areas of steeper slope in the time since accumulation ceased.

5.1.4 Aspect

On Earth, the permanence of glaciers is largely controlled by the summer temperature, which determines whether melting takes place. The aspect of slopes exerts a control on the level of insolation on any particular terrain, and with the thin atmosphere on Mars compared to Earth, radiation on the surfaces of glaciers may be a more significant control on ablation relative to convective heat transfer. Under the high obliquity conditions in the past on Mars, these radiative conditions were different from the present day, and any Earth analogues.

On Mars at $60°$ obliquity, and at $40°$ latitude, on the summer solstice the altitude of the Sun would have been $70°$ above the horizon at noon in the poleward direction, and $10°$ at midnight. At $50°$ latitude $80°$ at noon, and $20°$ at midnight. At $60°$ it would have been directly overhead at noon, and $30°$. Thus it is poleward slopes that experience the greatest insolation under high obliquity.

It is possible that the GLFs stop occurring in the higher mid-latitudes due to sublimation/melting under the continuous polar daylight at the highest obliquities.
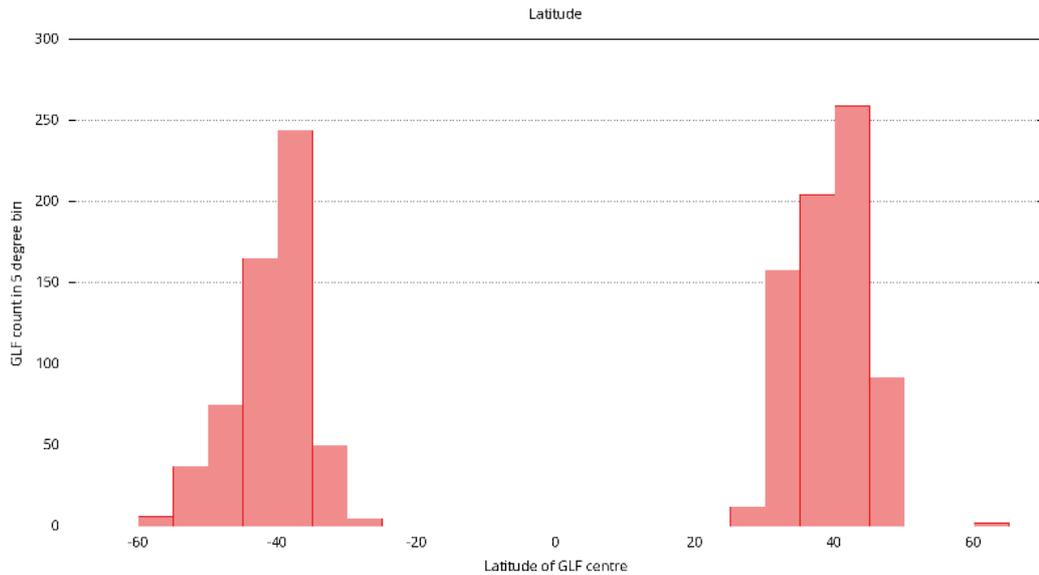
Figure 5.2: The distribution of the Souness GLF centre latitudes, including all 1309 objects. The southern hemisphere distribution continues to lower latitudes, however the flat, low topography in the northern hemisphere may be responsible for this rather than being a primary effect of latitude.

The alternative explanation is that the temperatures have not been high enough in the recent glacial periods on Mars, to allow significant precipitation and accumulation at these latitudes. In both hemispheres, the numbers of GLFs tends to drop off poleward of $\sim 45°$ latitude (figure 5.2). It can be presumed that the deficiency in the northern hemisphere is due to the flat, low topography in the 50s N on Mars. It is an open question whether this the drop-off in GLF counts at higher mid-latitudes is because there was too much insolation for preservation at the highest recent obliquities, when the higher latitudes would have experienced the most summer insolation, or whether it was not warm enough for accumulation in recent epochs at the higher latitudes.

The trends in GLF counts with respect to aspect in figures 4.2a and 4.2b, show a greater tendency for the distribution to be concentrated in the poleward direction in the southern hemisphere. The effect of aspect is complex to model, since at moderate obliquities, poleward slopes could be a cold-trap, allowing preservation of glaciers, but this is not the case at very high obliquity where these receive more insolation as noted above, Lissauer, Barnes & Chambers (2012) mentioning that at more than obliquity $\phi = 54°$, the polar regions receive more annual-averaged insolation that the equator.

Kreslavsky, Head & Marchant (2008) consider active-layer permafrost processes, suggesting that these occur when summer day-average temperatures exceed $0°C$ and suggest that this will occur at high obliquity for polar regions, and on mid-latitude poleward facing slopes. An asymmetry of slopes has been noted, with poleward slopes having a tendency to be less steep. Conway & Mangold (2013) consider this the product of deposition on poleward facing slopes. At high obliquity, there would be a higher day-average temperatures during summer on pole-facing slopes, but lower annual average. Arfstrom & Hartmann (2005) suggest that as obliquity decreases, pole-facing slopes would preserve ice for longer against ablation.

5.1.5 Curvature layers

The position of glacier slopes with respect to wind may have been significant on Mars. It is only possible to simulate what conditions existed during the higher obliquity periods in which the Martian glaciers are believed to have accumulated, however in the Antarctic Dry Valleys, wind-blown redeposited snow is a key factor determining the locations of glacier accumulation as was found in Chinn (1980). Redeposited snow accumulating in valley heads and against steep slopes was the source of the majority of the Dry Valleys alpine glaciers. Ablation by sublimation is also dependent on wind, where it was found that convex slopes exposed to the wind experience larger losses. (Kowalewski *et al.*, 2006).

The bias towards negative values of these curvature layers may be partly explained by the criteria used in Souness *et al.* (2012), which explicitly searched for flow features constrained by topography, however if the same factors of exposure to wind that affect deposition and sublimation in Antarctic Dry Valley glaciers have been relevant on Mars, this would be a physical reason for the observation.

5.2 Comments on the classifier function maps

It may be observed in the maps of the high values of the classifier function $\log_e(K_h)$ for head areas of glaciers, that many of the Souness GLF head areas are given a high value of the function and are thus shaded blue in the figures. However, it is not only these areas in the images that are shaded, but other areas not classified as GLFs by Souness *et al.* (2012). In figures 4.10 and 4.21, it can be seen that there are some other areas that appear to be flow features such as crater-fill

features and lineated valley-fill features (figure 4.23). Whether a feature of the type classified in Souness *et al.* (2012) forms depends not only on suitability of terrain for accumulation, but also on contextual topography.

In figure 4.20 of crater Greg, as well as picking out the head areas of the observed GLFs, areas below the currently observed GLFs are picked out as source areas, as well as areas on the south wall, and around the central mound. There is a hypothesis of an earlier epoch of glaciation in crater Greg than that which produced the presently observed GLFs in the north wall, in research by Fassett *et al.* (2010). This raises the possibility that a classifier such as this could potentially assist in searching areas of possible past glaciation where the glaciers have now disappeared through ablation.

5.3   Comparison to terrestrial glaciers

Mayo (1984) studied mass balance as a function of altitude, surveying the literature for glaciers in the USA, and found that both temperate and polar glaciers[1] had a more negative mass balance as altitude decreased. The exception was the Columbia glacier in Alaska, where at high altitudes, the positive mass balance turns over and begins to decrease due to the reduction in precipitation at the highest altitudes (between 2500m and 3500m) as the precipitable water vapour is precipitated out of the atmosphere before the humid air masses reach this elevation. This could have important implications for Mars, where higher areas could be too dry for significant accumulation, potentially reversing the common terrestrial pattern, leading to bare ground on higher areas, and glaciated lowlands. Fastook *et al.* (2008) detailed that ablation would be expected to decline with altitude slower than accumulation on Mars, leading to negative mass balance at the highest elevations, though this was discussing the high elevations on Tharsis rather than those within the range of the Souness mid-latitude GLFs.

Fountain *et al.* (2010) studied snow accumulation in the McMurdo Dry Valleys of Antarctica, where precipitated water equivalent can be $\sim$ 3-50mm per year, finding that wind-borne redeposition of snow enhanced the accumulation in certain areas. Differential sublimation can also be enhanced by exposure to wind, as Bliss, Cuffey & Kavanaugh (2011) found to be the case in Windy Gully within Taylor

---

[1]The technical distinction is that for temperate glaciers, accumulation occurs in a higher-altitude zone than ablation, whereas for an polar glacier, accumulation occurs throughout the glacier's area

Valley.

Wagnon *et al.* (1999) studied a glacier in the high Andes in Bolivia, where energy flux was dominated by radiation, and sublimation was the primary means of ablation, in the dry season, whereas melting took place in the wet season. The high sun angle of a tropical glacier means that radiation is often important in ablation. 'Penitentes' form under these conditions, whereby a hollow is progressively deepened by radiation being focused into it, but exposed points only receive direct rays, as described in Corripio & Purves (2005). The mid-latitudes of Mars at high obliquity would also experience a high sun angle. A difference between Mars and Andean glaciers would be that at the high obliquities, there would be less of a daily temperature cycle, since unbroken daylight would exist during summer. The air on Mars, even in a hypothesised thicker atmosphere would have been much thinner, and drier than the Earth. The conditions of Mars under a high obliquity would not have shared all of the characteristics of a single terrestrial analogue. The arid regions of the Andes may be another fruitful analogy as well as Antarctica, due to the aridity-dominated conditions there.

The Antarctic Dry valley glaciers have flow rates of of order of magnitude 0.1 to 1m per year. The mean annual temperature in that region is about 250K, perhaps in mid-latitudes of Mars mean annual temperature currently is about 210K. Based on an exponential scaling dependent on temperature (see Benn & Evans (2010)), and the fact the Martian surface gravity at 40% of the Earth's leads to a proportionately lower stress for a given loading, flow rates of Martian mid-latitude glacial features would be ~ 1 mm yr^{-1} or less. In the last 0.4 Myr since the last supposed epoch of glacier formation, flow would be less than 400m, less than the average length scale of these objects. Thus what is observed are likely to be primarily relict features, with most of the observed flow having taken place in past higher-obliquity epochs, rather than flow taking place under current conditions.

Lucchitta (1984) observed that the linear debris flows in Protonilus and Deuteronilus Mensae extend a maximum of no more than 20km from the scarps. A model of accumulation on these scarps and flow from them, could possibly account for the length of the flow features if the new, superposed features, are forms created by the flow of relic ice from the last Martian glacial period ~ 0.4 Myr ago.

5.4 Wet-based glaciers on Mars?

Arfstrom & Hartmann (2005) argued that the moraine-like ridges bounding several mid-latitude Martian viscous flow features could have been formed by water-lubricated sediment squeezing from beneath the ice in a wet-based glaciation. Banks *et al.* (2008, 2009) argue for a past wet-based glaciation in the Argyre Planatia region, at some point in Martian history. According to Fassett *et al.* (2010) these features date back to the Hesperian era, and are contemporary with glaciofluvial activity associated with the south circumpolar Dorsa Argentea formation, and interpreted to represent Hesperian drainage of meltwater discharge from a south circumpolar ice sheet, appearing to predate the Amazonian ice deposits discussed in Hubbard *et al.* (2011). Dickson, Fassett & Head (2009) examine Lyot crater, a crater believed to have formed in the early Amazonian at ($50°$N, $30°$E) and hypothesise conditions that allowed temporary liquid water, in an area of Martian atmospheric pressure and temperature being above the triple point of water, in what is the lowest point in the Northern hemisphere of Mars at a floor elevation of z ~ -7000m.

Antarctic permafrost in the Dry Valleys, has been observed to be strongly saline in some cases, (Dickinson & Rosen, 2003), (Hubbard *et al.*, 2004). If this is the case on Mars, then wet-based glaciers may be possible at much lower temperatures than would otherwise be the case.

5.5 Review of theory and observation of subsurface ice on Mars

Bryson *et al.* (2008) conducted some experiments simulating Mars conditions in a vacuum chamber to examine the stability of subsurface water ice on Mars, based on simulating the Martian regolith with basaltic material, which was observed beneath the red lighter dust layer by Mars Exploration Rover Spirit. Based on these experiments, they concluded a 1m thick layer of ice below 2m of the basalt soil could have survived since the obliquity change at the end of the last hypothesised Martian ice age 0.4 Myr ago. The survival time is sensitive to the depth of burial, at 1m underground the 1m ice layer is calculated to survive $\sim$ 1300 years.

Schon, Head & Milliken (2009) detailed two different hypotheses concerning the emplacement and distribution of ice in the near subsurface of Mars at mid-

high latitudes. These were either the diffusion of atmospheric water vapour into a porous regolith, forming ice-cemented soils (Mellon & Jakosky, 1995), or atmospheric deposition of ice, snow and dust by precipitation producing dusty ice-rich layers in periods of high obliquity. An enhanced mobilisation of atmospheric dust, would have provided condensation nuclei to promote precipitation. They favour the second hypothesis given the meters-thick layered deposits exposed at mid-latitudes.

In the first model, i.e. vapour diffusion, ice accumulation would be limited to available pore spaces of the regolith. A uniformly stratified, multi-layered deposit would not be expected, since deposition would be constrained by local topography and geology. A deposit draping the surface uniformly, exhibiting a distribution independent of local topography and geology, would be more likely to be the result of deposition by precipitation. A layered deposit may form during a lower-obliquity epoch resulting in sublimation, and concentration of the dust/debris layer, producing interbedded ice and sediment-rich sublimation lags. Gamma-ray and neutron spectroscopy show high latitude near-surface ice contents significantly above reasonable pore space estimates. (Boynton *et al.*, 2002; Feldman *et al.*, 2004)

The question to ask is this, whether the deposits were laid uniformly, and non-uniformly eroded, or only deposited in some places?

Kreslavsky & Head (2002a) detailed a meters-thick sedimentary layer at middle to high latitudes, covering about 23% of the Martian surface. There is a systematic variation of roughness by latitude at middle to high latitudes 30-50° north and south. At higher latitudes, terrains were shown to be smoother at short baselines, with a characteristic vertical scale of a few metres. This suggested the presence of a metres-thick mantling layer, originating through a sedimentation blanket. (Kreslavsky & Head, 2000; Mustard, Cooper & Rifkin, 2001). The mid-latitude mantle unit shows evidence of disaggregation and dissection events, followed by reaccumulation, resulting in a pitted or 'dissected' appearance visible in high-resolution HiRISE images. Mustard, Cooper & Rifkin (2001) interpret it as successive layers of ice-cemented dust, deposited during glacial phases, and ablated and disaggregated in interglacial phases. An alternative hypothesis would be chemical cementation of dust, however there was not any positive evidence seen for a chemical difference between 'mantle' terrain and terrain dominated by loose dust using thermal inertial or spectroscopic observations.

A slope asymmetry at mid-latitudes was observed by Kreslavsky, Head &

Marchant (2008). They found, based on analysis of global MOLA topography, that there was a latitudinal zonality of the occurrence of steep slopes. They found the frequency of steep ($> 20°$) slopes dropped more than three orders of magnitude from equatorial to high-latitude regions and that the boundary between extant steep slopes, and those that are reduced occurs at lower latitudes for pole-facing slopes and at higher latitudes for equator-facing slopes. There is thus a strong asymmetry between poleward and equatorward slopes in the mid-latitude zone around $45°$ latitude. They attribute this to an active permafrost layer forming in those areas which experience the highest day averaged surface temperatures at high obliquity. These are pole facing slopes at mid-latitudes, and all slopes at higher latitudes causing the relaxation of slopes preferentially in these areas. This hypothesis postulates that the active layer was active more than ~ 5 Myr ago, at the highest recent values of obliquity.

According to Kreslavsky & Head (2011), it has been possible for CO_2 glaciers to exist at high latitudes, during periods of low-obliquity. They observed features, which they refer to as 'high-latitude glaciers', including at $\sim 74°$N, $96°$E, where they observed looped ridges that appeared analogous to drop moraines of cold-based glaciers, which however appeared to exhibit too great a strain, and too plastic a flow for water ice under Martian conditions, arguing that CO_2 was deposited out of the atmosphere and formed glaciers in high-latitude regions.

5.6   The 'debris-covered glacier' vs. 'rock glacier' models

Colaprete & Jakosky (1998) consider the potential flow rates of rock glaciers and debris-covered glaciers of relatively pure ice Mars, noting that temperatures above ~ 220K would be needed to produce flow even of pure water ice glaciers, given low accumulation rates of ~ 1cm frost per year, and that 'rock glaciers' with a larger rock fraction would flow increasingly slowly. The debris-covered ice glacier model may be preferred, given that the debris cover mitigates some of the problem with the expected low accumulation rates by suppressing sublimation, providing there is enough debris for insulation to dominate over the albedo effect. Whalley & Azizi (2003) make analogies with terrestrial examples of rock glaciers but acknowledge the difficulties in comparison where the interpretation of many Earth-based rock glaciers, variance in terminology in the literature, and the lack of ground reference data for Mars, make it difficult to ensure comparability of the analogy. Further

comparisons are made in Mahaney *et al.* (2007).

Falaschi *et al.* (2014) detail rock glaciers in the arid parts of the high Andes, finding rock glaciers generally found above 4600m (at a latitude $\sim 24°$S). Perucca & Angillieri (2011) note that rock glaciers are able to occur at lower altitudes than pure-ice glaciers in the high Andes. The high level of solar insolation in arid tropical mountain regions of the Earth exceeds that which would be the case on Mars by a factor of over 2, however at high Martian obliquity, summer insolation would have been continuous at mid-latitudes. They are also widespread through the Andes in Central Chile and Argentina at $30°$S to $35°$S as studied in Corte (1980) and Brenning (2005). Rock glaciers are also found in other high-altitude mountain areas including many parts of the Himalayan ranges, (Hewitt, 2014) as well as debris-covered glaciers such as the Khumbu glacier near Mount Everest. (Nakawo, Yabuki & Sakai, 1999).

Hauber *et al.* (2011) remark on Svalbard as a terrestrial Mars analogue, which though not as arid and cold as the Antarctic Dry Valleys, exhibits a variety of landforms including rock glaciers and protalus ramparts, which have morphological analogues on Mars. This study is analogous to this work in the respect it uses the airborne version of HRSC (HRSC-A). (Hauber *et al.*, 2000; Scholten & Wewel, 2000; Otto *et al.*, 2007) This has a similar resolution for airborne use ($\sim$ 20cm/pixel)[2] as HiRISE has on Mars, allowing the authors to make direct comparisons to Martian landforms.

Marchant & Head (2003) detailed a model outlining the classification of Earth rock glaciers in to 'periglacial', and 'glacial' groups, the 'glacial' group being transitional to debris-covered glaciers. They suggest both types could be found on Mars, and forms of both types can be found in the Antarctic Dry Valleys, as well as in other areas such as Svalbard and Disko Island off West Greenland. (Humlum, 1988; Ødegård *et al.*, 2003)

Head *et al.* (2005) argue for a high ice/debris ratio in lobate debris aprons, since their tendency to flow around topographic obstacles on a local scale shows a sufficiently low viscosity to preclude high debris concentrations, which would reduce flow rate to extremely low levels.

---

[2]Depending on flight altitude, panchromatic resolution is quoted as 0.12-0.20m per pixel by Hauber *et al.* (2000) in their study of a glacier in Austria.

5.7   Context of longer-term Martian history

Head *et al.* (2010) suggest a three-phase model, with the ice congregating in tropical mountain glaciers around the Tharsis volcanoes and Elysium at the highest obliquities (Shean, Head & Marchant, 2005; Milkovich, Head & Marchant, 2006; Shean *et al.*, 2007; Fastook *et al.*, 2008), and mid-latitude glaciers forming at moderate levels of obliquity around $35°$. Neukum *et al.* (2004) suggest that relic forms of high altitude tropical mountain glaciers may still exist if ice is protected from sublimation by a sufficient debris cover.

Kargel & Strom (1992) detailed a possible large scale glaciation of many areas in the southern hemisphere, with an extended southern polar ice sheet, and ice in the Hellas basin and other areas. It is an interesting question how far back in time large ice sheets may have existed on Mars. The age of the glacial landforms in Hellas noted by Kargel & Strom (1992) is poorly constrained but likely between 0.25 and 2.3 Gyr. It is likely that extensive glaciation was restricted to certain time periods, likely constrained by the obliquity cycle, based on a comparison with the extent of glacial erosion in Canada during the 2 Myr of the Pleistocene, even allowing for the likelihood of a slower pace of activity on Mars due to colder temperatures and lower surface gravity, a billion year ice age is not needed for the amount of erosion observed. Banks *et al.* (2008) detail evidence for glacial erosion of areas in the Argyre region using HiRISE data. Head *et al.* (1999) and Kreslavsky & Head (2002b) studied the possibility of a past ocean on the northern plains of Mars, based on supposed past shorelines observed, but later work after more high resolution data became available, led to the evidence becoming more ambiguous. (Head *et al.*, 2001; Carr & Head, 2003; Ghatan & Zimbelman, 2006).

Hauber *et al.* (2008) detail what appeared to be former lobate debris aprons, taking the form of topographic depressions around mesas, at low latitudes east of Elysium, and in Kasei Vallis, similar to the currently observed mid-latitude forms. They state a hypothesised age of ~ 1 Gyr for these forms. Moore & Wilhelms (2001) suggested that Hellas Planatia contained an ice-covered lake earlier in Martian history.

Dickson, Fassett & Head (2009) studied Lyot Crater, the lowest point in the topography of the northern hemisphere at $\sim 50°$N, noting Amazonian aged fluvial systems, which indicate liquid water at the surface, and hypothesise that Lyot represented a microclimate at various times in the Amazonian, especially at the most extreme values of obliquity, whereby the temperature could be suitable for

liquid water for periods during summer, and the atmospheric pressure higher than most of Mars due to its low elevation. Morgan, Head & Marchant (2009) suppose a model where large scale glaciation producing the large lineated valley fill and lobate debris aprons in the Deuteronilus Mensae northern hemisphere dichotomy region took place 100-500 Myr ago, with the recent glacial epochs of the last few Myr being much more limited.

5.8 Glaciovolcanic activity on Mars

Glaciovolcanic features have been studied for Mars, including work by Neukum *et al.* (2004). Zealey (2009) studied a region of Mars to the east of the Tharsis plateau, Echus Plateau, finding sinuous ridges interpreted as evidence for subglacial volcanic eruptions. Keszthelyi *et al.* (2010) used HiRISE imagery to detail examples of several glaciovolcanic features in a variety of locations, mainly in the tropical regions of Mars, but some into the low mid-latitudes. Martínez-Alonso *et al.* (2011) investigate Chryse and Acidalia Planitiae using HiRISE imagery, detailing possible volcanic origin of mesas along the dichotomy boundary, and make analogues with terrestrial 'tuyas' produced by subglacial volcanism. Examples of these found in the Tuva Republic of Russia are detailed in Komatsu *et al.* (2007). Pedersen (2013) details possible Martian 'lahars', volcanically derived mudflow features, in the area north of Elysium.

Confusion with glaciovolcanic forms is not very likely to be important for this work, since large scale volcanic activity ceased outside the Tharsis and Elysium regions before the Amazonian, and is not expected to have been active in the last few million years in the mid-latitudes.

5.9 Recent activity of gullies on Mars

The southern wall of Greg Crater shows gully formations, and does not have any GLFs catalogued in Souness *et al.* (2012). Hypotheses for Martian gully formation include snowmelt, groundwater eruption (perhaps as strong brines), and CO_2 cryoclastic flows. It is an open question why certain slopes show evidence for gullies, and others glaciers. It is possible that the two types of feature be linked, if initially, ice-cemented rock and debris, like a rock glacier, forms on a slope, then at a later time, the ice sublimates, and this leaves poorly consolidated material that is easily

eroded by gullies. In Arfstrom & Hartmann (2005), it is offered that gullies could have been formed by melt from ablating glacial features.

Balme *et al.* (2006) compared orientations of southern hemisphere gullies at mid-latitudes to higher latitudes, noting that some studies had found that equator facing gullies are more common at high latitudes, and pole facing at lower latitudes. The study of Dickson, Head & Kreslavsky (2007) found the majority of gullies to be on pole-facing slopes between 30°S and 45°S. Bridges & Lackner (2006) made a study of the northern hemisphere and favoured a snowmelt model of gully formation. Head, Marchant & Kreslavsky (2008) describe the expected insolation of a south facing slope at 43° obliquity and 40°S latitude, and note that in early spring, the slope receives less insolation than a flat surface, whereas at the summer solstice, the peak level is higher, due to continuous daylight under a circumpolar Sun. This means accumulation may proceed through the spring, then melting in a short period of intense insolation around the summer solstice, leading to gully formation.

Dundas *et al.* (2010) presents HiRISE imagery of fresh gully activity, explained by a CO_2 frost model, which does not require liquid water, or water ice snowmelt. This is not claimed to be exclusive to the hypothesis of H_2O driven activity at higher obliquity, and further detail activity in Dundas *et al.* (2012). Johnsson *et al.* (2014) detail gully activity in a young crater at $\sim$ 45°S since the formation of the crater $\sim$ 0.2 Myr ago. Comparing the flows to those observed on Svalbard, these authors believe these gullies have been formed by water bearing debris flow. Levy *et al.* (2009) compared the snowmelt hypothesis of Martian gully formation to gullies observed in the Antarctic Dry Valleys.

Hobley, Howard & Moore (2014) study 'fresh shallow valleys' in the mid-latitudes of Mars, which appear associated with viscous flow features. In view of the problem in formation of these under current-like hyperarid Martian atmosphere within the Amazonian era, the authors conclude these were formed subglacially, beneath ice sheets 10-100m thick. In some cases, these valleys appear to flow uphill, which can occur under ice sheets when the flow is under hydraulic pressure.

5.10 Discussion of topographic analysis methodology and limitations of this work

5.10.1 Is it possible to be predictive of glacier locations?

The classifier picks out sources of viscous flow fairly well, however is not specific to the Souness GLFs, also picking up the older lobate debris apron around north of Olympus Mons, and other features including crater fill features. See for example figures 4.10 and 4.17. It may be a way to find search areas, which may find new glacial features, or make new discoveries by finding something new in areas which might be expected to have glacial features but do not. A further refinement making use of contextual information about topography, as well as the attributes of individual segments could be a route towards a more specific classifier.

5.10.2 Scale dependence of topographic analysis

This method has not taken account of the scale dependence of the topographic variables. This is a particular issue for this work, due to the variable resolution of the HRSC DTM data, between 50m and 250m/pixel.

The issue of scale in the analysis of a DTM is an important one, but can be complex to deal with, particularly if the features of interest to the study are either distributed across a wide range of scales, or poorly constrained in expected scale. The use of multiple windowing sizes, such as in Wood (1999) can be a way to cope with this within the differential geometry based framework of derived topographic layers. In an object-based methodology, a local variance method, as in Drăguț, Eisank & Strasser (2011); Drăguț & Eisank (2011) can be used to quantify the change in derived parameters for objects of interest as the windowing size increases. However, using a multiple windowing method increases the complexity of the analysis, and this can for large terrains, or for high resolution DTMs, increase the computational time required considerably.

5.10.3 Conceptual challenges

There is a conceptual challenge in translating semantic descriptions into quantitative classifications at the level of landform elements returned by a segmentation method. Eisank, Drăguț & Blaschke (2011) considers this for glacial 'cirque'

forms, and Evans (2012) further reviews the issue. The 'geomorphons' method of Jasiewicz & Stepinski (2013) may well have a more direct link to semantic categories of landform than differential geometry quantities.

Ground reference data is only available from a limited number of robotic landers for Mars. Even in relatively accessible regions of the Earth, there are significant controversies over climate history in deep time, for example Triassic to Pliocene ages have been proposed for the onset of hyperaridity in the Atacama. (Rech *et al.*, 2010).

The deep time dimension of Mars' terrain is a significant conceptual challenge. Differentiation of current and recent activity from ancient activity can be more of an issue on Mars, because very little of the Earth's surface displays billion year old terrains but large parts of Mars do. Glaciologists studying the Earth must avoid confusion between features produced by the last glaciation maybe 20 kyr ago, and the previous one a few hundred thousand years ago, whereas on Mars, it is possible to observe features a billion years old.

The possibility of preservation of glacier ice for millions of years in the sub-surface and the possible complex history of features are discussed in Arfstrom & Hartmann (2005) and possible long-term preservation of ice beneath the northern plains of Mars was suggested by Clifford & Parker (2001). For the crater Asimov at 47°S, 5°E, ages of > 8Myr have been proposed for glacial activity by Morgan, Head & Marchant (2011). It is not obvious why in this case, activity appears to date back further in time than other areas active in the last 4 Myr. This may be due to differences in composition, e.g. debris fraction, that is generally poorly constrained for individual objects on Mars. Parsons, Nimmo & Miyamoto (2011) proposes lobate debris apron emplacement some $\sim$ 100 Myr - 1 Gyr ago, and very slow flow of order 10m Myr^{-1}, under current Martian conditions, without the requirement for a significantly warmer climate.

There are processes operating on Mars now and in the past that do not have a direct Earth analogue, for example the White Mars model of CO_2 cryoclastic flows on Mars (Hoffman, 2000). Though this model is unlikely to be thought plausible in full given current knowledge, CO_2 cryoclastic flows are a favoured explanation by many for current gully activity.

5.11 Possible future work

Potential further avenues of study include:

5.11.1 Expanding data coverage

Using all available HRSC DTMs in the mid-latitude ranges, and see to what extent the classifier function predicts glacial activity in areas where there were no GLFs catalogued by Souness *et al.* (2012).

Using other training sets. Rather than simply presence/absence of glacier-like forms, use training sets for other landscape classes that may reduce the presently vast commission error, and examine whether GLFs of the Souness catalogued type can be isolated.

Trace the centrelines of Souness catalogued objects from MRO CTX images, to create a set of linear profiles, to compare slope profiles with Earth-based examples, and theoretical expectations, such as steeper slopes that would be expected for very slow flows as Colaprete & Jakosky (1998) detailed.

Extend the study to the tropical high-altitude regions, where Head *et al.* (2005) mentioned that some recent high-obliquity epochs may have led to glacier flow at the base of the Mount Olympus scarp. This is further discussed in Milkovich, Head & Marchant (2006). Hauber *et al.* (2005) studied glacial features which they estimated at 5-25 Myr age at Hecates Tholus. Schon & Head (2012) show evidence for glacial flow on Tharsis within the last $\sim$ 12.5 Myr, based on observation of pedestal craters superposed on a young impact craters.

5.11.2 Addressing scale issues in the topographic analysis

Use a multi-windowing scheme for the topographic variables, though this may well increase computational time beyond that practicable for a large scale study, or alternatively, use the Stepinski geomorphons method for the initial segmentation to objects and calculate topographic information for these objects. It is much more time-consuming to segment the image-topographic feature vector, and would be even more so with an expanded vector including derived layers at multiple scales, than it would be to simply calculate these quantities at multiple scale layers for objects segmented using by geomorphons.

This work has focused on applying to the global scale, however it may be fruitful to use a particular spatial area of interest, to make a study testing the

impact of choice of windowing scale, as well as use of different terrain attributes, such as local relief measures, and different classification methods, for example support vector machines, fuzzy rule-based, etc.

Another avenue of further study would be to develop the object based method beyond considering the features of individual objects, to considering the properties of neighbouring objects, and local context. The classification from terrain attributes to 'fuzzy' landform elements of Schmidt & Hewitt (2004) used a two step process, first considering the local topographic variables, and then reclassifying, considering the local context of the elements. The 'geomorphons' method may also be fruitful since it can be used to classify the landscape position to features such as footslope, ridge, pit, shoulder, valley etc. that describe the context of an area of terrain. (Jasiewicz & Stepinski, 2013).

Applying automated methods to analyse topography from a HiRISE DTM. This would however be difficult to be directly comparable due to the difference in scale. A multi-level approach may be useful here, locally using texture-based methods to identify terrain types in the HiRISE data, before aggregating to landform level objects later in the classification.

5.11.3   Modelling of climate and glaciers

Do climate modelling of different obliquity conditions. Forget *et al.* (2006) found at $45°$ obliquity ice deposition expected on the flanks of Tharsis volcanoes, and east of Hellas, but not in the Deuteronilus-Protonilus Mensae region, where a lot of the Souness GLFs are found. There are some unknown quantities involved, for example the amount of subsurface CO_2 ice that could be made available to the atmosphere under higher obliquity, in the absence of this knowledge an accurate model is difficult.

Make a detailed study of the lowest elevation GLFs in the Souness catalogue, in comparison to the general population, looking for any systematic differences in morphology. If HiRISE images covering the objects are available, measure a crater age using small craters, and compare to examples such as Greg Crater believed to be ~ 0.4 Myr of age, to see whether the low elevation objects are younger, and if so, whether it is possible to constrain the last probable epoch where they could have formed, based on the back-simulated evolution of Martian obliquity, and a climate model.

5.11.4 Future prospects in Mars exploration

The NASA Mars Atmosphere and Volatile Evolution Mission spacecraft has recently entered Martian orbit, performing Mars orbital insertion on 21st September 2014, and will study the upper atmosphere of Mars. This mission aims to study the escape of volatile elements from the atmosphere over time which may bring insights into the earlier climate history of Mars. The Indian Space Research Organisation also has a spacecraft which arrived at Mars on 24th September 2014. The 'Mars Orbiter Mission' also known as Mangalyaan[3] is carrying an optical camera, infrared imaging spectrometer, and further instruments to study the concentration of methane in the atmosphere and the deuterium/hydrogen ratio.[4] The 2016 ExoMars orbiter, as well as acting as a communication relay in support of the planned 2018 ExoMars rover, will also study trace gases in the Martian atmosphere.

Brown *et al.* (2014) put forward the case for a new LiDAR instrument for Mars, given that the MOLA study, while very successful, was an instrument from the early 1990s, given that it was a reflight of the instrument from the failed Mars Observer mission, and that modern LiDAR technologies have the potential to improve upon it. Specifically, a multi-wavelength near-infrared LiDAR could investigate the behaviour of H_2O and CO_2 ices on Mars, through the seasonal changes in the environment on Mars.

The HiRISE instrument on MRO has provided a stream of very-high resolution images, however there are some ideas to improve further. The USA National Reconnaissance Office has donated two optical assemblies to NASA comparable in size to the Hubble Space Telescope (2.4m objective mirror). A proposed use of one of these is the Mars Orbiting Space Telescope, where the telescope would be able to conduct both remote sensing of the Martian surface, at resolutions as fine as 8cm per pixel, and astronomical observations. Another idea is a balloon-based aerobot mission on Mars, which has been studied by Barnes *et al.* (2005).

A lander on Mars that lands on terrain where recent glacial activity is supposed to have taken place, and drills into the subsurface would be an excellent way to further investigate the hypotheses concerning glaciers. Subsurface exploration using a 'mole' in a similar way as planned for Beagle 2 has been studied for Mars in the Vanguard mission concept (Ellery *et al.*, 2005). A possible drilling mission is

---

[3]'Mars Craft' in the Sanskrit language.

[4]This is an important quantity for studying the history of volatile loss, since the heavier deuterium nuclei are less likely to escape to space than ^{1}H nuclei, the ratio may allow constrains to be put on the amount of hydrogen that has escaped to space since Mars' formation.

examined in the 'Icebreaker' (Glass *et al.*, 2008) mission concept. A lander for the mid-latitude glaciers is however not immediately likely to happen, since current and planned lander missions are focused on more ancient terrains, that may be more likely to contain evidence for past life on an early, warmer, wetter Mars.

Chapter 6

Conclusions

This study has expanded the range of descriptive statistics available for the objects catalogued and studied in Souness *et al.* (2012), by adding HRSC topography, for 1047 of the 1309 catalogued glacier-like forms in that work. Statistics on image brightness, elevation, slope, aspect, and topographic curvature layers have been calculated for the extents of the catalogued GLFs.

The basic result of Souness *et al.* (2012) on the topographic conditions that are associated with the glacier flows, that they are most abundant in areas of moderate relief, can be made more specific, that the preferred slope is $\sim$ $10-15$ ° on average across the extent of the objects, and that the head areas most commonly have slopes $\sim$ $15-20$ °. These objects are also most commonly found in areas of negative longitudinal and cross-sectional topographic curvature, i.e concave slopes and valley or cirque-like topography. These results may be evidence for the importance of wind-borne redeposition of snow, and/or wind-controlled sublimation in the formation or preservation of glaciers on Mars.

A classifier function for a segmented feature vector of the images and topography, trained based on these descriptive statistics, appears to be successful in predicting potential source areas of glacial flow on Mars, but is not successful in isolating the specific feature type that Souness *et al.* (2012) catalogued from other glacially related features. It is suggested that it would be necessary to use a classifier that is context-aware as well as examining the attributes of individual objects to separate the different types of glacial related features observable on Mars.

The classifier function also picks certain regions that, for example in the lower slopes of crater Greg, that do not appear to have current glaciation, but have been hypothesised to have been glaciated in the past in the work of Fassett *et al.*

(2010). It may be that a classifier such as this can assist in search for terrains where past glaciers that have now fully ablated were found.

Acknowledgements

Appendix A

Global maps

The maps in the following pages show the mid-latitudes of Mars, using a colourised MOLA topography overlaid on a Mars Orbiter Camera wide-angle mosaic via transparency. Locations of the HRSC tiles used, labelled by the first five characters of the product ID number and the topographic resolution are shown.

The Souness *et al.* (2012) glacier extents are also labelled, numbered by their catalogue numbers.

Not all HRSC tiles and Souness GLFs are labelled, since the GIS software used, `QGIS`, automatically avoids label overcrowding and in this case does not plot all labels.

The colour ramp for elevation used is blue for low elevation, red for high elevation, in the sequence blue, green, yellow, orange, and red from low to high.
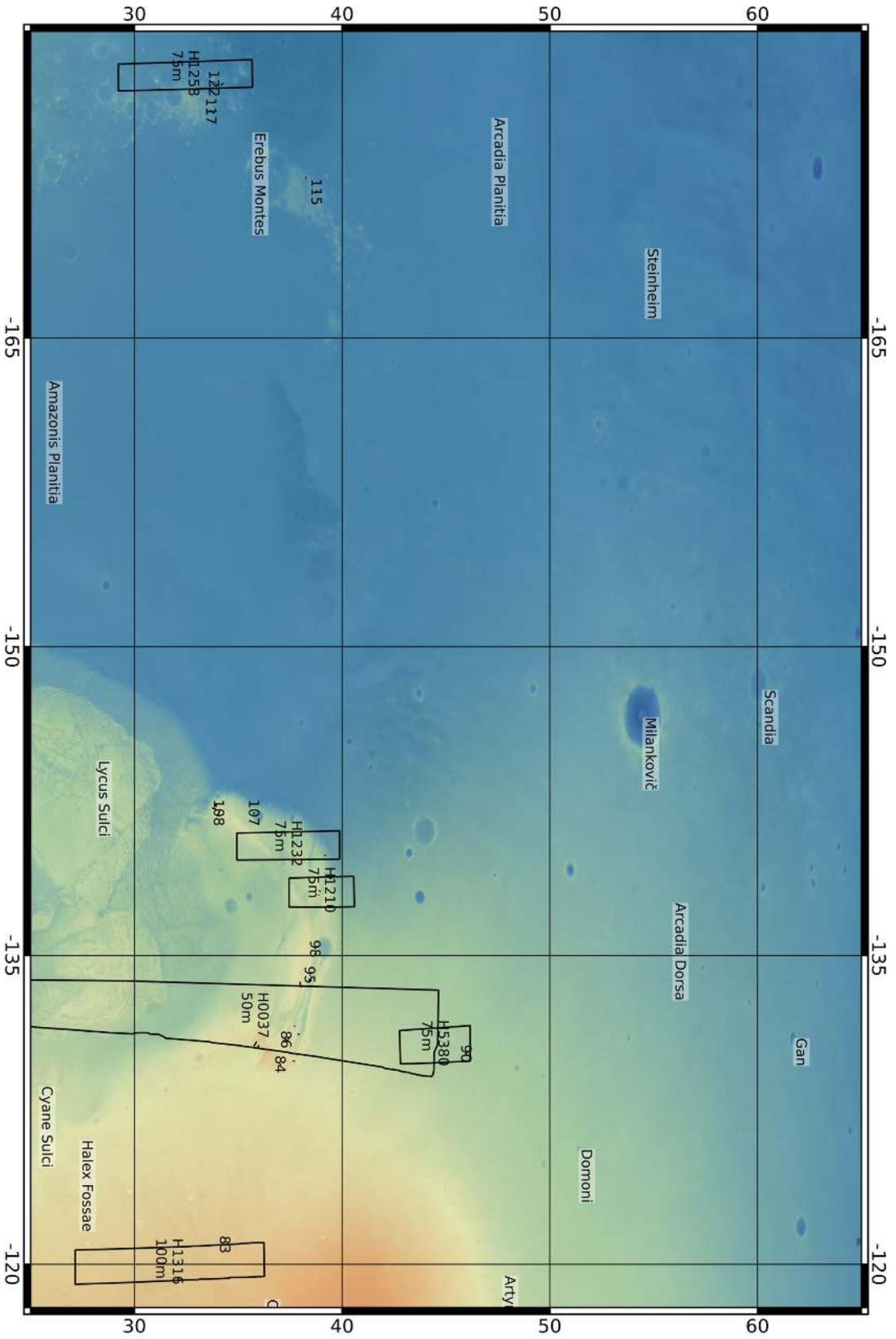
Figure A.1: Northern Hemisphere, panel 1
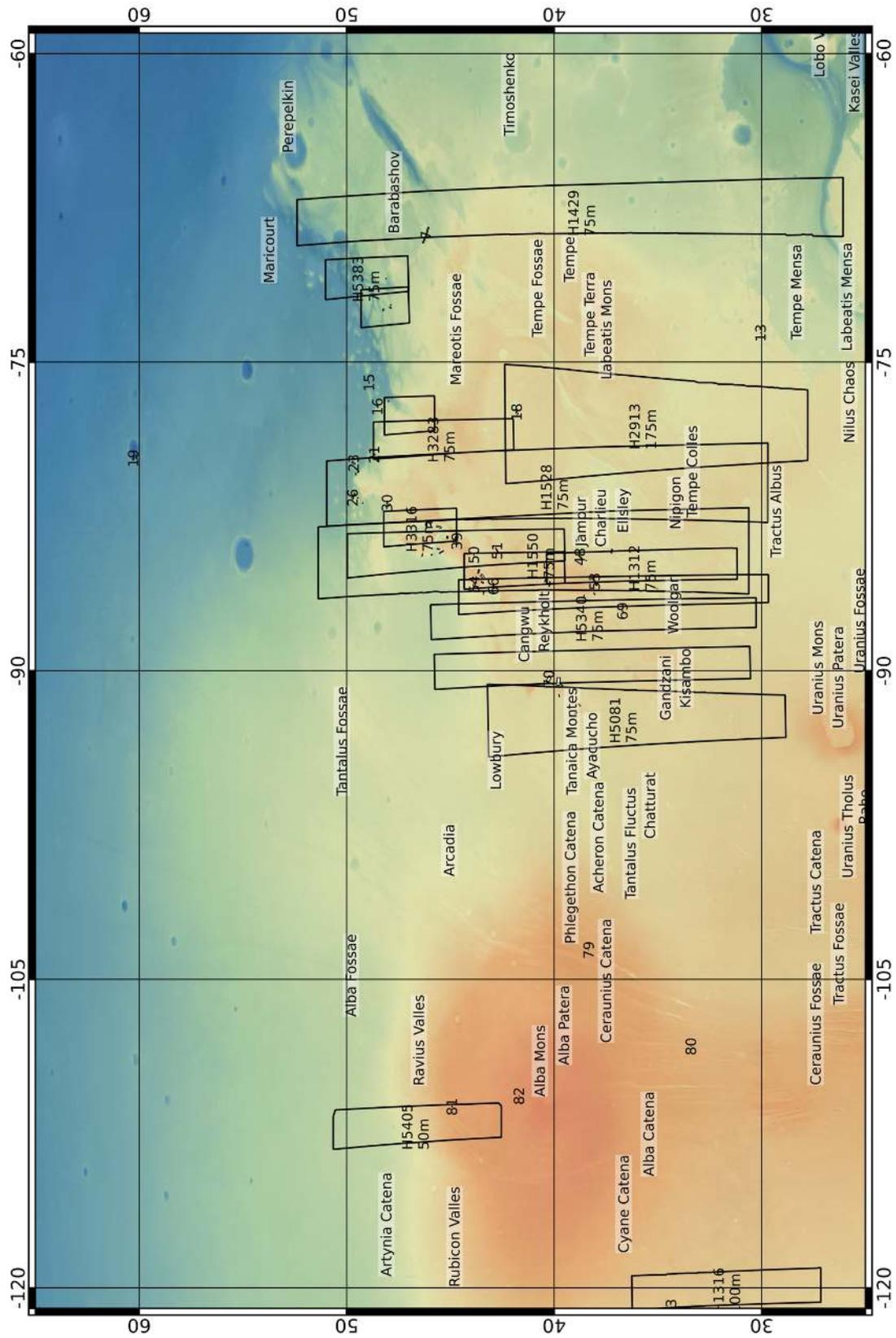
Figure A.2: Northern Hemisphere, panel 2
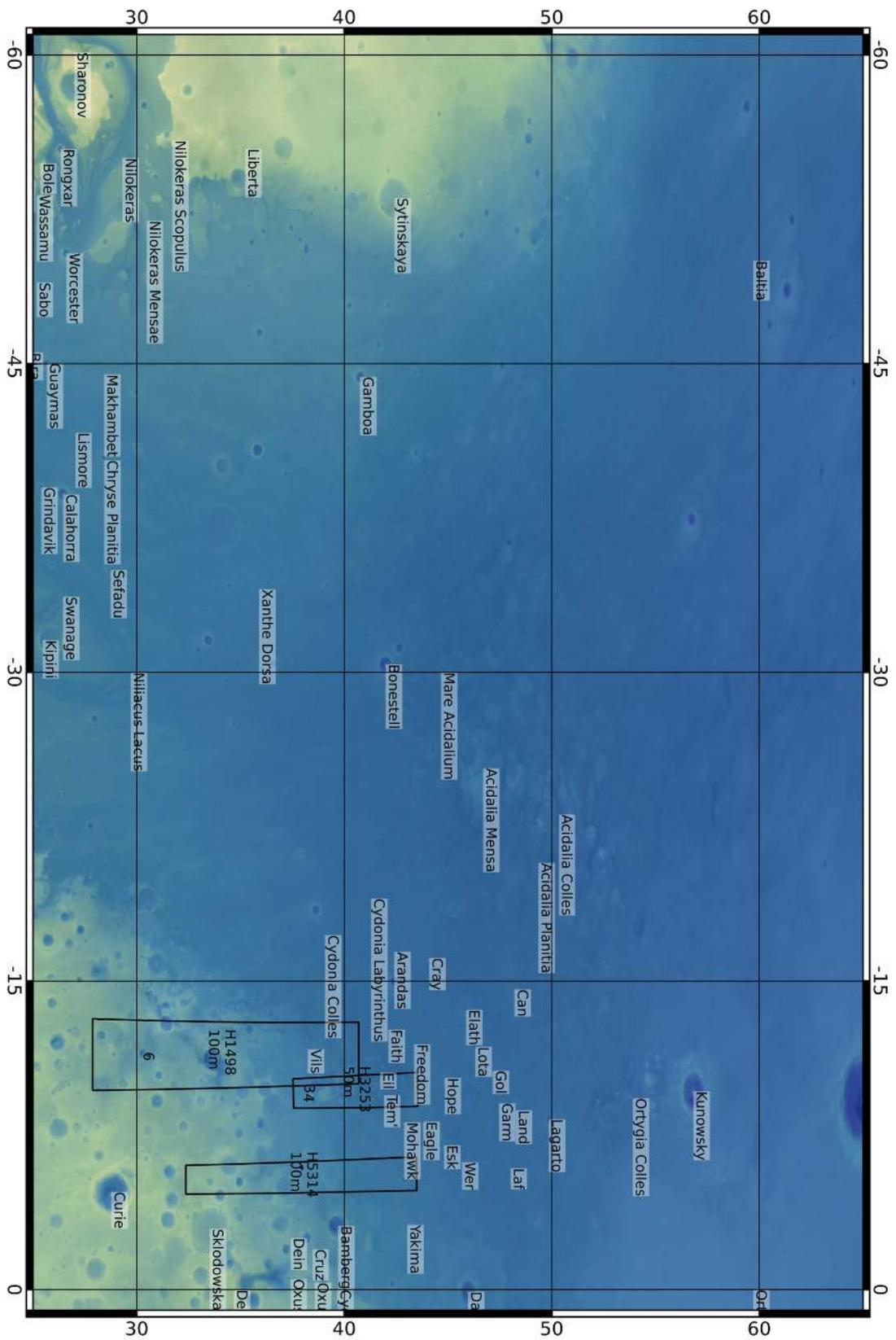
Figure A.3: Northern Hemisphere, panel 3

Figure A.4: Northern Hemisphere, panel 4
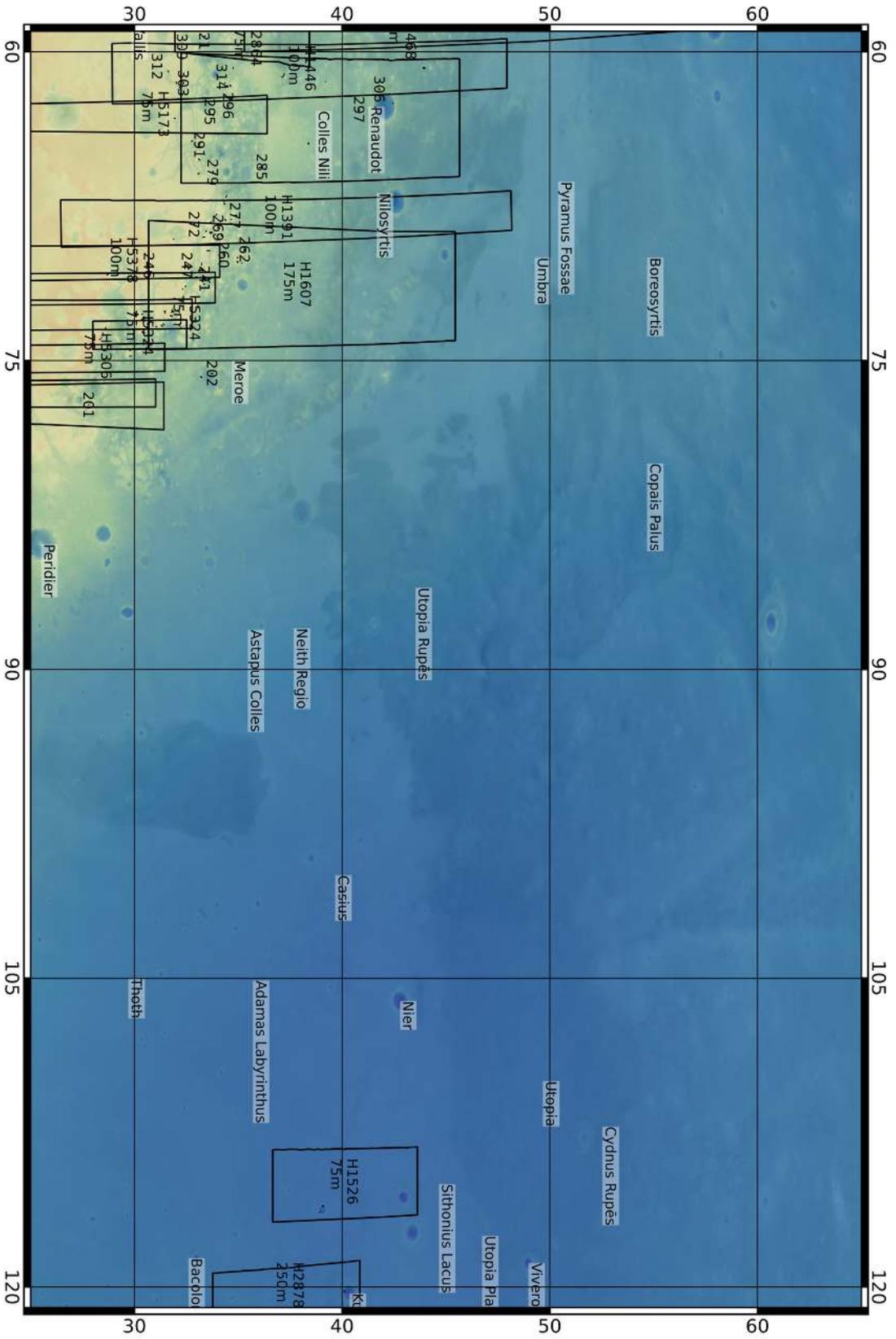
Figure A.5: Northern Hemisphere, panel 5
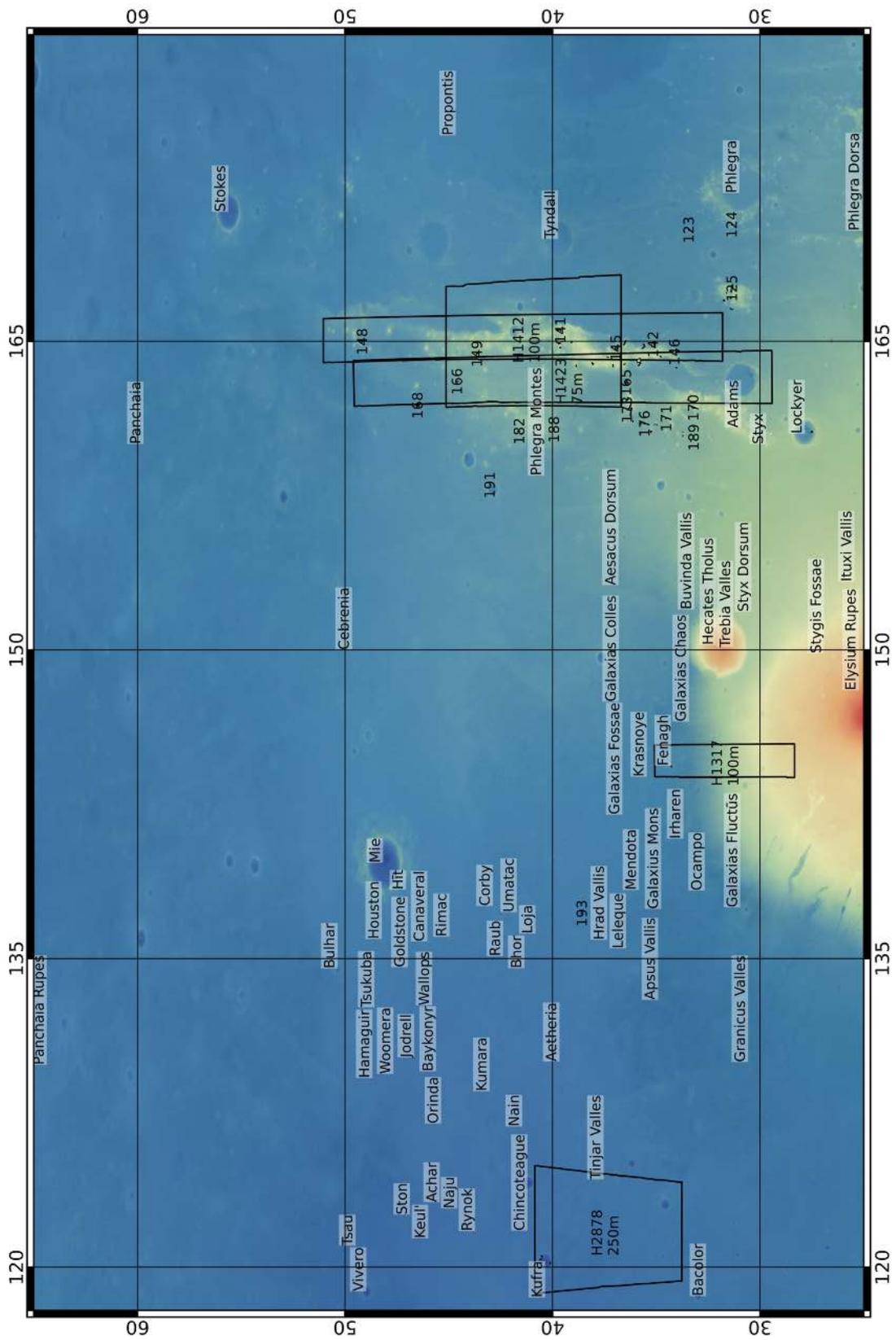
Figure A.6: Northern Hemisphere, panel 6
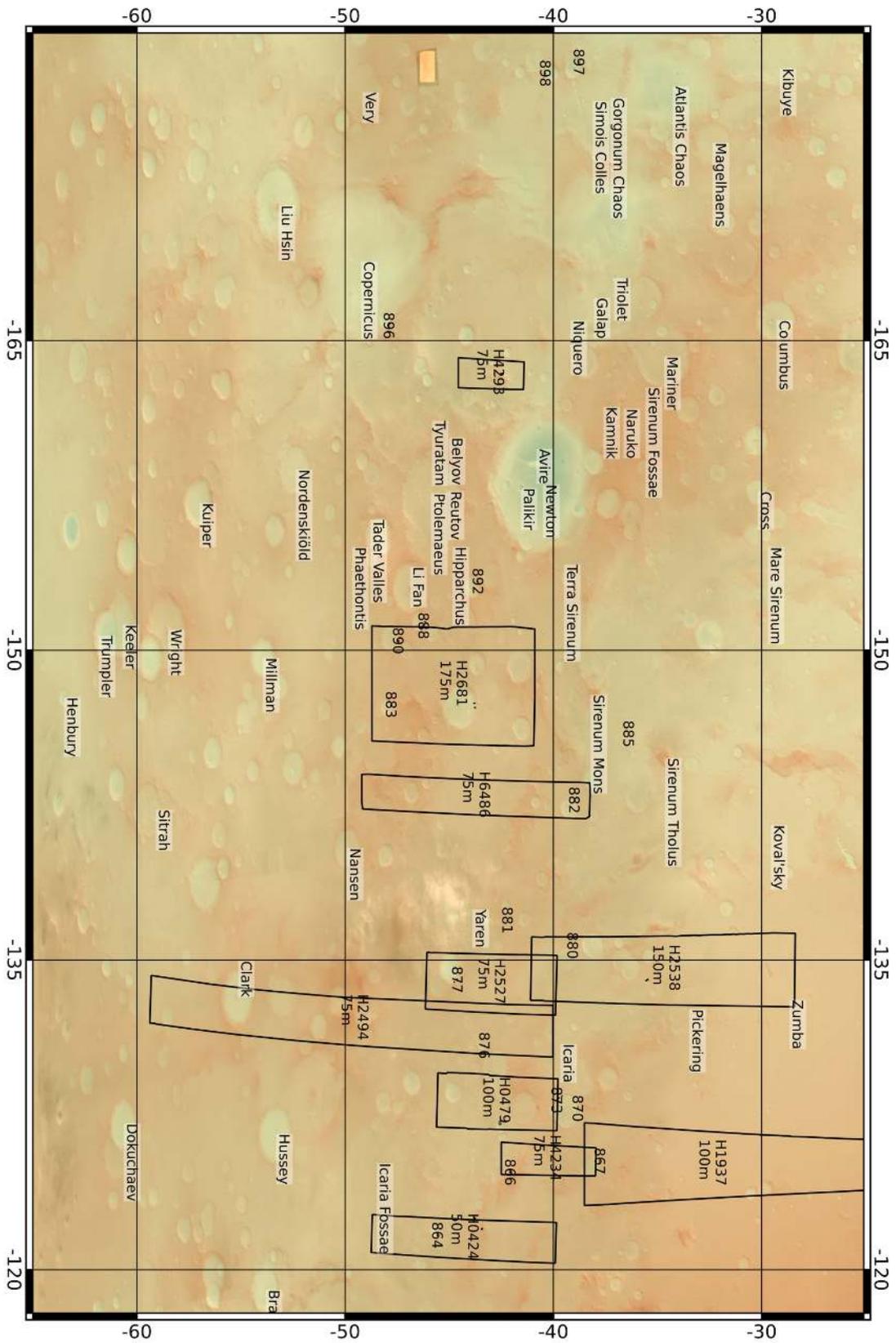
Figure A.7: Southern Hemisphere, panel 1
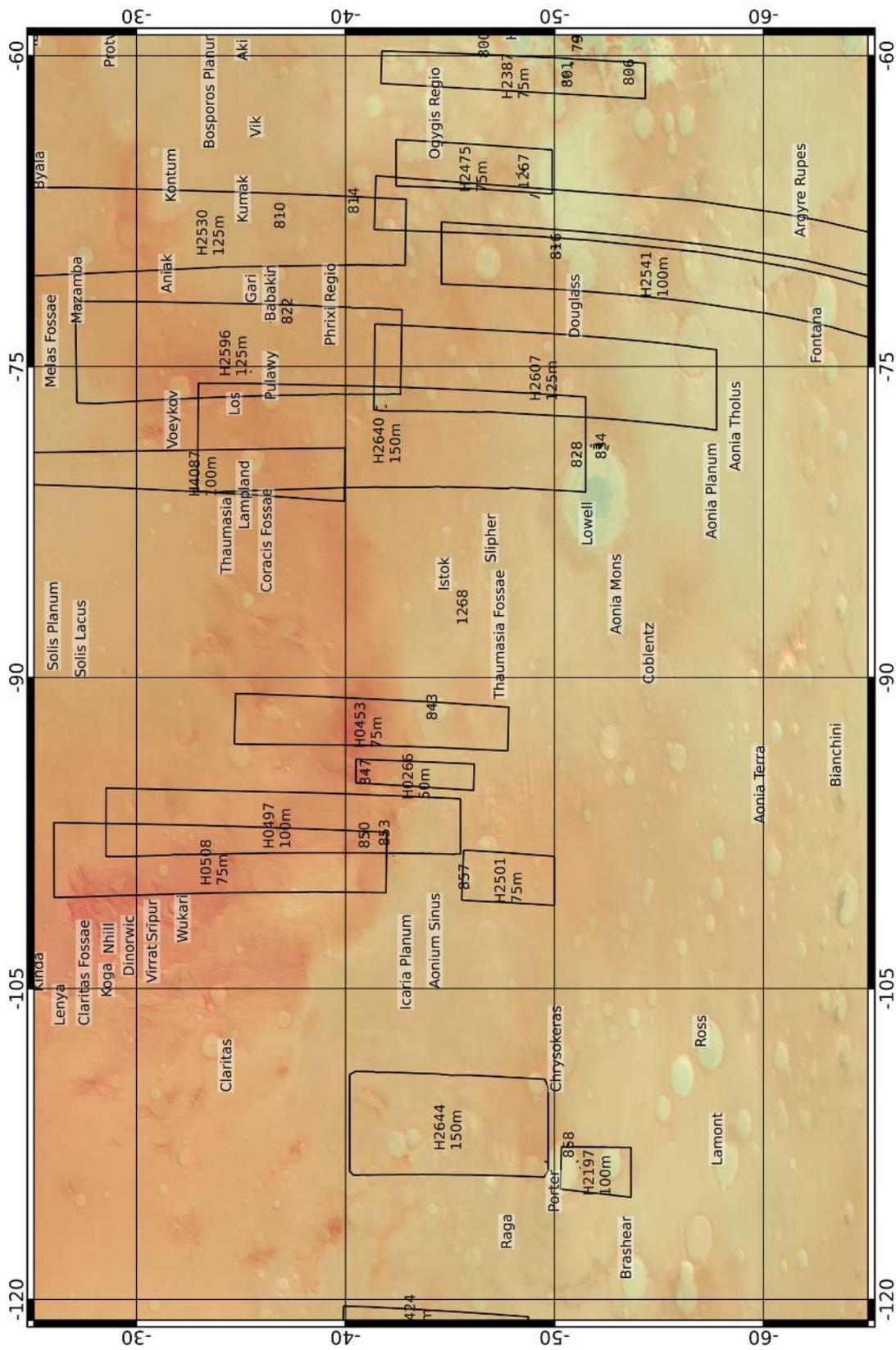
Figure A.8: Southern Hemisphere, panel 2
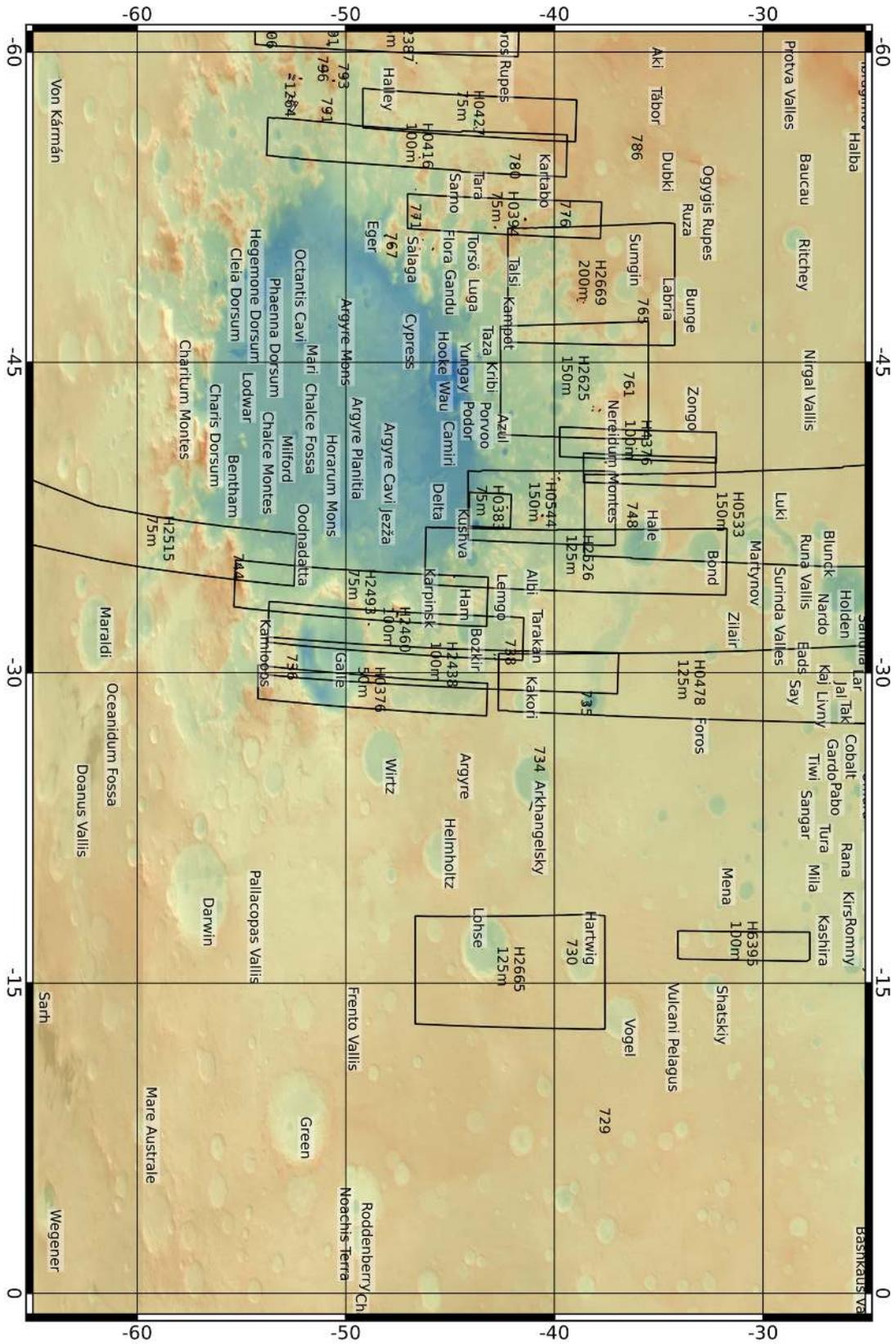
Figure A.9: Southern Hemisphere, panel 3

Figure A.10: Southern Hemisphere, panel 4

Figure A.11: Southern Hemisphere, panel 5
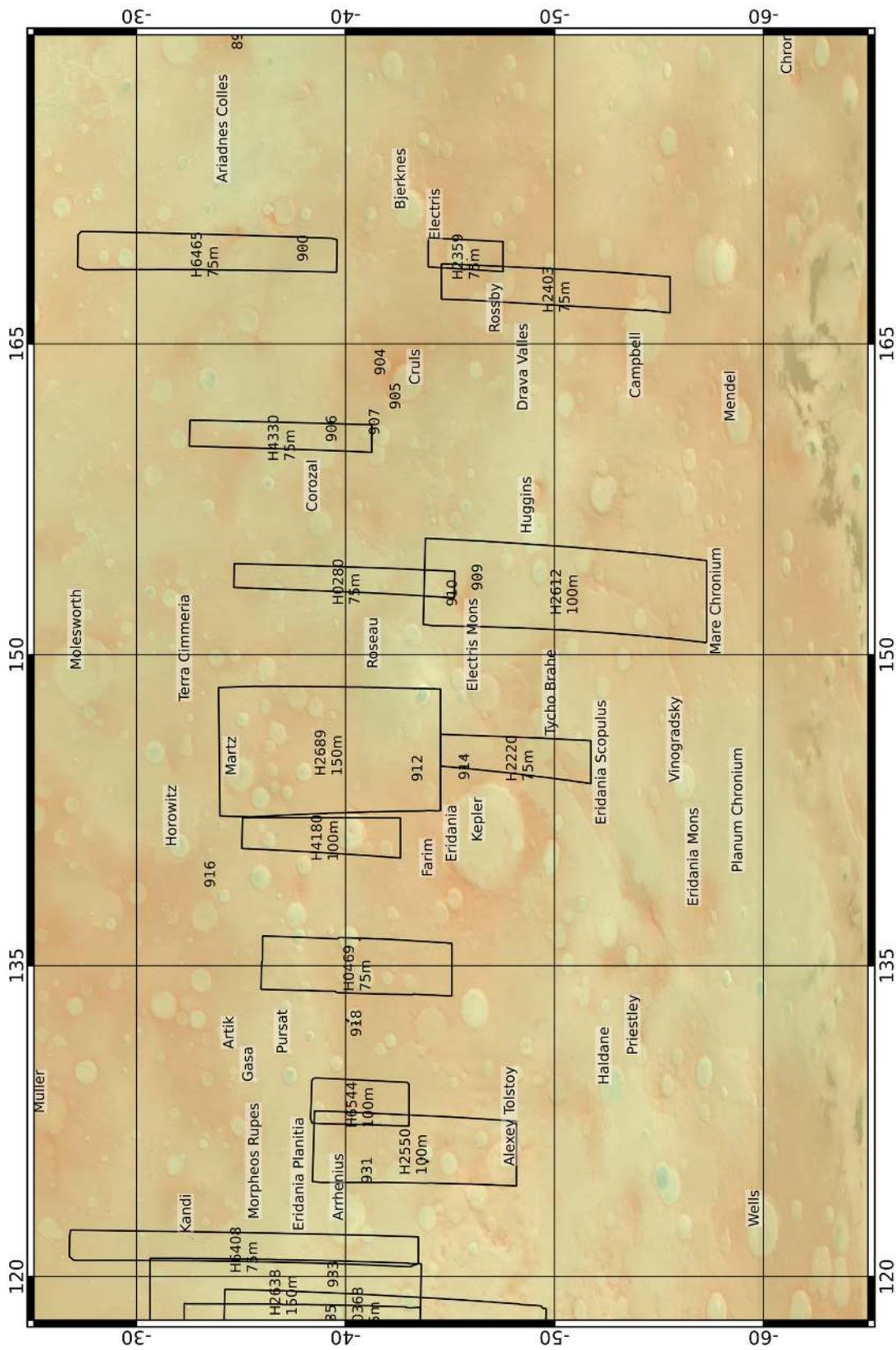
Figure A.12: Southern Hemisphere, panel 6

Appendix B

List of HRSC tiles

Table B.1: A full list of the 179 HRSC tiles used in this work, detailing the product ID, latitude and longitude of centre and the DTM resolution, sorted by the DTM resolution.

Product ID	Centre Latitude	Centre Longitude	DTM resolution (m/pixel)
H0037_0000	29	-132	50
H0248_0000	-38	102	50
H0266_0000	-44	-95	50
H0376_0000	-49	-30	50
H0424_0000	-45	-122	50
H2279_0001	-42	108	50
H2400_0001	-41	102	50
H3253_0000	40	-10	50
H5286_0000	44	-85	50
H5304_0000	41	-86	50
H5405_0000	46	-113	50
H0280_0001	-40	153	75
H0365_0000	-46	90	75
H0368_0000	-42	118	75
H0383_0000	-44	-38	75
H0394_0000	-43	-53	75
H0397_0000	-38	12	75
H0427_0000	-45	-57	75
H0453_0000	-42	-93	75
H0469_0000	-41	134	75
H0508_0000	-35	-99	75
H0988_0000	22	77	75
H1201_0000	43	24	75
H1210_0000	39	-139	75
H1232_0000	37	-141	75
			Continued on next page

111

Product ID	Centre Latitude	Centre Longitude	DTM resolution (m/pixel)
H1241_0000	44	54	75
H1258_0001	32	-178	75
H1312_0000	35	-85	75
H1351_0001	47	40	75
H1423_0001	39	163	75
H1428_0000	42	30	75
H1429_0000	39	-68	75
H1450_0000	41	28	75
H1461_0000	43	26	75
H1468_0001	47	58	75
H1523_0000	43	49	75
H1526_0000	40	115	75
H1528_0000	40	-81	75
H1545_0000	44	46	75
H1550_0000	41	-85	75
H2159_0001	-46	19	75
H2220_0000	-49	144	75
H2224_0000	-42	112	75
H2247_0000	-54	12	75
H2287_0001	-56	41	75
H2312_0000	-44	107	75
H2345_0000	-46	104	75
H2356_0002	-41	103	75
H2359_0000	-46	169	75
H2386_0000	-51	36	75
H2387_0000	-49	-61	75
H2403_0001	-51	167	75
H2430_0001	-53	35	75
H2441_0000	-51	33	75
H2475_0000	-47	-66	75
H2493_0000	-50	-34	75
H2494_0000	-50	-133	75
H2501_0000	-48	-100	75
H2515_0000	-63	-39	75
H2527_0000	-43	-134	75
H3249_0000	44	21	75
H3272_0000	46	-78	75
H3283_0000	45	-79	75
H3316_0001	46	-84	75
H4234_0000	-41	-126	75
H4293_0000	-43	-164	75
			Continued on next page

Product ID	Centre Latitude	Centre Longitude	DTM resolution (m/pixel)
H4330_0000	-37	160	75
H4365_0001	-36	-40	75
H5081_0000	36	-93	75
H5173_0000	27	63	75
H5195_0000	32	22	75
H5213_0000	34	20	75
H5249_0000	35	18	75
H5267_0000	36	16	75
H5281_0000	38	56	75
H5285_0000	36	15	75
H5288_0000	26	76	75
H5299_0000	38	55	75
H5303_0000	36	14	75
H5306_0000	24	74	75
H5322_0000	37	-87	75
H5324_0000	30	73	75
H5339_0000	40	12	75
H5340_0000	38	-88	75
H5342_0000	24	72	75
H5360_0000	28	71	75
H5376_0000	38	-90	75
H5380_0000	44	-131	75
H5383_0000	49	-71	75
H6408_0000	-36	121	75
H6419_0000	-39	99	75
H6465_0000	-34	169	75
H6486_0000	-44	-143	75
H0022_0000	-30	100	100
H0416_0000	-47	-56	100
H0451_0000	-39	102	100
H0479_0000	-43	-129	100
H0497_0000	-38	-97	100
H0528_0000	-30	93	100
H1316_0000	31	-121	100
H1317_0000	31	144	100
H1391_0000	37	68	100
H1395_0000	43	34	100
H1412_0001	41	165	100
H1446_0000	38	60	100
H1483_0000	42	23	100

Product ID	Centre Latitude	Centre Longitude	DTM resolution (m/pixel)
H1498_0000	34	-12	100
H1578_0000	44	42	100
H1628_0000	40	165	100
H1937_0000	-31	-126	100
H2181_0001	-49	17	100
H2195_0000	-46	82	100
H2197_0001	-52	-114	100
H2210_0000	-49	47	100
H2438_0000	-46	-31	100
H2460_0001	-48	-33	100
H2466_0000	-42	99	100
H2508_0000	-55	-69	100
H2529_0000	-49	29	100
H2541_0000	-56	-72	100
H2550_0000	-44	126	100
H2612_0000	-51	153	100
H3289_0000	45	51	100
H4087_0000	-32	-81	100
H4180_0000	-39	141	100
H4376_0000	-36	-42	100
H5314_0000	37	-6	100
H5317_0000	44	52	100
H5321_0000	38	13	100
H5328_0000	43	32	100
H5335_0000	46	51	100
H5378_0000	28	70	100
H5401_0000	48	-73	100
H6395_0000	-31	-17	100
H6409_0000	-30	20	100
H6437_0000	-38	97	100
H6544_0000	-41	128	100
H0478_0000	-24	-31	125
H0506_0000	-34	98	125
H0550_0000	-33	92	125
H0558_0000	-33	25	125
H1600_0001	39	38	125
H2510_0001	-41	96	125
H2526_0001	-39	-36	125
H2530_0001	-34	-69	125
H2596_0001	-35	-75	125

Product ID	Centre Latitude	Centre Longitude	DTM resolution (m/pixel)
H2607_0000	-50	-76	125
H2609_0000	-40	88	125
H2665_0001	-43	-16	125
H5263_0001	-29	57	125
H6552_0000	-46	41	125
H0466_0000	-21	69	150
H0533_0000	-23	-39	150
H0544_0000	-41	-38	150
H1629_0000	38	63	150
H2538_0000	-35	-135	150
H2540_0000	-33	28	150
H2595_0001	-43	24	150
H2625_0000	-40	-45	150
H2638_0000	-38	118	150
H2639_0000	-40	19	150
H2640_0000	-43	-79	150
H2644_0000	-45	-112	150
H2689_0001	-40	145	150
H2908_0000	41	53	150
H2996_0000	28	44	150
H1607_0009	38	71	175
H1644_0000	40	33	175
H2631_0001	-37	86	175
H2660_0001	-38	115	175
H2681_0000	-45	-149	175
H2864_0000	35	57	175
H2913_0000	35	-79	175
H2613_0000	-33	55	200
H2669_0000	-39	-49	200
H1932_0000	-41	6	225
H1887_0000	-42	108	250
H2694_0001	-39	13	250
H2878_0000	37	121	250

Bibliography

Aharonson, O., Zuber, M.T. & Rothman, D.H. (2001) Statistics of Mars' topography from the Mars orbiter laser altimeter: slopes, correlations, and physical models. *Journal of Geophysical Research: Planets (1991–2012)*, **106**, 23723–23735.

Albee, A.L., Palluconi, F. & Arvidson, R. (1998) Mars Global Surveyor mission: overview and status. *Science*, **279**, 1671–1672.

Arfstrom, J. & Hartmann, W.K. (2005) Martian flow features, moraine-like ridges, and gullies: Terrestrial analogs and interrelationships. *Icarus*, **174**, 321–335.

Baker, D.M., Head, J.W. & Marchant, D.R. (2010) Flow patterns of lobate debris aprons and lineated valley fill north of Ismeniae Fossae, Mars: Evidence for extensive mid-latitude glaciation in the Late Amazonian. *Icarus*, **207**, 186–209.

Balme, M., Mangold, N., Baratoux, D., Costard, F., Gosselin, M., Masson, P., Pinet, P. & Neukum, G. (2006) Orientation and distribution of recent gullies in the southern hemisphere of Mars: observations from High Resolution Stereo Camera/Mars Express (HRSC/MEX) and Mars Orbiter Camera/Mars Global Surveyor (MOC/MGS) data. *Journal of Geophysical Research: Planets (1991–2012)*, **111**.

Bandeira, L., Marques, J.S., Saraiva, J. & Pina, P. (2013) Advances in automated detection of sand dunes on Mars. *Earth Surface Processes and Landforms*, **38**, 275–283.

Bandeira, L., Saraiva, J. & Pina, P. (2007) Impact crater recognition on Mars based on a probability volume created by template matching. *Geoscience and Remote Sensing, IEEE Transactions on*, **45**, 4008–4015.

Banks, M.E., Lang, N.P., Kargel, J.S., McEwen, A.S., Baker, V.R., Grant, J.A., Pelletier, J.D. & Strom, R.G. (2009) An analysis of sinuous ridges in the southern Argyre Planitia, Mars using HiRISE and CTX images and MOLA data. *Journal of Geophysical Research: Planets (1991–2012)*, **114**.

Banks, M.E., McEwen, A.S., Kargel, J.S., Baker, V.R., Strom, R.G., Mellon, M.T., Gulick, V.C., Keszthelyi, L., Herkenhoff, K.E., Pelletier, J.D. *et al.* (2008) High

Resolution Imaging Science Experiment (HiRISE) observations of glacial and periglacial morphologies in the circum-Argyre Planitia highlands, Mars. *Journal of Geophysical Research: Planets (1991–2012)*, **113**.

Barata, T., Alves, E.I., Saraiva, J. & Pina, P. (2004) Automatic recognition of impact craters on the surface of Mars. *Image Analysis and Recognition*, pp. 489–496. Springer.

Barnes, D., Shaw, A., Summers, P., Woods, M., Ward, R., Evans, M., Paar, G. & Sims, M. (2005) Autonomous image based localisation for a martian aerobot. *Proc. 8th Int. Symposium on Artificial Intelligence, Robotics and Automation in Space*.

Benn, D. & Evans, D. (2010) *Glaciers and glaciation. 2nd edition*. Hodder Education.

Berman, D.C., Crown, D.A. & Bleamaster III, L.F. (2009) Degradation of mid-latitude craters on Mars. *Icarus*, **200**, 77–95.

Bibring, J.P., Langevin, Y., Gendrin, A., Gondet, B., Poulet, F., Berthé, M., Soufflot, A., Arvidson, R., Mangold, N., Mustard, J. *et al.* (2005) Mars surface diversity as revealed by the OMEGA/Mars Express observations. *Science*, **307**, 1576–1581.

Bibring, J.P., Langevin, Y., Mustard, J.F., Poulet, F., Arvidson, R., Gendrin, A., Gondet, B., Mangold, N., Pinet, P., Forget, F. *et al.* (2006) Global mineralogical and aqueous Mars history derived from OMEGA/Mars Express data. *Science*, **312**, 400–404.

Bliss, A.K., Cuffey, K.M. & Kavanaugh, J.L. (2011) Sublimation and surface energy budget of Taylor Glacier, Antarctica. *Journal of Glaciology*, **57**, 684–696.

Bonnefoy, R., Link, D., Casani, J., Vorontsov, V.A., Engstrom, F., Wolf, P., Jude, R., Patti, B. & Jones, C. (2004) Beagle 2 ESA/UK Commission of Inquiry.

Boynton, W., Feldman, W., Squyres, S., Prettyman, T., Brückner, J., Evans, L., Reedy, R., Starr, R., Arnold, J., Drake, D. *et al.* (2002) Distribution of hydrogen in the near surface of Mars: Evidence for subsurface ice deposits. *Science*, **297**, 81–85.

Brenning, A. (2005) Geomorphological, hydrological and climatic significance of rock glaciers in the Andes of Central Chile (33–35 S). *Permafrost and Periglacial Processes*, **16**, 231–240.

Brenning, A. (2009) Benchmarking classifiers to optimally integrate terrain analysis and multispectral remote sensing in automatic rock glacier detection. *Remote Sensing of Environment*, **113**, 239–247.

Brenning, A. & Trombotto, D. (2006) Logistic regression modeling of rock glacier and glacier distribution: Topographic and climatic controls in the semi-arid Andes. *Geomorphology*, **81**, 141–154.

Bridges, N.T. & Lackner, C.N. (2006) Northern hemisphere Martian gullies and mantled terrain: Implications for near-surface water migration in Mars' recent past. *Journal of Geophysical Research: Planets (1991–2012)*, **111**.

Brown, A.J., Michaels, T.I., Byrne, S., Sun, W., Titus, T.N., Colaprete, A., Wolff, M.J. & Videen, G. (2014) The science case for a modern, multi-wavelength, polarization-sensitive LIDAR in orbit around Mars. *arXiv preprint arXiv:1406.0030.*

Brown, D.G., Lusch, D.P. & Duda, K.A. (1998) Supervised classification of types of glaciated landscapes using digital elevation data. *Geomorphology*, **21**, 233–250.

Bryson, K.L., Chevrier, V., Sears, D.W. & Ulrich, R. (2008) Stability of ice on Mars and the water vapor diurnal cycle: Experimental study of the sublimation of ice through a fine-grained basaltic regolith. *Icarus*, **196**, 446–458.

Bue, B.D. & Stepinski, T.F. (2006) Automated classification of landforms on Mars. *Computers & Geosciences*, **32**, 604–614.

Bue, B.D. & Stepinski, T.F. (2007) Machine detection of martian impact craters from digital topography data. *Geoscience and Remote Sensing, IEEE Transactions on*, **45**, 265–274.

Bunting, P. & Clewley, D. (2014) Remote Sensing and Geographical Information Systems Library Homepage.
URL http://www.rsgislib.org

Burger, D., Stassun, K.G., Pepper, J.A., Siverd, R.J., Paegert, M.A. & De Lee, N.M. (2012) Filtergraph: A Flexible Web Application for Instant Data Visualization of Astronomy Datasets. *arXiv preprint arXiv:1212.4458.*
URL http://www.filtergraph.vanderbilt.edu

Burr, D.M., Soare, R.J., Wan Bun Tseung, J.M. & Emery, J.P. (2005) Young (late Amazonian), near-surface, ground ice features near the equator, Athabasca Valles, Mars. *Icarus*, **178**, 56–73.

Burr, D.M., Tanaka, K.L. & Yoshikawa, K. (2009) Pingos on Earth and Mars. *Planetary and Space Science*, **57**, 541–555.

Byrne, S., Dundas, C.M., Kennedy, M.R., Mellon, M.T., McEwen, A.S., Cull, S.C., Daubar, I.J., Shean, D.E., Seelos, K.D., Murchie, S.L. *et al.* (2009) Distribution of mid-latitude ground ice on Mars from new impact craters. *Science*, **325**, 1674–1676.

Carr, M.H. & Head, J.W. (2003) Oceans on Mars: An assessment of the observational evidence and possible fate. *Journal of Geophysical Research: Planets (1991–2012)*, **108**.

Carr, M.H. & Head, J.W. (2010) Geologic history of Mars. *Earth and Planetary Science Letters*, **294**, 185–203.

Chinn, T. (1980) Glacier balances in the Dry Valleys area, Victoria Land, Antarctica. *Proceedings of the Riederalp Workshop, September 1978*, vol. 126 of *World Glacier Inventory - Inventaire mondial des Glaciers*.

Clark, R.N. & McCord, T.B. (1982) Mars residual north polar cap: Earth-based spectroscopic confirmation of water ice as a major constituent and evidence for hydrated minerals. *Journal of Geophysical Research: Solid Earth (1978–2012)*, **87**, 367–370.

Clifford, S.M. & Parker, T.J. (2001) The evolution of the Martian hydrosphere: Implications for the fate of a primordial ocean and the current state of the northern plains. *Icarus*, **154**, 40–79.

Colaprete, A. & Jakosky, B.M. (1998) Ice flow and rock glaciers on Mars. *Journal of Geophysical Research: Planets (1991–2012)*, **103**, 5897–5909.

Conway, S.J. & Mangold, N. (2013) Evidence for Amazonian mid-latitude glaciation on Mars from impact crater asymmetry. *Icarus*, **225**, 413–423.

Corripio, J.G. & Purves, R.S. (2005) Surface energy balance of high altitude glaciers in the central Andes: The effect of snow penitentes. *Climate and hydrology in mountain areas*, pp. 15–27.

Corte, A. (1980) Glaciers and glaciolithic systems of the Central Andes. *Proceedings of the Riederalp Workshop, September 1978*, vol. 126 of *World Glacier Inventory - Inventaire mondial des Glaciers*.

Craddock, R.A. & Howard, A.D. (2002) The case for rainfall on a warm, wet early Mars. *Journal of Geophysical Research: Planets (1991–2012)*, **107**, 21–1.

Delamere, W.A., Tornabene, L.L., McEwen, A.S., Becker, K., Bergstrom, J.W., Bridges, N.T., Eliason, E.M., Gallagher, D., Herkenhoff, K.E., Keszthelyi, L. *et al.* (2010) Color imaging of Mars by the High Resolution Imaging Science Experiment (HiRISE). *Icarus*, **205**, 38–52.

Dickinson, W.W. & Rosen, M.R. (2003) Antarctic permafrost: An analogue for water and diagenetic minerals on Mars. *Geology*, **31**, 199–202.

Dickson, J.L., Fassett, C.I. & Head, J.W. (2009) Amazonian-aged fluvial valley systems in a climatic microenvironment on Mars: Melting of ice deposits on the interior of Lyot Crater. *Geophysical Research Letters*, **36**.

Dickson, J.L., Head, J.W. & Kreslavsky, M. (2007) Martian gullies in the southern mid-latitudes of Mars: Evidence for climate-controlled formation of young fluvial features based upon local and global topography. *Icarus*, **188**, 315–323.

Dickson, J.L., Head, J.W. & Marchant, D.R. (2008) Late Amazonian glaciation at the dichotomy boundary on Mars: Evidence for glacial thickness maxima and multiple glacial phases. *Geology*, **36**, 411–414.

Drăguț, L. & Eisank, C. (2011) Object representations at multiple scales from digital elevation models. *Geomorphology*, **129**, 183–189.

Drăguț, L., Eisank, C. & Strasser, T. (2011) Local variance for multi-scale analysis in geomorphometry. *Geomorphology*, **130**, 162–172.

Dundas, C.M. & Byrne, S. (2010) Modeling sublimation of ice exposed by new impacts in the martian mid-latitudes. *Icarus*, **206**, 716–728.

Dundas, C.M., Diniega, S., Hansen, C.J., Byrne, S. & McEwen, A.S. (2012) Seasonal activity and morphological changes in martian gullies. *Icarus*, **220**, 124–143.

Dundas, C.M. & McEwen, A.S. (2010) An assessment of evidence for pingos on Mars using HiRISE. *Icarus*, **205**, 244–258.

Dundas, C.M., McEwen, A.S., Diniega, S., Byrne, S. & Martinez-Alonso, S. (2010) New and recent gully activity on Mars as seen by HiRISE. *Geophysical Research Letters*, **37**.

Eisank, C., Drăguț, L. & Blaschke, T. (2011) A generic procedure for semantics-oriented landform classification using object-based image analysis. *Geomorphometry*, **2011**, 125–128.

Eliason, E., Castalia, B., Leis, R. & Becker, K. (2007) Software Interface Specification for HiRISE Experimental Data Record Products. , Jet Propulsion Laboratory, NASA.

Eliason, E., Castalia, B., Mattson, S., Heyd, R., Becker, K., Anderson, J. & Sides, S. (2009) Software interface specification for HiRISE reduced data record products. *MRO JPL Document D-32006*.

Ellery, A., Kolb, C., Lammer, H., Parnell, J., Edwards, H., Richter, L., Patel, M., Romstedt, J., Dickensheets, D., Steele, A. *et al.* (2002) Astrobiological instrumentation for Mars–the only way is down. *International Journal of Astrobiology*, **1**, 365–380.

Ellery, A., Ball, A.J., Cockell, C., Dickensheets, D., Edwards, H., Kolb, C., Lammer, H., Patel, M. & Richter, L. (2005) Vanguard—a European robotic astrobiology-focussed Mars sub-surface mission proposal. *Acta Astronautica*, **56**, 397–407.

Evans, I.S. (2012) Geomorphometry and landform mapping: What is a landform? *Geomorphology*, **137**, 94–106.

Fairén, A.G., Dohm, J.M., Baker, V.R., de Pablo, M.A., Ruiz, J., Ferris, J.C. & Anderson, R.C. (2003) Episodic flood inundations of the northern plains of Mars. *Icarus*, **165**, 53–67.

Falaschi, D., Castro, M., Masiokas, M., Tadono, T. & Ahumada, A.L. (2014) Rock Glacier Inventory of the Valles Calchaquíes Region ($\sim 25°$ S), Salta, Argentina, Derived from ALOS Data. *Permafrost and Periglacial Processes*, **25**, 69–75.

Fassett, C.I., Dickson, J.L., Head, J.W., Levy, J.S. & Marchant, D.R. (2010) Supraglacial and proglacial valleys on Amazonian Mars. *Icarus*, **208**, 86–100.

Fastook, J.L., Head, J.W., Marchant, D.R. & Forget, F. (2008) Tropical mountain glaciers on Mars: Altitude-dependence of ice accumulation, accumulation conditions, formation times, glacier dynamics, and implications for planetary spin-axis/orbital history. *Icarus*, **198**, 305–317.

Feldman, W., Prettyman, T., Maurice, S., Plaut, J., Bish, D., Vaniman, D., Mellon, M., Metzger, A., Squyres, S., Karunatillake, S. *et al.* (2004) Global distribution of near-surface hydrogen on Mars. *Journal of Geophysical Research: Planets (1991–2012)*, **109**.

Fisher, P., Wood, J. & Cheng, T. (2004) Where is Helvellyn? Fuzziness of multi-scale landscape morphometry. *Transactions of the Institute of British Geographers*, **29**, 106–128.

Florinsky, I.V. (2012) *Digital terrain analysis in soil science and geology*. Academic Press.

Florinsky, I.V. (2014) Digital Terrain Modelling: Theory and Practice.
URL http://iflorinsky.narod.ru

Forget, F. (2009) The present and past climates of planet Mars. *EPJ Web of Conferences*, vol. 1, pp. 235–248. EDP Sciences.

Forget, F., Haberle, R., Montmessin, F., Levrard, B. & Head, J.W. (2006) Formation of glaciers on Mars by atmospheric precipitation at high obliquity. *Science*, **311**, 368–371.

Fouchet, T., Lellouch, E., Ignatiev, N., Forget, F., Titov, D., Tschimmel, M., Montmessin, F., Formisano, V., Giuranna, M., Maturilli, A. *et al.* (2007) Martian water vapor: Mars Express PFS/LW observations. *Icarus*, **190**, 32–49.

Fountain, A.G., Dana, G.L., Lewis, K.J., Vaughn, B.H. & Mcknight, D.H. (1998) *Glaciers of the McMurdo Dry Valleys, southern Victoria Land, Antarctica*. Wiley Online Library.

Fountain, A.G., Nylen, T.H., Monaghan, A., Basagic, H.J. & Bromwich, D. (2010) Snow in the McMurdo Dry Valleys, Antarctica. *International Journal of Climatology*, **30**, 633–642.

Frey, H.V. (2003) Large-Diameter Visible and Buried Impact Basins on Mars: Implications for Age of the Highlands and (Buried) Lowlands and Turn-Off of the Global Magnetic Field. *Lunar and Planetary Science Conference* (eds. S. Mackwell & E. Stansbery), vol. 34 of *Lunar and Planetary Science Conference*, p. 1838.

GDAL Development Team (2014) Geospatial Data Abstraction Library Homepage. URL `http://www.gdal.org`

Ghatan, G.J. & Zimbelman, J.R. (2006) Paucity of candidate coastal constructional landforms along proposed shorelines on Mars: Implications for a northern lowlands-filling ocean. *Icarus*, **185**, 171–196.

Ghosh, S., Stepinski, T.F. & Vilalta, R. (2010) Automatic annotation of planetary surfaces with geomorphic labels. *Geoscience and Remote Sensing, IEEE Transactions on*, **48**, 175–185.

Glass, B., Cannon, H., Branson, M., Hanagud, S. & Paulsen, G. (2008) DAME: planetary-prototype drilling automation. *Astrobiology*, **8**, 653–664.

Golombek, M., Anderson, R., Barnes, J.R., Bell, J., Bridges, N., Britt, D., Brückner, J., Cook, R., Crisp, D., Crisp, J. *et al.* (1999) Overview of the Mars Pathfinder mission: Launch through landing, surface operations, data sets, and science results. *Journal of Geophysical Research: Planets (1991–2012)*, **104**, 8523–8553.

Gwinner, K., Scholten, F., Spiegel, M., Schmidt, R., Giese, B., Oberst, J., Heipke, C., Jaumann, R. & Neukum, G. (2009) Derivation and validation of high-resolution digital terrain models from Mars Express HRSC data. *Photogrammetric Engineering & Remote Sensing*, **75**, 1127–1142.

Haberle, R.M., Murphy, J.R. & Schaeffer, J. (2003) Orbital change experiments with a Mars general circulation model. *Icarus*, **161**, 66–89.

Hartmann, W.K. (2005) Martian cratering 8: Isochron refinement and the chronology of Mars. *Icarus*, **174**, 294–320.

Hartmann, W.K., Ansan, V., Berman, D.C., Mangold, N. & Forget, F. (2014) Comprehensive analysis of glaciated martian crater Greg. *Icarus*, **228**, 96–120.

Hartmann, W.K., Thorsteinsson, T. & Sigurdsson, F. (2003) Martian hillside gullies and Icelandic analogs. *Icarus*, **162**, 259–277.

Hartmann, W.K. & Werner, S.C. (2010) Martian Cratering 10. Progress in use of crater counts to interpret geological processes: Examples from two debris aprons. *Earth and Planetary Science Letters*, **294**, 230–237.

Hauber, E., Reiss, D., Ulrich, M., Preusker, F., Trauthan, F., Zanetti, M., Hiesinger, H., Jaumann, R., Johansson, L., Johnsson, A. *et al.* (2011) Periglacial landscapes on Svalbard: Terrestrial analogs for cold-climate landforms on Mars. *Geological Society of America Special Papers*, **483**, 177–201.

Hauber, E., Slupetzky, H., Jaumann, R., Wewel, F., Gwinner, K. & Neukum, G. (2000) Digital and automated high resolution stereo mapping of the Sonnblick glacier (Austria) with HRSC-A. *Proceedings, EARSeL-SIG-Workshop Land Ice and Snow, Dresden, Germany*, pp. 246–254.

Hauber, E., Van Gasselt, S., Chapman, M. & Neukum, G. (2008) Geomorphic evidence for former lobate debris aprons at low latitudes on Mars: Indicators of the Martian paleoclimate. *Journal of Geophysical Research: Planets (1991–2012)*, **113**.

Hauber, E., van Gasselt, S., Ivanov, B., Werner, S., Head, J.W., Neukum, G., Jaumann, R., Greeley, R., Mitchell, K.L., Muller, P. *et al.* (2005) Discovery of a flank caldera and very young glacial activity at Hecates Tholus, Mars. *Nature*, **434**, 356–361.

Hays, J.D., Imbrie, J. & Shackleton, N.J. (1976) Variations in the Earth's orbit: Pacemaker of the ice ages. *Science*, **194**, 1121–1132.

Head, J.W., Ivanov, M.A., Hiesinger, H., Kreslavsky, M.A., Pratt, S. & Thomson, B.J. (2001) Oceans in the Northern Lowlands of Mars?: Further Tests Using MGS Data. *Lunar and Planetary Science Conference*, vol. 32 of *Lunar and Planetary Science Conference*, p. 1064.

Head, J.W., Neukum, G., Jaumann, R., Hiesinger, H., Hauber, E., Carr, M., Masson, P., Foing, B., Hoffmann, H., Kreslavsky, M. *et al.* (2005) Tropical to mid-latitude snow and ice accumulation, flow and glaciation on Mars. *Nature*, **434**, 346–351.

Head, J.W., Hiesinger, H., Ivanov, M.A., Kreslavsky, M.A., Pratt, S. & Thomson, B.J. (1999) Possible ancient oceans on Mars: evidence from Mars Orbiter Laser Altimeter data. *Science*, **286**, 2134–2137.

Head, J.W., Kreslavsky, M.A. & Pratt, S. (2002) Northern lowlands of Mars: Evidence for widespread volcanic flooding and tectonic deformation in the Hesperian Period. *Journal of Geophysical Research: Planets (1991–2012)*, **107**, 3–1.

Head, J.W., Marchant, D.R., Dickson, J.L., Kress, A.M. & Baker, D.M. (2010) Northern mid-latitude glaciation in the Late Amazonian period of Mars: Criteria for the recognition of debris-covered glacier and valley glacier landsystem deposits. *Earth and Planetary Science Letters*, **294**, 306–320.

Head, J.W., Marchant, D.R. & Kreslavsky, M.A. (2008) Formation of gullies on Mars: Link to recent climate history and insolation microenvironments implicate surface water flow origin. *Proceedings of the National academy of Sciences*, **105**, 13258–13263.

Head, J.W., Mustard, J.F., Kreslavsky, M.A., Milliken, R.E. & Marchant, D.R. (2003) Recent ice ages on Mars. *Nature*, **426**, 797–802.

Head, J.W. & Pratt, S. (2001) Extensive Hesperian-aged south polar ice sheet on Mars: Evidence for massive melting and retreat, and lateral flow and ponding of meltwater. *Journal of Geophysical Research: Planets (1991–2012)*, **106**, 12275–12299.

Heipke, C., Oberst, J., Albertz, J., Attwenger, M., Dorninger, P., Dorrer, E., Ewe, M., Gehrke, S., Gwinner, K., Hirschmüller, H. *et al.* (2007) Evaluating planetary digital terrain models—The HRSC DTM test. *Planetary and Space Science*, **55**, 2173–2191.

Herschel, W. (1784) On the remarkable appearances at the polar regions of the planet mars, the inclination of its axis, the position of its poles, and its spheroidical figure; with a few hints relating to its real diameter and atmosphere. *Philosophical Transactions of the Royal Society of London*, **74**, 233–273.

Hewitt, K. (2014) Rock Glaciers and Related Phenomena. *Glaciers of the Karakoram Himalaya*, pp. 267–289. Springer.

HiRISE Operations Centre, Lunar and Planetary Laboratory, University of Arizona (2014) High Resolution Imaging Science Experiment.
URL `http://hirise.lpl.arizona.edu`

Hobley, D.E., Howard, A.D. & Moore, J.M. (2014) Fresh shallow valleys in the Martian midlatitudes as features formed by meltwater flow beneath ice. *Journal of Geophysical Research: Planets*, **119**, 128–153.

Hoffman, N. (2000) White Mars: A New Model for Mars' Surface and Atmosphere Based on CO_2. *Icarus*, **146**, 326–342.

Holt, J.W., Safaeinili, A., Plaut, J.J., Head, J.W., Phillips, R.J., Seu, R., Kempf, S.D., Choudhary, P., Young, D.A., Putzig, N.E. *et al.* (2008) Radar sounding evidence for buried glaciers in the southern mid-latitudes of Mars. *Science*, **322**, 1235–1238.

Hubbard, A., Lawson, W., Anderson, B., Hubbard, B. & Blatter, H. (2004) Evidence for subglacial ponding across Taylor Glacier, Dry Valleys, Antarctica. *Annals of Glaciology*, **39**, 79–84.

Hubbard, B., Souness, C.J. & Brough, S. (2014) Glacier-like forms on Mars. *The Cryosphere Discuss.*

Hubbard, B., Milliken, R.E., Kargel, J.S., Limaye, A. & Souness, C.J. (2011) Geomorphological characterisation and interpretation of a mid-latitude glacier-like form: Hellas Planitia, Mars. *Icarus*, **211**, 330–346.

Humlum, O. (1988) Rock glacier appearance level and rock glacier initiation line altitude: a methodological approach to the study of rock glaciers. *Arctic and Alpine research*, pp. 160–178.

Iwahashi, J. & Pike, R.J. (2007) Automated classifications of topography from DEMs by an unsupervised nested-means algorithm and a three-part geometric signature. *Geomorphology*, **86**, 409–440.

Jakosky, B.M. & Phillips, R.J. (2001) Mars' volatile and climate history. *nature*, **412**, 237–244.

Jasiewicz, J. & Stepinski, T.F. (2014) University of Cincinnati, Space Informatics Lab Geomorphons App.
URL `http://sil.uc.edu/geom/app`

Jasiewicz, J. & Stepinski, T.F. (2013) Geomorphons—a pattern recognition approach to classification and mapping of landforms. *Geomorphology*, **182**, 147–156.

Jaumann, R., Neukum, G., Behnke, T., Duxbury, T., Eichentopf, K., Flohrer, J., Gasselt, S., Giese, B., Gwinner, K., Hauber, E. *et al.* (2007) The high-resolution stereo camera (HRSC) experiment on Mars Express: Instrument aspects and experiment conduct from interplanetary cruise through the nominal mission. *Planetary and Space Science*, **55**, 928–952.

Jaumann, R., Neukum, G., Tirsch, D., Hoffmann, H. & Mars Express HRSC Team (2014) The High Resolution Stereo Camera (HRSC): 10 Years of Imaging Mars. *LPI Contributions*, **1791**, 1078.

Johnsson, A., Reiss, D., Hauber, E., Hiesinger, H. & Zanetti, M. (2014) Evidence for very recent melt-water and debris flow activity in gullies in a young mid-latitude crater on Mars. *Icarus*, **235**, 37–54.

Kadish, S.J., Head, J.W., Barlow, N.G. & Marchant, D.R. (2008) Martian pedestal craters: Marginal sublimation pits implicate a climate-related formation mechanism. *Geophysical Research Letters*, **35**.

Kargel, J.S., Baker, V.R., Begét, J.E., Lockwood, J.F., Péwé, T.L., Shaw, J.S. & Strom, R.G. (1995) Evidence of ancient continental glaciation in the Martian northern plains. *Journal of Geophysical Research: Planets (1991–2012)*, **100**, 5351–5368.

Kargel, J.S. & Strom, R.G. (1992) Ancient glaciation on Mars. *Geology*, **20**, 3–7.

Keszthelyi, L., Jaeger, W., Dundas, C., Martínez-Alonso, S., McEwen, A. & Milazzo, M. (2010) Hydrovolcanic features on Mars: Preliminary observations from the first Mars year of HiRISE imaging. *Icarus*, **205**, 211–229.

Kim, J. & Muller, J.P. (2008) Very high resolution stereo DTM extraction and its application to surface roughness estimation over Martian surface. *International Archives of the Photogrammetry, Remote Sensing and Spatial Information Sciences*, **37**, 993–998.

Kim, J. & Muller, J.P. (2009) Multi-resolution topographic data extraction from Martian stereo imagery. *Planetary and Space Science*, **57**, 2095–2112.

Kite, E.S., Halevy, I., Kahre, M.A., Wolff, M.J. & Manga, M. (2013) Seasonal melting and the formation of sedimentary rocks on Mars, with predictions for the Gale Crater mound. *Icarus*, **223**, 181–210.

Kite, E.S., Lucas, A. & Fassett, C.I. (2013) Pacing early Mars river activity: Embedded craters in the Aeolis Dorsa region imply river activity spanned $\gtrsim$ (1–20) Myr. *Icarus*, **225**, 850–855.

Kite, E.S., Rafkin, S., Michaels, T.I., Dietrich, W.E. & Manga, M. (2011) Chaos terrain, storms, and past climate on Mars. *Journal of Geophysical Research: Planets (1991–2012)*, **116**.

Kite, E.S., Williams, J.P., Lucas, A. & Aharonson, O. (2014) Low palaeopressure of the martian atmosphere estimated from the size distribution of ancient craters. *Nature Geoscience*, **7**, 335–339.

Kolb, E.J. & Tanaka, K.L. (2001) Geologic history of the polar regions of Mars based on Mars Global Surveyor data: II. Amazonian Period. *Icarus*, **154**, 22–39.

Komatsu, G., Arzhannikov, S.G., Arzhannikova, A.V. & Ershov, K. (2007) Geomorphology of subglacial volcanoes in the Azas Plateau, the Tuva Republic, Russia. *Geomorphology*, **88**, 312–328.

Kowalewski, D., Marchant, D., Levy, J.S. & Head, J.W. (2006) Quantifying low rates of summertime sublimation for buried glacier ice in Beacon Valley, Antarctica. *Antarctic Science*, **18**, 421–428.

Kreslavsky, M.A. & Head, J.W. (2002a) Mars: Nature and evolution of young latitude-dependent water-ice-rich mantle. *Geophysical Research Letters*, **29**, 14–1.

Kreslavsky, M.A. & Head, J.W. (2000) Kilometer-scale roughness of Mars: Results from MOLA data analysis. *Journal of Geophysical Research: Planets (1991–2012)*, **105**, 26695–26711.

Kreslavsky, M.A. & Head, J.W. (2002b) Fate of outflow channel effluents in the northern lowlands of Mars: The Vastitas Borealis Formation as a sublimation residue from frozen ponded bodies of water. *Journal of Geophysical Research: Planets (1991–2012)*, **107**, 4–1.

Kreslavsky, M.A. & Head, J.W. (2011) Carbon dioxide glaciers on Mars: Products of recent low obliquity epochs (?). *Icarus*, **216**, 111–115.

Kreslavsky, M.A., Head, J.W. & Marchant, D.R. (2008) Periods of active permafrost layer formation during the geological history of Mars: Implications for circum-polar and mid-latitude surface processes. *Planetary and Space Science*, **56**, 289–302.

Kress, A.M. & Head, J.W. (2008) Ring-mold craters in lineated valley fill and lobate debris aprons on Mars: Evidence for subsurface glacial ice. *Geophysical Research Letters*, **35**.

Lammer, H., Chassefière, E., Karatekin, Í., Morschhauser, A., Niles, P.B., Mousis, O., Odert, P., Ute, V., Breuer, D., Dehant, V. *et al.* (2013) Outgassing history and escape of the Martian atmosphere and water inventory. *Space Science Reviews*, **174**, 113–154.

Laskar, J., Gastineau, M., Joutel, F., Levrard, B., Robutel, P. & Correia, A. (2004) A new astronomical solution for the long term evolution of the insolation quantities of Mars. *Lunar and Planetary Institute Science Conference Abstracts*, vol. 35, p. 1600.

Laskar, J., Joutel, F. & Boudin, F. (1993) Orbital, precessional, and insolation quantities for the Earth from-20 Myr to+ 10 Myr. *Astronomy and Astrophysics*, **270**, 522–533.

Lemmon, M., Smith, P., Shinohara, C., Tanner, R., Woida, P., Shaw, A., Hughes, J., Reynolds, R., Woida, R., Penegor, J. *et al.* (2008) The Phoenix surface stereo imager (SSI) investigation. *Lunar and Planetary Institute Science Conference Abstracts*, vol. 39, p. 2156.

Levy, J.S., Head, J.W., Marchant, D., Dickson, J. & Morgan, G. (2009) Geologically recent gully–polygon relationships on Mars: Insights from the Antarctic Dry Valleys on the roles of permafrost, microclimates, and water sources for surface flow. *Icarus*, **201**, 113–126.

Levy, J.S., Head, J.W. & Marchant, D.R. (2007) Lineated valley fill and lobate debris apron stratigraphy in Nilosyrtis Mensae, Mars: Evidence for phases of

glacial modification of the dichotomy boundary. *Journal of Geophysical Research: Planets (1991–2012)*, **112**.

Levy, J.S., Head, J.W. & Marchant, D.R. (2009) Concentric crater fill in Utopia Planitia: History and interaction between glacial "brain terrain" and periglacial mantle processes. *Icarus*, **202**, 462–476.

Levy, J.S., Marchant, D.R. & Head, J.W. (2010) Thermal contraction crack polygons on Mars: A synthesis from HiRISE, Phoenix, and terrestrial analog studies. *Icarus*, **206**, 229–252.

Lissauer, J.J., Barnes, J.W. & Chambers, J.E. (2012) Obliquity variations of a moonless Earth. *Icarus*, **217**, 77–87.

Lobitz, B., Wood, B.L., Averner, M.M. & McKay, C.P. (2001) Use of spacecraft data to derive regions on Mars where liquid water would be stable. *Proceedings of the National Academy of Sciences*, **98**, 2132–2137.

Lucchitta, B.K. (1984) Ice and debris in the fretted terrain, Mars. *Journal of Geophysical Research: Solid Earth (1978–2012)*, **89**, B409–B418.

MacMillan, R., Pettapiece, W., Nolan, S. & Goddard, T. (2000) A generic procedure for automatically segmenting landforms into landform elements using DEMs, heuristic rules and fuzzy logic. *Fuzzy sets and Systems*, **113**, 81–109.

Madeleine, J.B., Forget, F., Head, J.W., Levrard, B., Montmessin, F. & Millour, E. (2009) Amazonian northern mid-latitude glaciation on Mars: A proposed climate scenario. *Icarus*, **203**, 390–405.

Mahaney, W.C., Miyamoto, H., Dohm, J.M., Baker, V.R., Cabrol, N.A., Grin, E.A. & Berman, D.C. (2007) Rock glaciers on Mars: Earth-based clues to Mars' recent paleoclimatic history. *Planetary and Space Science*, **55**, 181–192.

Malin, M.C., Bell, J.F., Cantor, B.A., Caplinger, M.A., Calvin, W.M., Clancy, R.T., Edgett, K.S., Edwards, L., Haberle, R.M., James, P.B. *et al.* (2007) Context camera investigation on board the Mars Reconnaissance Orbiter. *Journal of Geophysical Research: Planets (1991–2012)*, **112**.

Malin, M.C., Lavoie, S. & Grayzeck, E. (2007) Mars Reconnaissance Orbiter (MRO) CTX and MARCI EDR Archive Volume Software Interface Specification (SIS). , Jet Propulsion Laboratory, NASA.

Mangold, N. (2005) High latitude patterned grounds on Mars: Classification, distribution and climatic control. *Icarus*, **174**, 336–359.

Marchant, D.R. & Head, J.W. (2003) Tongue-shaped lobes on Mars: Morphology, nomenclature, and relation to rock glacier deposits. *Sixth International Conference on Mars*, vol. 1, p. 3091.

Marchant, D.R., Lewis, A., Phillips, W., Moore, E., Souchez, R., Denton, G., Sugden, D., Potter, N. & Landis, G. (2002) Formation of patterned ground and sublimation till over Miocene glacier ice in Beacon Valley, southern Victoria Land, Antarctica. *Geological Society of America Bulletin*, **114**, 718–730.

Marchant, D.R. & Head, J.W. (2007) Antarctic dry valleys: Microclimate zonation, variable geomorphic processes, and implications for assessing climate change on Mars. *Icarus*, **192**, 187–222.

Martínez, G. & Renno, N. (2013) Water and brines on Mars: current evidence and implications for MSL. *Space Science Reviews*, **175**, 29–51.

Martínez-Alonso, S., Mellon, M., Banks, M., Keszthelyi, L. & McEwen, A. (2011) Evidence of volcanic and glacial activity in Chryse and Acidalia Planitiae, Mars. *Icarus*, **212**, 597–621.

Mayo, L.R. (1984) Glacier mass balance and runoff research in the USA. *Geografiska Annaler. Series A. Physical Geography*, pp. 215–227.

McEwen, A.S., Dundas, C.M., Mattson, S.S., Toigo, A.D., Ojha, L., Wray, J.J., Chojnacki, M., Byrne, S., Murchie, S.L. & Thomas, N. (2013) Recurring slope lineae in equatorial regions of Mars. *Nature Geoscience*, **7**, 53–58.

McEwen, A.S., Eliason, E.M., Bergstrom, J.W., Bridges, N.T., Hansen, C.J., Delamere, W.A., Grant, J.A., Gulick, V.C., Herkenhoff, K.E., Keszthelyi, L. *et al.* (2007) Mars reconnaissance orbiter's high resolution imaging science experiment (HiRISE). *Journal of Geophysical Research: Planets (1991–2012)*, **112**.

Mellon, M.T., Arvidson, R.E., Sizemore, H.G., Searls, M.L., Blaney, D.L., Cull, S., Hecht, M.H., Heet, T.L., Keller, H.U., Lemmon, M.T. *et al.* (2009) Ground ice at the Phoenix landing site: Stability state and origin. *Journal of Geophysical Research: Planets (1991–2012)*, **114**.

Mellon, M.T. & Jakosky, B.M. (1995) The distribution and behavior of Martian ground ice during past and present epochs. *Journal of Geophysical Research: Planets (1991–2012)*, **100**, 11781–11799.

Melosh, H.J. (2011) *Planetary surface processes*. Cambridge University Press.

Michael, G. & Neukum, G. (2010) Planetary surface dating from crater size–frequency distribution measurements: Partial resurfacing events and statistical age uncertainty. *Earth and Planetary Science Letters*, **294**, 223–229.

Milkovich, S.M., Head, J.W. & Marchant, D.R. (2006) Debris-covered piedmont glaciers along the northwest flank of the Olympus Mons scarp: Evidence for low-latitude ice accumulation during the Late Amazonian of Mars. *Icarus*, **181**, 388–407.

Milliken, R., Mustard, J. & Goldsby, D. (2003) Viscous flow features on the surface of Mars: Observations from high-resolution Mars Orbiter Camera (MOC) images. *Journal of Geophysical Research: Planets (1991–2012)*, **108**.

Minár, J. & Evans, I.S. (2008) Elementary forms for land surface segmentation: The theoretical basis of terrain analysis and geomorphological mapping. *Geomorphology*, **95**, 236–259.

Mishkin, A.H., Limonadi, D., Laubach, S.L. & Bass, D.S. (2006) Working the Martian night shift-the MER surface operations process. *Robotics & Automation Magazine, IEEE*, **13**, 46–53.

Montmessin, F. (2007) The orbital forcing of climate changes on Mars. *Solar Variability and Planetary Climates*, pp. 457–472. Springer.

Moore, J.M. & Wilhelms, D.E. (2001) Hellas as a possible site of ancient ice-covered lakes on Mars. *Icarus*, **154**, 258–276.

Morgan, G.A., Head, J.W. & Marchant, D.R. (2009) Lineated valley fill (LVF) and lobate debris aprons (LDA) in the Deuteronilus Mensae northern dichotomy boundary region, Mars: Constraints on the extent, age and episodicity of Amazonian glacial events. *Icarus*, **202**, 22–38.

Morgan, G.A., Head, J.W. & Marchant, D.R. (2011) Preservation of Late Amazonian Mars ice and water-related deposits in a unique crater environment in Noachis Terra: Age relationships between lobate debris tongues and gullies. *Icarus*, **211**, 347–365.

Mustard, J.F., Cooper, C.D. & Rifkin, M.K. (2001) Evidence for recent climate change on Mars from the identification of youthful near-surface ground ice. *Nature*, **412**, 411–414.

Nakawo, M., Yabuki, H. & Sakai, A. (1999) Characteristics of Khumbu Glacier, Nepal Himalaya: recent change in the debris-covered area. *Annals of Glaciology*, **28**, 118–122.

Neukum, G. & Jaumann, R. (2004) HRSC: The high resolution stereo camera of Mars Express. *Mars Express: The Scientific Payload*, vol. 1240, pp. 17–35.

Neukum, G., Jaumann, R., Hoffmann, H., Hauber, E., Head, J.W., Basilevsky, A., Ivanov, B., Werner, S., Van Gasselt, S., Murray, J. *et al.* (2004) Recent and episodic volcanic and glacial activity on Mars revealed by the High Resolution Stereo Camera. *Nature*, **432**, 971–979.

Newman, C.E., Lewis, S.R. & Read, P.L. (2005) The atmospheric circulation and dust activity in different orbital epochs on Mars. *Icarus*, **174**, 135–160.

NSSDC (2014) National Space Science Data Centre Mars Fact Sheet. URL http://nssdc.gsfc.nasa.gov/planetary/factsheet/marsfact.html

Ødegård, R.S., Isaksen, K., Eiken, T. & Ludvig Sollid, J. (2003) Terrain analyses and surface velocity measurements of the Hiorthfjellet rock glacier, Svalbard. *Permafrost and Periglacial Processes*, **14**, 359–365.

Otto, J.C., Kleinod, K., König, O., Krautblatter, M., Nyenhuis, M., Roer, I., Schneider, M., Schreiner, B. & Dikau, R. (2007) HRSC-A data: a new high-resolution data set with multipurpose applications in physical geography. *Progress in Physical Geography*, **31**, 179–197.

Parsons, R.A., Nimmo, F. & Miyamoto, H. (2011) Constraints on martian lobate debris apron evolution and rheology from numerical modeling of ice flow. *Icarus*, **214**, 246–257.

Pathare, A.V., Paige, D.A. & Turtle, E. (2005) Viscous relaxation of craters within the Martian south polar layered deposits. *Icarus*, **174**, 396–418.

Pedersen, G. (2013) Frozen Martian lahars? Evaluation of morphology, degradation and geologic development in the Utopia–Elysium transition zone. *Planetary and Space Science*, **85**, 59–77.

Perminov, V. (1999) The difficult road to Mars. *National Aeronautics and Space Administration Monographs in Aerospace History*.

Perucca, L. & Angillieri, M.Y.E. (2011) Glaciers and rock glaciers' distribution at 28° S, Dry Andes of Argentina, and some considerations about their hydrological significance. *Environmental Earth Sciences*, **64**, 2079–2089.

Pierce, T.L. & Crown, D.A. (2003) Morphologic and topographic analyses of debris aprons in the eastern Hellas region, Mars. *Icarus*, **163**, 46–65.

Planetary Data System Geosciences Node (2014) Mars Orbital Data Explorer. URL http://ode.rsl.wustl.edu/mars

Plaut, J.J., Safaeinili, A., Holt, J.W., Phillips, R.J., Head, J.W., Seu, R., Putzig, N.E. & Frigeri, A. (2009) Radar evidence for ice in lobate debris aprons in the mid-northern latitudes of Mars. *Geophysical Research Letters*, **36**.

Plesko, C.S. (2010) *Automated feature detection and hydrocode modeling of impact-related structures on Mars*. Ph.D. thesis, University of California, Santa Cruz.

Prima, O.D.A., Echigo, A., Yokoyama, R. & Yoshida, T. (2006) Supervised landform classification of Northeast Honshu from DEM-derived thematic maps. *Geomorphology*, **78**, 373–386.

Ramirez, R.M., Kopparapu, R., Zugger, M.E., Robinson, T.D., Freedman, R. & Kasting, J.F. (2014) Warming early Mars with CO_2 and H_2. *Nature Geoscience*, **7**, 59–63.

Rech, J.A., Currie, B.S., Shullenberger, E.D., Dunagan, S.P., Jordan, T.E., Blanco, N., Tomlinson, A.J., Rowe, H.D. & Houston, J. (2010) Evidence for the development of the Andean rain shadow from a Neogene isotopic record in the Atacama Desert, Chile. *Earth and Planetary Science Letters*, **292**, 371–382.

Rennó, N.O., Bos, B.J., Catling, D., Clark, B.C., Drube, L., Fisher, D., Goetz, W., Hviid, S.F., Keller, H.U., Kok, J.F. *et al.* (2009) Possible physical and thermodynamical evidence for liquid water at the Phoenix landing site. *Journal of Geophysical Research: Planets (1991–2012)*, **114**.

Reuter, H., Wendroth, O. & Kersebaum, K. (2006) Optimisation of relief classification for different levels of generalisation. *Geomorphology*, **77**, 79–89.

Rignot, E., Hallet, B. & Fountain, A. (2002) Rock glacier surface motion in Beacon Valley, Antarctica, from synthetic-aperture radar interferometry. *Geophysical Research Letters*, **29**, 48–1.

Romstad, B. & Etzelmüller, B. (2009) Structuring the digital elevation model into landform elements through watershed segmentation of curvature. *Proceedings of Geomorphometry*, **2009**, 55–60.

Schmidt, J. & Hewitt, A. (2004) Fuzzy land element classification from DTMs based on geometry and terrain position. *Geoderma*, **121**, 243–256.

Scholten, F., Gwinner, K., Roatsch, T., Matz, K., Wahlisch, M., Giese, B., Oberst, J., Jaumann, R. & Neukum, G. (2005) Mars express HRSC data processing-methods and operational aspects. *Photogrammetric engineering and remote sensing*, **71**, 1143.

Scholten, F. & Wewel, F. (2000) Digital 3D-data acquisition with the high resolution stereo camera-airborne (HRSC-A). *International Archives of Photogrammetry and Remote Sensing*, **33**, 901–908.

Schon, S.C. & Head, J.W. (2012) Decameter-scale pedestal craters in the tropics of Mars: Evidence for the recent presence of very young regional ice deposits in Tharsis. *Earth and Planetary Science Letters*, **317**, 68–75.

Schon, S.C., Head, J.W. & Milliken, R.E. (2009) A recent ice age on Mars: Evidence for climate oscillations from regional layering in mid-latitude mantling deposits. *Geophysical Research Letters*, **36**.

Searls, M., Mellon, M., Martinez-Alonso, S. & Team, H. (2008) Slope Analysis and Ice Stability of the Mid-Latitude Dissected Terrain on Mars. *Lunar and Planetary Institute Science Conference Abstracts*, vol. 39, p. 2376.

Sharp, R.P. (1973) Mars: Fretted and chaotic terrains. *Journal of geophysical research*, **78**, 4073–4083.

Shean, D.E., Head, J.W., Fastook, J.L. & Marchant, D.R. (2007) Recent glaciation at high elevations on Arsia Mons, Mars: Implications for the formation and evolution of large tropical mountain glaciers. *Journal of Geophysical Research: Planets (1991–2012)*, **112**.

Shean, D.E., Head, J.W. & Marchant, D.R. (2005) Origin and evolution of a cold-based tropical mountain glacier on Mars: The Pavonis Mons fan-shaped deposit. *Journal of Geophysical Research: Planets (1991–2012)*, **110**.

Shepherd, J., Bunting, P. & Dymond, J. (2014) Operational large-scale segmentation of imagery based on iterative elimination. *Journal of Applied Remote Sensing. (Submitted)*.
URL http://www.rsgislib.org/rsgislib_segmentation.html

Smith, D.E., Zuber, M., Frey, H., Garvin, J., Head, J.W., Muhleman, D., Pettengill, G., Phillips, R., Solomon, S., Zwally, H. *et al.* (1998) Topography of the northern hemisphere of Mars from the Mars Orbiter Laser Altimeter. *Science*, **279**, 1686–1692.

Smith, D.E., Zuber, M.T., Solomon, S.C., Phillips, R.J., Head, J.W., Garvin, J.B., Banerdt, W.B., Muhleman, D.O., Pettengill, G.H., Neumann, G.A. *et al.* (1999) The global topography of Mars and implications for surface evolution. *Science*, **284**, 1495–1503.

Soare, R.J., Conway, S., Dohm, J. & El-Maarry, M. (2014) Possible open-system (hydraulic) pingos in and around the Argyre impact region of Mars. *Earth and Planetary Science Letters*, **398**, 25–36.

Soare, R.J., Burr, D.M. & Wan Bun Tseung, J.M. (2005) Possible pingos and a periglacial landscape in northwest Utopia Planitia. *Icarus*, **174**, 373–382.

Soare, R.J. & Osinski, G.R. (2009) Stratigraphical evidence of late Amazonian periglaciation and glaciation in the Astapus Colles region of Mars. *Icarus*, **202**, 17–21.

Soare, R.J., Osinski, G.R. & Roehm, C.L. (2008) Thermokarst lakes and ponds on Mars in the very recent (late Amazonian) past. *Earth and Planetary Science Letters*, **272**, 382–393.

Som, S.M., Greenberg, H.M. & Montgomery, D.R. (2008) The Mars Orbiter Laser Altimeter dataset: Limitations and improvements. *Mars*, **4**, 14–26.

Souness, C.J. & Hubbard, B. (2012) Mid-latitude glaciation on Mars. *Progress in Physical Geography*, **36**, 238–261.

Souness, C.J. & Hubbard, B. (2013) An alternative interpretation of late Amazonian ice flow: Protonilus Mensae, Mars. *Icarus*.

Souness, C.J., Hubbard, B., Milliken, R.E. & Quincey, D. (2012) An inventory and population-scale analysis of martian glacier-like forms. *Icarus*, **217**, 243–255.

Squyres, S.W. (1978) Martian fretted terrain: Flow of erosional debris. *Icarus*, **34**, 600–613.

Squyres, S.W. (1979) The distribution of lobate debris aprons and similar flows on Mars. *Journal of Geophysical Research: Solid Earth (1978–2012)*, **84**, 8087–8096.

Stepinski, T.F. & Collier, M. (2004) Extraction of Martian valley networks from digital topography. *Journal of Geophysical Research: Planets (1991–2012)*, **109**.

Stepinski, T.F. & Bagaria, C. (2009) Segmentation-based unsupervised terrain classification for generation of physiographic maps. *Geoscience and Remote Sensing Letters, IEEE*, **6**, 733–737.

Stepinski, T.F., Ghosh, S. & Vilalta, R. (2006) Automatic recognition of landforms on Mars using terrain segmentation and classification. *Discovery Science*, pp. 255–266. Springer.

Stepinski, T.F., Mendenhall, M.P. & Bue, B.D. (2009) Machine cataloging of impact craters on Mars. *Icarus*, **203**, 77–87.

Stepinski, T.F. & Vilalta, R. (2005) Digital topography models for Martian surfaces. *Geoscience and Remote Sensing Letters, IEEE*, **2**, 260–264.

Sugden, D.E., Marchant, D.R., Potter Jr, N., Souchez, R.A., Denton, G.H., Swisher III, C.C. & Tison, J.L. (1995) Preservation of Miocene glacier ice in East Antarctica. *Nature*, **376**, 412–414.

Tanaka, K.L. & Kolb, E.J. (2001) Geologic history of the polar regions of Mars based on Mars Global Surveyor Data: I. Noachian and Hesperian Periods. *Icarus*, **154**, 3–21.

Trainer, M.G., Tolbert, M.A., McKay, C.P. & Toon, O.B. (2010) Enhanced CO_2 trapping in water ice via atmospheric deposition with relevance to Mars. *Icarus*, **206**, 707–715.

Turtle, E., Pathare, A., Hartmann, W. & Esquerdo, G. (2001) Investigating Creep of Ground Ice as a Cause of Crater Relaxation in Martian High-Latitude Softened Terrain. *Lunar and Planetary Institute Science Conference Abstracts*, vol. 32, p. 2044.

Van Asselen, S. & Seijmonsbergen, A. (2006) Expert-driven semi-automated geomorphological mapping for a mountainous area using a laser DTM. *Geomorphology*, **78**, 309–320.

Van Gasselt, S., Hauber, E. & Neukum, G. (2010) Lineated valley fill at the Martian dichotomy boundary: Nature and history of degradation. *Journal of Geophysical Research: Planets (1991–2012)*, **115**.

Wagnon, P., Ribstein, P., Kaser, G. & Berton, P. (1999) Energy balance and runoff seasonality of a Bolivian glacier. *Global and planetary change*, **22**, 49–58.

Werner, S.C. (2009) The global martian volcanic evolutionary history. *Icarus*, **201**, 44–68.

Whalley, W.B. & Azizi, F. (2003) Rock glaciers and protalus landforms: Analogous forms and ice sources on Earth and Mars. *Journal of Geophysical Research: Planets (1991–2012)*, **108**.

Williams, D.M. & Pollard, D. (2003) Extraordinary climates of Earth-like planets: three-dimensional climate simulations at extreme obliquity. *International Journal of Astrobiology*, **2**, 1–19.

Wood, J. (1999) Visualization of scale dependencies in the surface models. *International Cartographic Association Annual Conference, Ottawa*.

Wood, J. (2009) LandSerf webpage.
URL `http://www.landserf.org`

Wood, J. (1996) *The geomorphological characterisation of digital elevation models*. Ph.D. thesis, University of Leicester.
URL `http://www.soi.city.ac.uk/~jwo/phd/`

Wood, J. (1998) Modelling the continuity of surface form using digital elevation models. *Proceedings of the 8th international symposium on spatial data handling*, pp. 725–736. IGU Commission of GIS New York.

Yokohata, T., Odaka, M. & Kuramoto, K. (2002) Role of H_2O and CO_2 Ices in Martian Climate Changes. *Icarus*, **159**, 439–448.

Yokoyama, R., Shirasawa, M. & Pike, R.J. (2002) Visualizing topography by openness: a new application of image processing to digital elevation models. *Photogrammetric engineering and remote sensing*, **68**, 257–266.

Zalewska, N. (2013) Hellas Planitia as a potential site of sedimentary minerals. *Planetary and Space Science*, **78**, 25–32.

Zalewska, N. (2014) Water in the Deepest Crater of Mars. *Insights on Environmental Changes*, pp. 65–76. Springer.

Zealey, W.J. (2009) Glacial, periglacial and glacio-volcanic structures on the Echus Plateau, upper Kasei Valles. *Planetary and Space Science*, **57**, 699–710.

Zuber, M., Smith, D., Solomon, S., Muhleman, D., Head, J.W., Garvin, J., Abshire, J. & Bufton, J. (1992) The Mars Observer laser altimeter investigation. *Journal of Geophysical Research: Planets (1991–2012)*, **97**, 7781–7797.